IMPROVED ATMOSPHERIC DENSITY ESTIMATION FOR ANDE-2 SATELLITES USING DRAG COEFFICIENTS OBTAINED FROM GAS-SURFACE INTERACTION EQUATIONS

BY

Harold Patrick Flanagan

Submitted to the graduate degree program in Aerospace Engineering and the Graduate Faculty of the University of Kansas in partial fulfillment of the requirements for the degree of Master of Science

Committee members:

Chairperson: Dr. Craig McLaughlin

Dr. Haiyang Chao

Dr. Zhongquan Charlie Zheng

Date:

The Thesis Committee for Harold Flanagan certifies that this is the approved version of the following thesis:

IMPROVED ATMOSPHERIC DENSITY ESTIMATION FOR ANDE-2 SATELLITES USING DRAG COEFFICIENTS OBTAINED FROM GAS-SURFACE INTERACTION EQUATIONS

BY

Harold Patrick Flanagan

Committee members:

Chairperson: Dr. Craig McLaughlin

Dr. Haiyang Chao

Dr. Zhongquan Charlie Zheng

Date:

ABSTRACT

A major issue in the process of predicting the future position of satellites in low earth orbit (LEO) is that the drag coefficient of a satellite is generally not precisely known throughout the satellite's lifespan. One reason for this problem is that as a satellite travels through the Earth's thermosphere, variations in the composition of the thermosphere directly affect the drag coefficient of the satellite. The greatest amount of uncertainty in the drag coefficient from these variations in the thermosphere comes from the amount of atomic oxygen that covers the satellites surface as the satellite descends to lower altitudes. This percent surface coverage of atomic oxygen directly affects the interaction between the surface of the satellite and the gas through which it is passing.

The work performed in this thesis determines the drag coefficients of the ANDE-2 satellites over their life spans by using satellite laser ranging (SLR) data of the ANDE-2 satellites in unison with gas-surface interaction equations. The fractional coverage of atomic oxygen is determined by using empirically determined data and semi-empirical models that attempt to predict the fractional coverage of oxygen relative to the composition of the atmosphere. These drag coefficients are then used to determine the atmospheric densities experienced by these satellites over various days, so that inaccuracies in the atmospheric models can be observed. The drag coefficients of the ANDE-2 satellites decrease throughout the satellites' life, and vary most due to changes in the temperature and density of the atmosphere. The greatest uncertainty in the atmosphere's composition occurs at lower altitudes at the end of ANDE-2's life.

ACKNOWLEDGEMENTS

I would first like to thank Dr. Craig A. McLaughlin for the opportunity to perform this research and for the time, advice, and patience he has bestowed upon me during this process. I would also like to thank Dr. Haiyang Chao and Dr. Zhongquan Charlie Zheng for being my committee members.

The previous research performed by Travis Lechtenberg, Piyush Mehta, Andrew Hiatt, Dhaval Krishna involving precision orbit ephemeris, ballistic and density coefficients half-lives, accommodation coefficients, satellite drag coefficients, and their personal codes have all made this thesis possible. Much of the data conversion and ODTK scripts that were used in this research came from the previous help and assistance of Dr. David A. Vallado and Jens Ramrath at Analytical Graphics, Inc. The research involving accommodation coefficients performed by Kenneth and Mildred Moe, Marcin Pilinski, Andrew Walker, Piyush Mehta, Bruce Bowman, Brian Argrow, Scott Palo, and Joseph Koller has truly been invaluable to the creation of this thesis.

I would also like to personally thank the people that took the time to write the letters of recommendation that made it possible for me to attend the University of Kansas and achieve a master's degree. My sincerest thanks go to Dr. Lukie L. Christie, Dr. Luis A. Rodriguez, and Dr. Luis G. Rodriguez. A special thanks to Dr. Daniel Raymer for encouraging me throughout my high school and college years and for his advice involving the pursuit of a career in aerospace engineering.

I am completely and wholly indebted to my parents for their love and support throughout my education. Without their time, commitment, and support, I could not have risen to the task of completing this thesis. They are the foundation that all of my accomplishments are built upon.

TABLE OF CONTENTS

Nomenclature

Symbol	Definition	Units
$\vec{a}_{drag}$	Acceleration due to drag	m/s^2
A	Area if satellite	m^2
a	Semi-major axis	m
a_b	Earth albedo	
AMU_{mass}	AMU conversion to kg	kg/AMU
a_p	3-hour geomagnetic amplitude index	Tesla or kg s/m
Ap	Daily geomagnetic amplitude index	Tesla or kg s/m
A_r	Molecular mass of argon	AMU
BC	Ballistic coefficient	$m^{2/kg}$
$\Delta BC/BC$	Estimated ballistic coefficient correction	
$C_{\oplus}$	Variable related to Earth's eccentricity	m/degrees
C_D	Satellite drag coefficient	
$C_{D,ads}$	Adsorption drag coefficient	
$C_{D,cy}$	Drag coefficient of a cylinder	

$C_{D,fp}$	Drag coefficient of a flat plate	
$C_{D,S}$	Drag coefficient for clean satellite surface	
$C_{D,sp}$	Drag coefficient of a sphere	
$C_{D,T}$	Total drag coefficient	
C_v	Streaming heat capacity	J/mol K
D	Diameter of spacecraft	m
d	Cross correlation delay	minutes
d_{avg}	Mean collision diameter	m
e	Eccentricity	
$e_{\oplus}$	Earth's eccentricity	
e_{IR}	Emissivity	W/m^2
erf	Gauss error function	
E	Energy	Joules
E_i	Incident energy	Joules
E_r	Reflected energy	Joules
E_W	Wall/surface energy	Joules
$F_{10.7}$	Daily solar flux measured at 10.7 cm wavelength	SFU
$F_{10.7}(adj)$	Adjusted daily solar flux	SFU
$F_{10.7}(obs)$	Observed daily solar flux	SFU

$F_{s\text{-}e}$	View factor from a sphere to Earth	
g_0	Gravitational acceleration	m/s^2
G_s	Solar constant	W/m^2
H	Satellite's attitude	km
H	Molecular mass of hydrogen	AMU
H_e	Molecular mass of helium	AMU
Δh	Change in altitude	m
i	Cross correlation series index	
I_0	Modified Bessel function	
i_{inc}	Inclination	deg
k	Sequence index for Gauss Markov process and sequential filter	
K	Geomagnetic activity level	
K	Langmuir isotherm fitting parameter	

K_a	Reflection of collimated incoming solar energy off of a spherical Earth factor	
k_b	Boltzmann constant	m^2kg/s^2K
K_k	Kalman gain at *k*	
K_n	Knudsen number	
K_p	Geomagnetic planetary index	
K_p	Planetary geomagnetic activity level	
L_{ref}	Length of spacecraft	m
m	Number of days being analyzed	
m	Satellite mass	kg
M	Mean molecular mass	AMU
$M_{10.7}$	Solar index for far ultraviolet radiation	SFU
m_{atm}	Molecular mass of atmosphere	AMU
m_g	Mean molecular mass	kg
m_s	Atomic mass of satellite surface	AMU
mx	Mean of series x	
my	Mean of series y	
N	Molecular mass of nitrogen	AMU

N	Number of elements	
n_0	Oxygen number density	Number molecules/m^3
N_2	Molecular mass of nitrogen	AMU
O	Molecular mass of atomic oxygen	AMU
O_2	Molecular mass of oxygen	AMU
p	Atmospheric pressure	Pa
P	Partial pressure component	Number of molecules * K
p_0	Absolute pressure	Pa
P_o	Partial pressure component of atomic oxygen	Pa
$P(u_i \longrightarrow u_r).$	Scattering kernel for u	
$P(v_i \longrightarrow v_r)$	Scattering kernel for v	
Δp	Change in pressure	N/m^2
q_{IR}	Earth IR emission	W/m^2
Q_W	Electrical power dissipation	W
R	Universal gas constant	J/mol K
$R_\oplus$	Earth's equatorial radius	m
R_E	Earth's equatorial radius	km
$\vec{r}$	Position vector	m

$r_{ECEFsat}$	Position vector in ECEF	m
r_i	x coordinate position	m
r_j	y coordinate position	m
r_k	z coordinate position	m
$r_{\delta sat}$	Position vector for *i* and *j* coordinates	m
s	Speed ratio	
t	time	UT seconds
T	Kinetic temperature of gas	K
T_a	True anomaly	degrees
t_0	Initial time	seconds
T_∞	Atmospheric temperature of gas	K
T_i	Atmospheric temperature	K
$T_{k,i}$	Temperature of incoming molecule	K
$T_{k,r}$	Temperature of reflected molecule	K
T_{MAX}	Maximum expected satellite surface temperature	K
T_{MIN}	Minimum expected satellite surface temperature	K

tp	Time of periapsis	UT seconds
T_W	Satellite surface temperature	K
u	Normal velocity component	
u_i	Incident normal velocity component	
u_r	Reflected normal velocity component	
w	Tangential velocity component	
$w(t_k)$	Gaussian white noise variable	
x	x coordinate position	m
x_0	Initial estimate	
$\boldsymbol{X}_0^*$	Initial conditions	
X_f	Filter state	
x_i	Cross-correlation series	
X_s	Smoother state	
ΔX	State error matrix	
$\Delta\hat{X}$	Optimal state error estimate	
y	y coordinate position	m
y_i	Cross-correlation series	
Δy	Measurement residual	

z	z position	m
∞	Infinity	

Greek Symbol	**Definition**	**Units**
α	Accommodation coefficient	
α_l	Longitude angle	degrees
α_m	Gauss Markov variable	
α_n	Normal energy accommodation coefficient	
α_s	Goodman accommodation coefficient	
α_t	Tangential energy accommodation coefficient	
δ	Initial latitude angle	degrees
θ	Fraction of satellite's surface covered by atomic oxygen	
λ	Mean distance between molecular collisions	m
μ	Ratio of atomic mass of atmosphere to atomic mass of satellite surface	

σ_t	Tangential momentum accommodation coefficient	
τ	User defined half-life	seconds
υ	Tangential velocity component	m/s
υ_i	Incident tangential velocity component	m/s
υ_{mp}	Most probable speed	m/s
υ_r	Reflected tangential velocity component	m/s
υ_{rel}	relative velocity	m/s
υ_w	Tangential velocity component	m/s
$\vec{\upsilon}_{rel}$	Relative velocity vector	m/s
Φ	State transition matrix	
ϕ_{gd}	Incremental geodetic latitude angle	degrees
Φ_{gdold}	Previous incremental geodetic latitude angle	degrees
Ω	Earth's rotational velocity	Radians/solar second
Ω	Right ascension of the ascending node	degrees
ω_p	Argument of periapsis	degrees

ρ	Density	kg/m^3
ρ_{Ar}	Argon number density	$1/m^3$
ρ_{H}	Hydrogen number density	$1/m^3$
ρ_{He}	Helium number density	$1/m^3$
ρ_{N}	Atomic nitrogen density	$1/m^3$
ρ_{N2}	Nitrogen number density	$1/m^3$
ρ_{O}	Atomic oxygen number density	$1/m^3$
ρ_{O2}	Oxygen number density	$1/m^3$
σ	Stefan-Boltzmann constant	W/m^2K^4
σ_f^2	Covariance for filter	
σ_s^2	Covariance for smoother	

Abbreviation	**Definition**	**Units**
ANDE-2	Atmospheric Neutral Density Experiment 2	
ANDE-RR	Atmospheric Neutral Density Experiment Risk Reduction	
AU	Astronomical Unit	AU
BCHL	Ballistic Coefficient Half-Life	

CHAMP	Challenging Minisatellite Payload
CIRA	COSPAR International Reference Atmosphere
CLL	Cercignani-Lampis-Lord
COSPAR	Committee on Space Research
CPF	Consolidated Prediction Format
CRD	Consolidated Range Data
DCF	Density Correction Factor
DRIA	Diffuse Reflection with Incomplete Accommodation
DS3V	Direct Simulation Three-Dimensional program
DSMC	Direct Simulation Monte Carlo
ECEF	Earth Centered Earth Fixed
EUV	Extreme Ultra-Violet
FMF	Free Molecular Flow
FUV	Far Ultraviolet Radiation

GFZ	Heimholtz Centre Potsdam GFZ German Research Centre for Geosciences in Potsdam, Germany
GITM	Global Ionosphere-Thermosphere Model
GRACE	Gravity Recovery And Climate Experiment
GSI	Gas-surface Interaction
HASDM	High Accuracy Satellite Drag Model
ILRS	International Laser Ranging Service
IR	Infrared
ITRF	International Terrestrial Reference Frame
JB2006	Jacchia-Bowman 2006
JB2008	Jacchia-Bowman 2008
LEO	Low Earth Orbit
MSISE	Mass Spectrometer Incoherent Scatter Extending from ground to space

MSISE-90	Mass Spectrometer Incoherent Scatter Extending from ground to space 1990	
MUV	Mid Ultraviolet Radiation	
NRLMSISE 2000	Naval Research Laboratory Mass Spectrometer and Incoherent Scatter Radar Extending from ground to space 2000	
ODTK	Orbit Determination Took Kit	
POE	Precision Orbit Ephemeris	
SFU	Solar Flux Unit	Watt/m^2 Hz
SLR	Satellite Laser Ranging	
SP	Sequential Processing	
SSN	Space Surveillance Network	
STK	Systems Tool Kit	
TPMC	Test Particle Monte Carlo	
UBSTD	Unbiased Standard Deviation	

Table of Figures

Table of Tables

1. Introduction

1.1. Objective

The research presented in this thesis provides corrections to current atmospheric density models through the analysis of Satellite Laser Ranging (SLR) data from satellites in Low Earth Orbit (LEO). The satellites analyzed in this paper are the spherical Atmospheric Neutral Density Experiment 2 (ANDE-2) satellites that were placed into orbit for the purpose of better determining the density of the atmosphere encountered by satellites in LEO. The spherical nature of the ANDE-2 satellites gives way to less uncertainty in the determination of their individual drag coefficients because their cross-sectional area doesn't change. Previous non-spherical satellites experienced changes in their drag coefficients and cross-sectional area due to the orientation of the satellite constantly changing. This research attempts to improve the accuracy of the drag coefficient estimates of the ANDE-2 satellites in order to better characterize the uncertainty in the estimated atmospheric density encountered by satellites in LEO.

1.2. Motivation

The future prediction of a satellite's location over a period of time becomes more difficult to determine with longer future predictions, and particularly so for satellites in LEO that experience large variations in atmospheric density and thermospheric winds. Hence, the ability to predict future collisions to operational satellites from other space objects becomes increasingly more difficult the further into the future the prediction for these events needs to be made. Thus, the motivation for this research is to obtain a more accurate method of predicting atmospheric density so that the future trajectories of satellites can be more precisely determined.

The importance behind the motivation for understanding changes in the upper atmosphere and its effects on satellites is clearly stated by Vallado (2007, p. 549), "Next to the oblateness of the Earth, atmospheric drag most strongly influences the motion of a satellite *near Earth*; in fact, during the last few

revolutions of the satellite's life, drag effects can be more dominant than those from the Earth's oblateness." Vallado (2007) further discuss the importance of atmospheric models for investigating the use of aerobraking and satellite tethers.

This research attempts to utilize the SLR data for the ANDE-2 satellites in unison with physics-based gas-surface interaction equations to determine more accurate and precise values for the drag coefficients of the ANDE-2 satellites. These new C_D values can then be used to make corrections to atmospheric models in hopes of achieving greater accuracy for satellite orbit predictions and the predicted lifespan of satellites.

1.3. Satellite Drag

According to Vallado (2007), the cause of drag on a satellite is due to the bombardment of tiny atmospheric particles against the satellite's outer shell, which over time slowly degrade the orbit of the satellite by reducing the total mechanical energy of the satellite. This ultimately results in a change of velocity for the satellite, and therefore a change in the semimajor axis and eccentricity of the satellite's orbit. Furthermore, this change in momentum of the satellite tends to occur around periapsis when the satellite is closest to the Earth, and thus the satellite encounters more atmospheric density and likewise more atmospheric drag. This will reduce the eccentricity of the satellite's orbit making the satellite's orbit more circular, which will ultimately bring the satellite closer to the Earth where the atmosphere is denser, resulting in more drag and a shorter lifespan for the satellite.

The basic atmospheric drag equation is given in Vallado (2007 p. 549) as

$$\vec{a}_{drag} = -\frac{1}{2}\frac{C_D A}{m}\rho\, v_{rel}^2 \frac{\vec{v}_{rel}}{|\vec{v}_{rel}|} \tag{1}$$

The variable $\vec{a}_{drag}$ is the acceleration due to atmospheric drag acting on the satellite while m and A are the mass and cross sectional area of the satellite, respectively. The drag coefficient of the satellite is C_D, which can be determined using three different methods: (1) a physical drag coefficient that is calculated by

measuring the exchange of momentum and energy between the satellite and atmospheric molecules, (2) a fitted drag coefficient that is specific to the atmospheric model being used and is estimated using the orbit determination process, or (3) a fixed drag coefficient that does not change (Pardini et al., 2010).

The values for the drag coefficients of satellites in LEO have generally been approximated to only two significant digits with 2.2 being the approximate drag coefficient value for satellites that are non-spherical and compact in shape, while for spherical satellites values of 2.0 to 2.1 have been used as approximate drag coefficient values (Vallado, 2007). Fixing the drag coefficient allows for the simplification of orbit determination calculations, but since it does not take into account changes in the density of the atmosphere relative to the satellite's altitude, or the change in cross sectional area of the satellite relative to the satellite's orientation, it cannot truly provide an accurate drag coefficient value for a satellite.

$\vec{v}_{rel}$ is the velocity vector of the satellite relative to the rotating atmosphere and is shown in equation (2) (Vallado 2007).

$$\vec{v}_{rel} = \frac{d\vec{r}}{dt} - \vec{\omega}_{\oplus} \times \vec{r} = \left[\frac{dx}{dt} + \omega_{\oplus} y \quad \frac{dy}{dt} - \omega_{\oplus} x \quad \frac{dz}{dt}\right]^T \tag{2}$$

The constant $\vec{\omega}_{\oplus}$ is the angular velocity of the Earth's atmosphere, while the variables $\vec{r}$ and $\frac{d\vec{r}}{dt}$ are the position and velocity vectors of the satellite. A more detailed version of this equation including wind variations van be found in Vallado (2007 p. 550).

The variable that is the most difficult to predict and determine accurately is the atmospheric density (ρ). The reason for this variability can be clearly seen in the following two equations. The first equation is the ideal gas law given by equation (3) (Vallado 2007), with (M) being the mean molecular mass of the atmosphere's constituents, (R) being the universal gas constant, and (g_0) being gravity.

$$\rho = \frac{p_0 M}{g_0 R T} \tag{3}$$

The two main variables in this equation are the Temperature (T) and the absolute pressure (p_0). The temperature of the atmosphere is one of the more difficult variables to predict in the equation. This is simply because of the variety of things that affect the temperature of the atmosphere such as: changes in solar flux, solar flares, sunspots, geomagnetic activity, winds in the thermosphere, diurnal variations in the atmosphere, and other celestial or terrestrial events.

The change in atmospheric pressure relative to height is given by the hydrostatic equation shown in equation (4) (Vallado 2007).

$$\Delta p = -\rho g_0 \Delta h \tag{4}$$

The variable (Δh) shows the change in height while the variable (Δp) is the change in pressure, both of which can contribute to the change in atmospheric density.

The last concept that will be introduced in this section is the ballistic coefficient (BC) which is a different way of representing how a satellite is affected by drag, and is the preferred way of representing satellite drag in the Orbital Determination Tool Kit (ODTK). The definition for the ballistic coefficient as it is defined in ODTK is shown in equation (5).

$$BC = \frac{c_D A}{m} \tag{5}$$

This representation of the ballistic coefficient is actually the inverse of the classical definition as given in Vallado (2007), and is used because a decrease or rise in BC will relate to a decrease or rise in the drag.

1.3.1. **Gas-Surface Interaction Models**

A way of physically determining the drag coefficient of a satellite is by using gas-surface interaction (GSI) models that attempt to estimate the C_D of a satellite by calculating the amount of energy transferred to the surface of the satellite by a reflected molecule. This allows for a physical drag coefficient to be calculated that is independent of the current atmospheric models being used in the analysis of satellite motion. When a particle hits the surface of the satellite, it transmits some of its energy to the satellite and then is reflected off the satellite's surface. However, not all particles are reflected in the same manner and can either stick to the satellites surface contaminating it (usually atomic oxygen) or be reflected in a specular, diffuse, or quasi-specular manner. One of the main variables in the GSI models is the accommodation coefficient (α), which quantifies the amount of kinetic energy lost by reflected particles that have struck the outer hull of the satellite as a fraction. This fraction is represented in equation (6).

$$\alpha = \frac{E_i - E_r}{E_i - E_w} \tag{6}$$

The variable *E* simply represents energy, while subscripts *i*, *r*, and *w* represent the incident, reflected and satellite surface/wall conditions (Watt and Moreton, 1964).

1.3.2. **Maxwell's Model**

The Maxwell model assumes that particles are reflected in either a specular or diffuse manner, and quantifies the distribution of specularly reflected particles as a fraction ε and the fraction of diffusely reflected particles as 1- ε. The Maxwell Model is the simplest GSI model, but is deficient according to molecular beam experiments that show particles are reflected in a quasi-specular manner (Hinchen and Foley, 1966). More sophisticated GSI models are generally used due to the Maxwell's models deficiency in this area.

1.3.3. **Diffuse Reflection with Incomplete Accommodation (DRIA)**

If the surface of a satellite is clean and smooth, it will reflect free-stream particles in a quasi-specular manner (Knechtel and Pitts 1969). However, satellites in LEO below 500 km commonly have surface contamination from atomic oxygen (Moe 1967), and data analyzed from pressure gauges and mass spectrometers have shown that satellites at altitudes around 150-300 km have surfaces that are covered in adsorbed oxygen (Moe and Moe, 1969; Moe et al., 1972; Hedin et al.,1973; Offermann and Grossmann, 1973). This results in the molecules being reflected in a diffuse pattern, which then lose a large portion of their kinetic energy. Hence, as the surface area of adsorbed molecules is increased over the satellite surface, so is the energy accommodation.

Satellites at higher altitudes have less surface contamination due to the density of atomic oxygen being significantly lower at higher altitudes. This results in lower energy accommodation and the incident molecules being reflected in an increasingly more quasi-specular manner. Evidence of this event has been shown in laboratory experiments (Saltsburg et al., 1967) and has also been shown in the data analysis of satellites in orbits at 800 to 1000 km (Harrison and Swinerd, 1995).

Satellites in circular orbits as low as 225 km may still have as much as 2 to 3 % of their striking molecules reflected in a quasi-specular manner (Gregory and Peters, 1987). And satellites with highly eccentric orbits (such as Molniya orbits) may have a lower accommodation coefficient near perigee (below 300 km) due to molecules striking the satellite surface at higher speeds making them less likely to be adsorbed to the surface (Moe and Moe, 2005). The different types of surface reflection experienced by particles in gas-surface interaction situations are detailed in Figure 1.

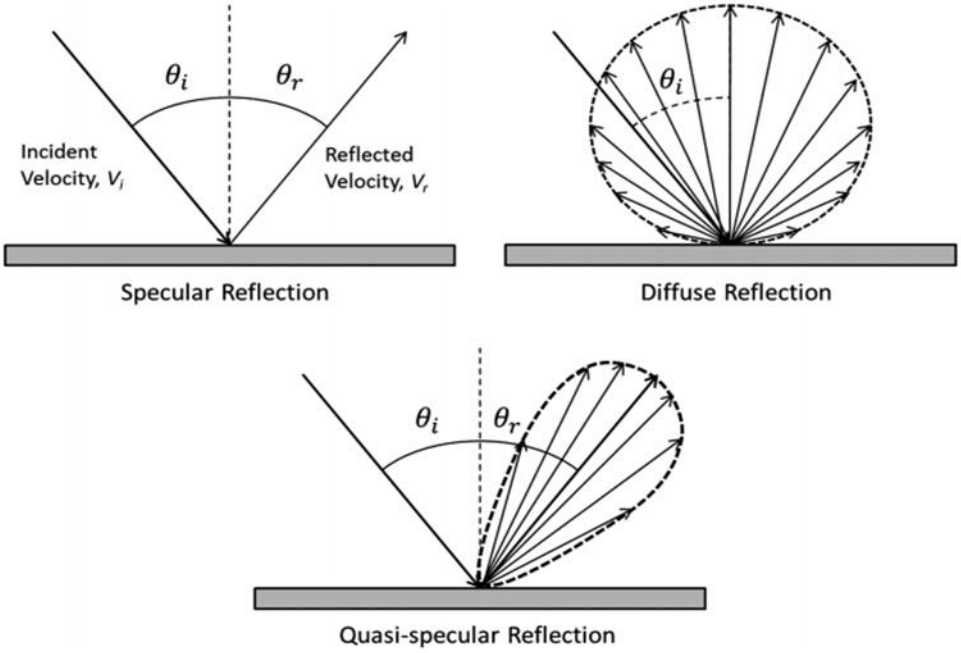

Figure 1: Representations of particle reflections during gas-surface interactions (Mehta et al. 2014)

1.3.4. **Cercignani-Lampis-Lord Model (CLL)**

The Cercignani-Lampis-Lord (CLL) GSI model attempts to use data from molecular beam experiments to theoretically match the distribution of reflected particles for satellite surfaces by specifying normal and tangential particle velocities for a scattering kernel (Cercignani and Lampis, 1971). The scattering kernel represents the velocity distribution of particles that strike a solid surface. If the surface of the satellite is isotropic the two tangential velocity components v and w act the same and are treated the same. Independent controlling parameters are defined as the normal energy accommodation coefficient (α_n) and tangential momentum accommodation coefficient (σ_t) for the mutually independent normal and tangential velocity scattering kernels. The scattering kernel equation for tangential velocity (v) is defined in equation (7) (Lord, 1991a).

$$P(v_i \longrightarrow v_r) = \frac{1}{\sqrt{\pi\sigma_t(2-\sigma_t)}} e^{-\frac{(v_r-(1-\sigma_t)v_i)}{\sigma_t(2-\sigma_t)}} \tag{7}$$

The term $P(v_i \longrightarrow v_r)$ in equation 7 is the probability of the incident tangential velocity component (v_i) being reflected as reflected tangential velocity component (v_r). Both velocity components v_i and v_r are measured in units of v_w, which is represented in equation (8) (Lord, 1991a).

$$v_w = \sqrt{\frac{2k_bT_w}{m_g}} \tag{8}$$

Where T_w is the surface temperature of the satellites outer hull, k_B is the Boltzmann constant, and m_g is the average molecular mass of the atmosphere at the satellite's altitude. A similar relation is used for the second tangential component *w*. The tangential momentum accommodation coefficient σ_t can be related to the tangential energy accommodation coefficient α_t using equation (9) (Lord, 1991a).

$$\alpha_t = \sigma_t(2-\sigma_t) \tag{9}$$

The energy accommodation coefficient α can be related to α_t and α_n using equation (10) (Lord, 1991a)

$$\alpha = \frac{\alpha_n + \alpha_t}{2} \tag{10}$$

The normal velocity component *u* also has a scattering kernel, but is represented by a different equation from the tangential velocity components *v* and *w*. This is due to particles hitting the outer hull of the spacecraft having a velocity distribution that is biased toward particles traveling at a higher velocity, and because the normalization condition for *u* is integrated between 0 and ∞ due to it always being positive. The scattering kernel equation for *u* is given in equation (11) (Lord, 1991a).

$$P(u_i \longrightarrow u_r) = \frac{2u_r}{\alpha_n} I_0\left(\frac{2\sqrt{1-\alpha_n}u_r u_i}{\alpha_n}\right) e^{-\frac{u_r^2+(1-\alpha_n)u_i^2}{\alpha_n}} \tag{11}$$

I_0 is the modified Bessel function of the first kind and order zero, and the probability that the normal incident velocity u_i is reflected as the normal reflected velocity u_r is represented by $P(u_i \longrightarrow u_r)$. An extension of the CLL model allows for modeling Diffuse Reflection with Incomplete Accommodation and was developed by Lord (1991b).

1.4. Computational Gas-Surface Interaction Methods

A few computational methods exist for the analysis of satellites undergoing Free Molecular Flow (FMF), including Test Particle Monte Carlo (TPMC) and Direct Simulation Monte Carlo (DSMC). Both of these models do a good job at computing C_D for satellites in FMF with TPMC being less computationally expensive. However, TPMC does not perform as well as DSMC in areas of the atmosphere where GSI interactions are less dominant. A way of determining what type of flow is being experienced by a satellite, is by calculating the non-dimensional Knudsen number (K_n) which is the ratio between the mean distance molecules travel between subsequent collisions (λ) and the length of the spacecraft (L_{ref}). The Knudsen number can be calculated using equation (12).

$$K_n = \frac{\lambda}{L_{ref}} \tag{12}$$

The mean free path (λ) can be calculated using equation (13).

$$\lambda = \frac{k_b T}{\sqrt{2}\pi d_{avg}^2 p} \tag{13}$$

k_b is the Boltzman constant, p is the ambient pressure of the gas, T is the kinetic temperature of the gas, and d_{avg} is the mean collision diameter (Bird, 1994 and Graziano, 2007). Figure 2 shows the establishment of flow based on the Knudsen number.

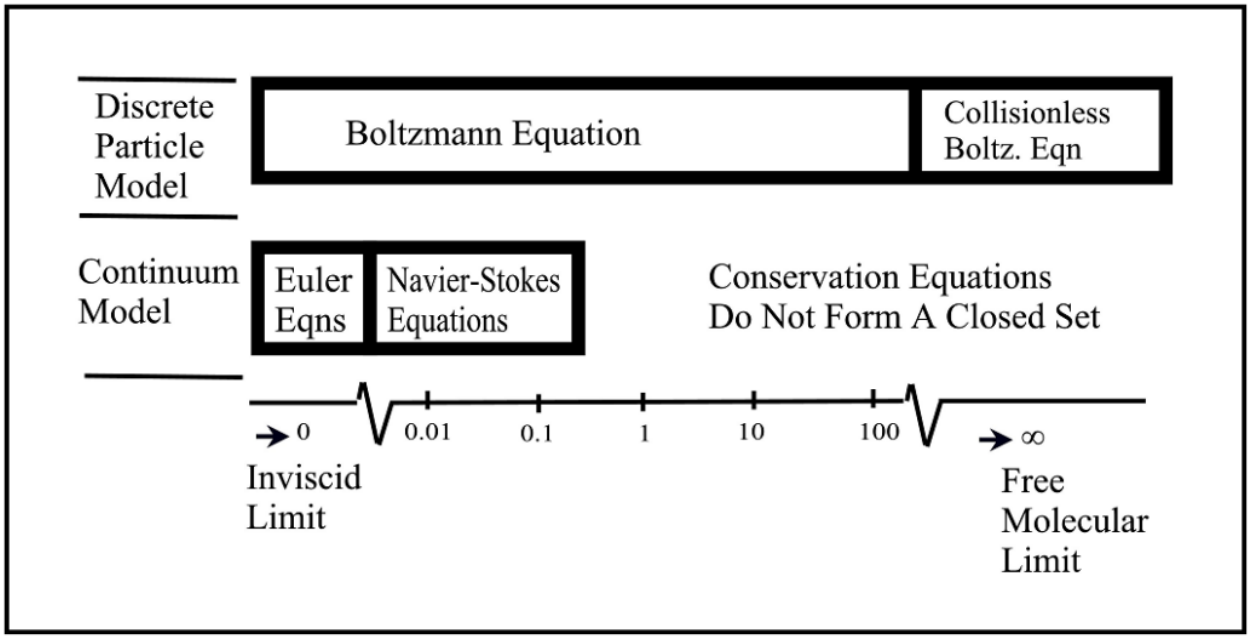

Figure 2: Flow establishment based on Knudsen number, taken from Bird (1994)

Satellites above 200 km generally have a Knudsen number above 10 with inter-molecular collisions being very rare at those altitudes and GSIs being dominate. With K_n<10 inter-molecular collisions become more common and GSIs become less common, this is where the TPMC method begins to experience problems in accurately computing the C_D of a satellite and the DSMC method should be used instead.

1.4.1. **Test Particle Monte Carlo**

TPMC is a computational method that attempts to model gas-surface interactions through the use of test particles, which represent a large number of actual molecules. The test particles are fired at the surface of the satellite to simulate GSIs with a constant free-stream bulk velocity and thermal velocity that is determined probabilistically. The TPMC method has the ability to model particles reflected off of complex concave geometries as well as flow shadowing. The test particles do not, however, experience intermolecular collisions, which is why the TPMC method is not ideal for transitional flows and is used primarily for FMF analysis instead (Mehta, 2013).

1.4.2. **Direct Simulation Monte Carlo**

A method similar to TPMC, but with the ability to model transitional and continuum flows is the DSMC method, which was created in 1963 by Graeme Bird (Bird, 1963). The DSMC method uses stochastic processes and kinetic theory in order to track the simulated particles' interaction with the satellite surface, as well as intermolecular collisions and boundary conditions using probability. The movements of each molecule are tracked independently in the program and information regarding energy, velocity, and position are stored in the program. As interactions between the surface, other molecules, and boundary conditions take place, the information regarding each particle is updated and saved in the program's memory. The object being analyzed in the program is inserted as a surface mesh while molecules are projected at the surface in a flow field. A large flow environment (like the Earth's atmosphere) is used in the simulation and is often set to free-stream boundary conditions allowing for molecules to either enter or leave the computational realm of the program (Mehta, 2013).

1.4.2.1. Direct Simulation Three-Dimensional Visual Program

One variation of the DSMC code is the Direct Simulation Three-Dimensional Visual Program (DS3V) which was also developed by Graeme Bird (Bird, 1963). The program sets all variables automatically except for the number of megabytes required for initial storage space, which determines the number of cells that will be used in discretizing computations and does not allow for the user to specify the accommodation coefficient. The default setting in DS3V for the accommodation coefficient is complete accommodation, and the two GSI models that the program uses are the Maxwell model and CLL model (Bird, 2006). The program can however, be tricked into modeling diffuse reactions with incomplete accommodation according to Mehta in section 3.1 of his dissertation (Mehta, 2013). The DS3V code is free and available on the internet at www.gab.com.au.

1.4.2.2. DSMC Analysis Code

The National Aeronautics and Space Administration developed the DSMC Analysis Code (DAC) for the purpose of studying rarefied gas dynamic scenarios which are encountered during the re-entry of space vehicles. DAC also uses the Maxwell GSI model and CLL GSI model, but can model DRIA interactions by using the Lord extension of the CLL model (Lord, 1991a). The DAC program, unlike the DS3V program, is not free or available to citizens outside the U.S., but does allow access to open-source code.

The DAC program is faster than the DS3V program due to its ability to use batch processing in CLL GSI simulations and specifies the time step and statistical weight for the simulated molecules relative to gas conditions. Research involving this model was done in collaboration with the Los Alamos National Laboratory and the University of Kansas in Mehta (2013) with simulations performed by Dr. Andrew Walker from the Los Alamos National Laboratory.

1.5. Solar and Geomagnetic Activity

Solar and geomagnetic activity are major factors in determining the density of the atmosphere because of the heating effect solar activity has on the atmosphere from solar radiation and the ionization of the atmosphere that occurs during fluctuations in geomagnetic activity. Data bases currently exist for solar flux and geomagnetic indices so that the effects these disturbances have on the atmosphere can be utilized by atmospheric models, as well as any other type of research that may require raw data from these sources.

Some programs that are utilized for orbit determination such as the Orbit Determination Tool Kit (ODTK) and Systems Tool Kit (STK) from Analytical Graphics, Inc., already have solar and geomagnetic data included in the program. For programs that require this data but do not have it included in the program package, information regarding the raw data for solar flux and geomagnetic indices can be found online on a few websites. Daily solar flux data normally are distributed on the National Geophysical Data Center's

website (2015a). The data used in this research for the daily solar flux were taken from the Natural Resources Canada website (2015).

Geomagnetic indices can also be found on the National Geophysical Data Center's website (2015b), which were taken from the Heimholtz Centre Potsdam GFZ German Research Centre for Geosciences in Potsdam, Germany (commonly called GFZ for short). The Geomagnetic indices can also be found on the GFZ's website (GFZ, 2015).

1.5.1. **Solar Indices**

As mentioned previously, the solar activity from the sun affects the atmospheric density by warming the atmosphere with incoming solar radiation also known as solar flux or *Extreme Ultra-Violet* (EUV) radiation. EUV radiation does not pass through the atmosphere to the Earth's surface and hence cannot be measured from Earth's surface; instead incoming solar radiation with the wavelength 10.7 cm or frequency of 2800 MHz is measured at the Earth's surface. This is due to the fact that 10.7 cm radiation (also known as $F_{10.7}$) originates in the same part of the Sun's chromosphere and corona, has the same relative strength as EUV radiation, and is capable of being transmitted through the Earth's atmosphere without being stopped. The units of measurement for solar flux are *Solar Flux Units* (SFU), where the value for one SFU is given below.

$$1\,SFU = 1 \times 10^{-22}\,\frac{watt}{m^2/Hz} \tag{14}$$

The values for daily solar flux are distributed using this unit scale and are distributed on the websites previously mentioned (National Geophysical Data Center, 2015a and Natural Resources Canada, 2015).

Since the solar flux is measured at the surface of the Earth (known as observed solar flux), the solar flux measurements may not exactly represent the actual solar activity for that day, this is because of the elliptical orbit of Earth. Because of this, two forms of measurement exist for solar flux: the observed value, and the adjusted value. The observed value is used for terrestrial related experiments and studies, and the

adjusted value is for solar experiments and studies. The adjusted value is found by using the observed value and adjusting it for one *Astronomical Unit* (AU) or 149,597,870.66 km, which is the average distance of Earth from the Sun. The adjusted to observed solar flux conversion is given in equation (15) (Vallado 2007).

$$F_{10.7}(obs) = \frac{F_{10.7}(adj)AU^2}{r_{\oplus-sun}^2} \tag{15}$$

Some atmospheric models require the adjusted solar flux measurements to make predictions about the solar flux values for the day of interest, as well as 81-day averages that are either centered on the day of interest or precede the day of interest.

The daily solar flux levels can be described in four different ways: Low, Moderate, Elevated, and High. The allowed variations in solar flux for each level are shown in Table 1 and are based on Picone et al (2002).

Table 1: Solar Activity Levels

$F_{10.7}$ Solar Activity Levels	
Low	$F_{10.7}<75$
Moderate	$75<F_{10.7}<150$
Elevated	$150<F_{10.7}<190$
High	$F_{10.7}>190$

1.5.2. **Geomagnetic Indices**

The Earth's magnetic field has four effects on satellite operations according to Vallado (2007). The four effects on satellite operations according to Vallado (2007) are: (1) charged particles from magnetic changes cause ionization of the atmosphere altering both the density of the atmosphere and drag forces on satellites. (2) Charged particles can cause the surface of the satellite to become more attractive to other particles in the atmosphere, which can alter the satellites drag coefficient. (3) The ionization of the atmosphere can cause interference with the satellites communication systems as well as satellite tracking. (4) Electromagnetics onboard the satellite for attitude maneuvers can be interfered with by charged particles in the atmosphere during magnetic field disturbances. The two effects that the magnetic field has on satellites that are of greatest interests for this paper are effects (1) and (2).

The activity in the magnetic field is measured using what is known as the geomagnetic *planetary index*, K_p which is a quasi-logarithmic worldwide average of the geomagnetic activity below the auroral zones. The geomagnetic activity is measured as a K value by twelve stations every three hours and then averaged to form the worldwide K_p value. These values of K_p vary from 0 to 9, and can be converted into what is known as the geomagnetic *planetary amplitude*, a_p which is for every three hours, and averaging these eight 3-hour a_p indices yields the geomagnetic *daily planetary amplitude*, A_p. The A_p is measured in gamma units where one unit gamma is 10^{-9} Tesla or 10^{-9} (kg s/m). The conversion for K_p to a_p is given in Vallado (2007) and is shown in Table 2.

Table 2: Kp and ap values

K_p	0o	0+	1-	1o	1+	2-	2o	2+	3-	3o	3+	4-	4o	4+
K_p	0	0.33	0.67	1	1.33	1.67	2	2.33	2.67	3	3.33	3.67	4	4.33
a_p	0	2	3	4	5	6	7	9	12	15	18	22	27	32
K_p	5-	5o	5+	6-	6o	6+	7-	7o	7+	8-	8o	8+	9-	9o
K_p	4.67	5	5.33	5.67	6	6.33	6.67	7	7.33	7.67	8	8.33	8.67	9
a_p	39	48	56	67	80	94	111	132	154	179	207	236	300	400

The daily planetary amplitude tends to not reach values over 100, and is generally nearer to the 10 to 20 range. The geomagnetic activity is also separated into three different levels: quiet, moderate, and active. These levels are shown in Table 3 based on Picone et al. (2002). The A_p also follows two different cycles related to the Sun. First is the 11-year sunspot cycle with the largest values for A_p towards the end of the 11-year cycle, and second is a semi-annual cycle that involves the variable position of the solar wind in relation to the magnetosphere of the Earth. Both cycles are difficult to predict and additional influences on the A_p from solar flares, coronal holes, disappearing solar filaments, and the solar wind environment at Earth all assist in making the A_p more difficult to predict.

Table 3: Geomagnetic Activity Levels

A_p Geomagnetic Activity	
Quite	$A_p<10$
Moderate	$10<A_p<50$
Eleavated	$50<A_p$

1.6. Atmospheric Models

1.6.1. Jacchia 1971 Atmospheric Model

The Jacchia 1971 model was created by updating the Jacchia 1970 model to include new atmospheric composition and density findings from mass spectrometer and EUV-absorption data. The new model starts analysis by assuming a sea-level mean molecular mass boundary condition at 90 km, and then varies the mean molecular mass from 90 to 100 km using an empirical model for mean molecular mass. From 100 to 150 km a diffusion model for mean molecular mass is used to take into account the dissociation of oxygen at higher altitudes. The diffuse model used assumes a ratio of 9.2 for O/O_2 at 150 km for an exospheric temperature of 900 to 1000 K and adjusts the temperature from 90 to 150 km so that this condition is met. The temperature profile starts at a height of 90 km with a temperature value of 183K, and then rises till it reaches a point of inflection at 125 km where the temperature approaches the exospheric temperature in an asymptotic manner. Additionally, the Jacchia 1971 model uses a running 81-day solar flux and geomagnetic average to help smooth out short term variations in solar activity such as the 27-day solar cycle (Jacchia, 1971).

1.6.2. CIRA 1972 Atmospheric Model

The CIRA 1972 model is a semi-theoretical model (with some free variables) for determining the mean atmospheric density, and was released by the Committee on Space Research (COSPAR). The original CIRA 1965 model was updated to the CIRA 1972 by including the Jacchia 1971 model's variations in the atmosphere from 110 to 2000 km, and mean atmospheric density values from 25 to 500 km. The CIRA 1972 model gets most of its data from satellite drag and ground-based measurements (COSPAR Working Group IV, 1972 and Vallado, 2007).

1.6.3. **Jacchia-Bowman 2008 Atmospheric Model**

The Jacchia-Bowman 2008 model (JB2008) was created as the replacement to the Jacchia-Bowman 2006 model (JB2006), which is based on Jacchia's diffusion equations. Previous atmospheric models before the JB2006, lacked the ability to model the periodic fluctuations in the ultraviolet radiation due to the 27-day solar cycle, and produced large atmospheric density errors over 27-day periods. Previous models also did a poor job of modeling semiannual density variations in the atmosphere and the effects of geomagnetic activity. JB2008 attempts to model atmospheric density with more accuracy by using new solar indices, a new geomagnetic index model, and a semiannual atmospheric density model (Bowman et al., 2008).

The JB2008 uses atmospheric density data obtained from four different sources: daily density values from drag analysis of multiple satellites with perigee altitudes ranging from 175 to 1000 km obtained by the Air Force over the period of 1997 to 2007, density values from 2001 to 2005 from the Air Force's High Accuracy Satellite Drag Model (HASDM), CHAMP accelerometer obtained densities from 2001 to 2005, and GRACE accelerometer obtained densities from 2002 to 2005 (Bowman et al., 2008).

The JB2008 uses four different solar indices for its temperature equation. This includes $F_{10.7}$ radiation with the addition of three ultraviolet heating indices: $S_{10.7}$, $M_{10.7}$, and $Y_{10.7}$. These new ultraviolet heating indices represent the effects of extreme ultraviolet radiation (EUV), far ultraviolet radiation (FUV), and mid ultraviolet radiation (MUV). The 81-day centered average for each solar index is used to calculate the atmospheric temperature in order to provide a better estimate of atmospheric density than the previous model (JB2006) which did not use the $Y_{10.7}$ indices (Bowman et al., 2008).

1.6.4. **NRLMSISE 2000 Atmospheric Model**

The NRLMSISE 2000 model was developed by the Naval Research Laboratory as an update to the previous Mass Spectrometer Incoherent Scatter Rader (MSIS) model MSISE-90. The new model incorporates atmospheric density from satellite accelerometers, orbit determination (some of this data

includes Jacchia and Barlier data sets), incoherent scatter radar temperature readings from 1981 to 1997, and molecular oxygen density numbers determined from solar ultraviolet occultation readings on the Solar Maximum Mission satellite (Picone et al. 2002).

An advantage of the NRLMSISE 2000 model is that it uses less code for calculating atmospheric density than some other models (such as the Jacchia models) and also gives the number densities of major atmospheric constituents. However, because the NRLMSISE 2000 model requires more computations to be made to produce a result, the NRLMSISE 2000 model runs slower than the Jacchia models. Also, in some instances the NRLMSISE 2000 model may be out-performed by some Jacchia based models (Vallado, 2007).

1.7. Satellites Examined

1.7.1. ANDE-2

The Atmospheric Neutral Density Experiment-2 (ANDE-2) is the follow-up mission for the original Atmospheric Neutral Density Experiment Risk Reduction (ANDE-RR) mission, with the objective to provide new data on atmospheric density from an initial altitude of 350 km. The mission consisted of two spherical satellites fitted with 30 optical retro reflectors (for tracking) of the same diameter, with one active satellite (Castor) and one inactive satellite (Pollux). The satellites where purposely made to have different masses with the Castor satellite being about 20 kg heavier, so that the non-conservative forces acting on the satellites would cause them to separate slowly over time. The active satellite (Castor) had an on-board spectrometer for wind and temperature data as well as a GPS receiver. Both satellites where tracked using Satellite Laser Ranging (SLR) by the International Laser Ranging Service (ILRS) network and the Space Surveillance Network (SSN) and operated during solar minimum conditions (Earth Observation Portal, 2015). The satellite characteristics for ANDE-2 were taken from Lechtenberg (2015) and Earth Observation Portal (2015) and are shown in Table 4.

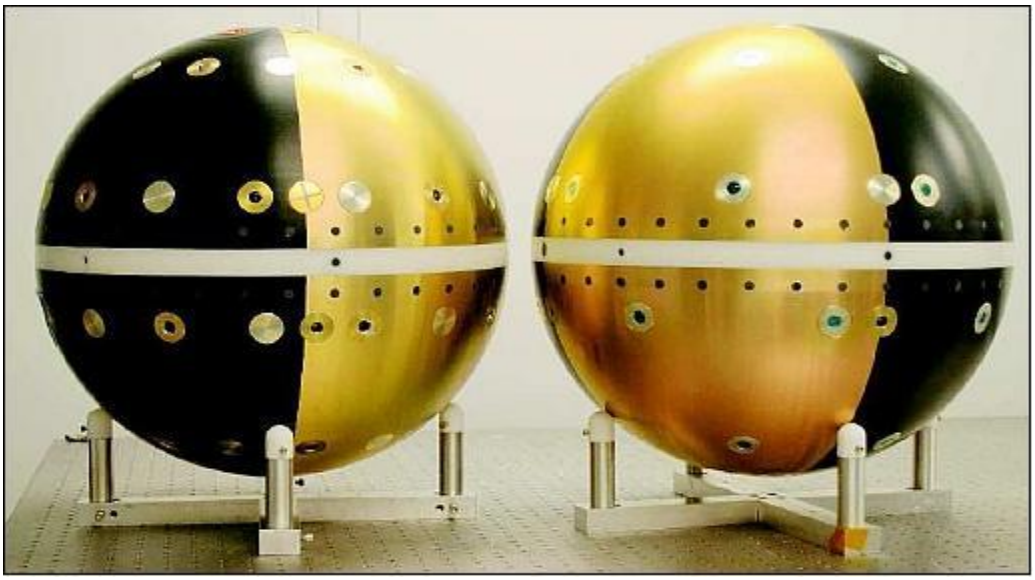

Figure 3: The two ANDE-2 satellites: Castor (left) and Pollux (right)

Table 4: Satellite Characteristics for ANDE-2 (Earth Observation Portal, 2015)

Satellite	Launch Date	Re-entry Date	Mass (kg)	Cross-Sect Area (m^2)	Initial Altitude	Inclination (degrees)
ANDEc	Jul. 30, 2009	Aug. 18, 2010	47.45	0.182921	350	51.6
ANDEp	Jul. 30, 2009	Mar. 28, 2010	27.4	0.182921	350	51.6

1.8. Previous Research Involving the Drag Coefficients of Spherical Satellites

Various research regarding the C_D of spherical satellites due to GSIs have been performed by multiple researchers using the previously mentioned models and programs, as well as other methods. The vast majority of research involving the determination of the C_D is performed relative to parameters such as the accommodation coefficient, momentum accommodation coefficient, the temperature of the atmosphere, the temperature of the satellites surface, altitude, the velocity of the satellite, solar minimum and solar maximum, as well as other parameters.

The material in this section will mostly be derived from the research of Mehta (2013, 2014), Pilinksi et al. (2010, 2011), and Walker et al. (2014). In the work of Mehta (2013, 2014) and Walker et al. (2014)

variables are set to constant values while the variable of interest is being varied. The constant values for these variables are T_W = 300 K, T_∞ = 1100 K, v_{rel} = 7500 m/s, and $\alpha = 1$. Also, the variable values chosen for the C_D range are values used for computing the C_D in the DS3V program.

1.8.1. **Effects of Temperature Variation on the Drag Coefficient**

Mehta (2013) provided the information shown in Figure 4, which shows the sensitivity of the C_D for various satellite shapes relative to the satellite's surface temperature. The surface temperature of the satellite is varied to simulate the differences in satellite's surface during nighttime and daytime operations. The range of C_D according to Mehta (2013) is given in Table 5 for the expected surface temperature range of 183 K to 465 K.

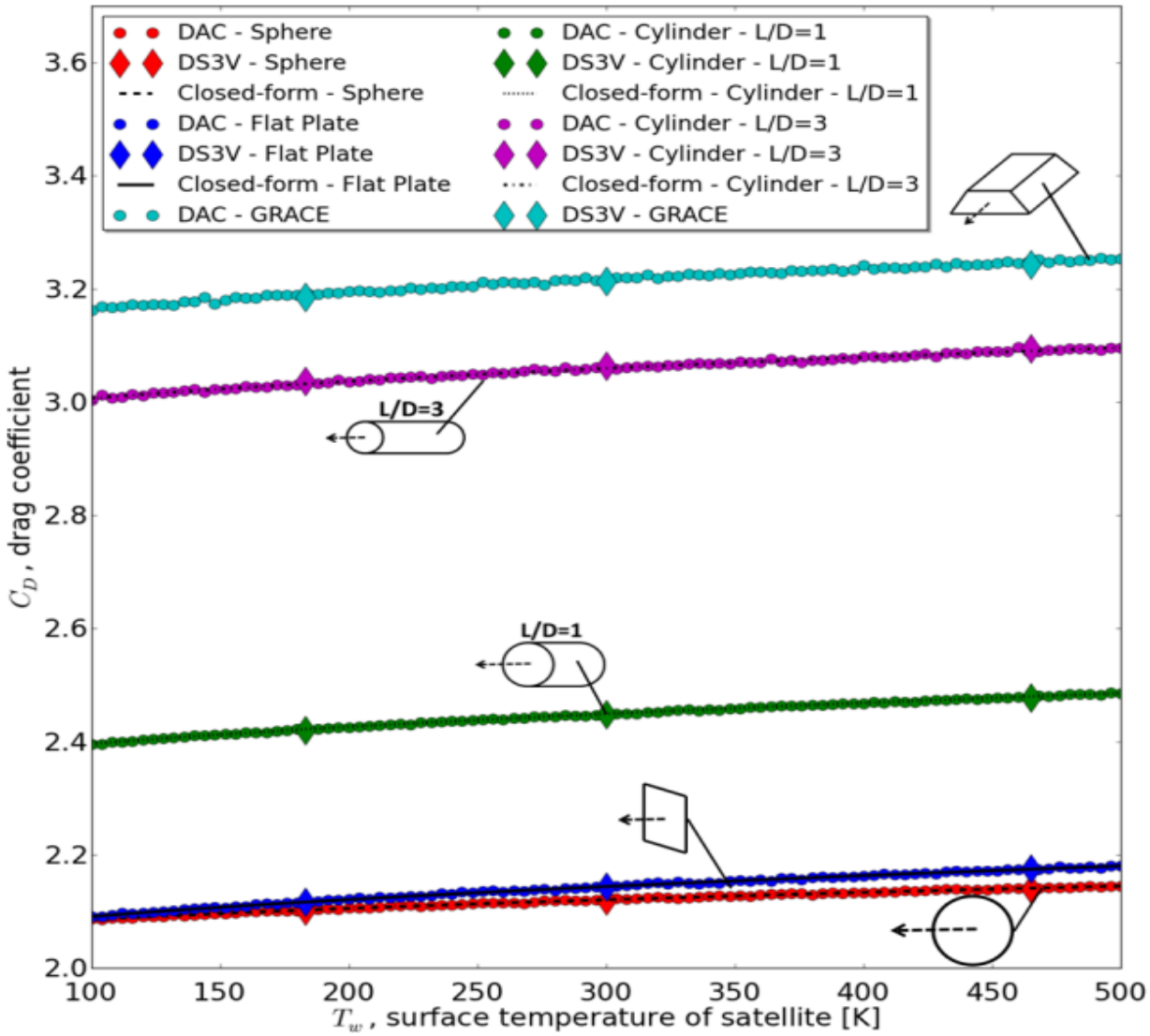

Figure 4: Drag coefficient sensitivity relative to surface temperature for different satellite geometries (Mehta, 2013)

Table 5: C_D values from Figure 4

Satellite	183^o K	465^o K
Sphere	2.10	2.14
Flat Plate	2.12	2.18
Cylinder L/D=1	2.42	2.48
Cylinder L/D=3	3.03	3.09
GRACE	3.19	3.24

Mehta (2013) also provided information on the sensitivity of the C_D for various satellite shapes relative to the atmospheric translational temperature. In Figure 5 the atmospheric translational temperature is varied from 200 K to 2000 K to simulate differences in temperature for night and daytime temperature variations. The range of C_D according to Mehta (2013) is given in Table 6 for the expected atmospheric translational temperatures of 700 K and 1500 K.

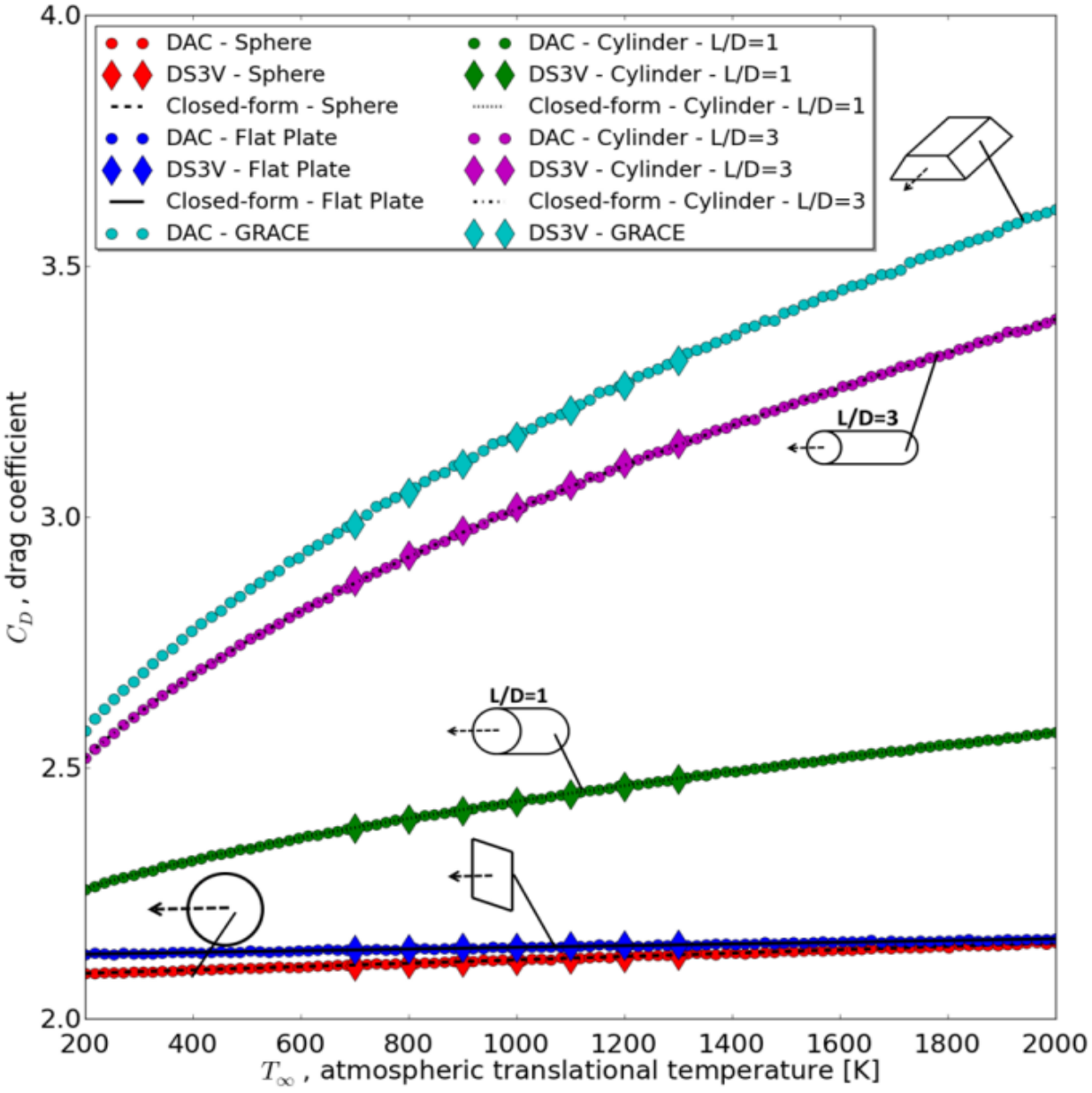

Figure 5: Drag coefficient sensitivity relative to atmospheric translational temperature for different satellite geometries (Mehta, 2013)

Table 6: C_D values for Figure 5

Satellite	700° K	1500° K
Sphere	2.11	2.14
Flat Plate	2.14	2.15
Cylinder L/D=1	2.11	2.51
Cylinder L/D=3	2.87	3.22
GRACE	2.99	3.41

1.8.2. **Effects of Altitude Variation on the Drag Coefficient**

Changes in satellite altitude results in the complexity of drag coefficient calculations due to the variations of multiple GSI variables, namely, the accommodation coefficient, the temperature of the atmosphere, the temperature of the satellite's surface, and the mean molecular mass of the atmosphere. Variations in the solar activity only add to list of these complications since solar activity directly effects all four of the variables listed above. Pilinski et al. (2011) used closed-form solutions (derived from modified Sentman (1961) equations) assuming diffuse reflection with incomplete accommodation in free molecular flow, in unison with the NRLMSISE 2000 model to determine the atmospheric temperature and mean molecular mass. Pilinski et al. (2011) determined the accommodation coefficient through interpolation with information obtained from Bowman and Moe (2006) for solar minimum and maximum conditions. This subject is summarized in section 1.9.5 of this thesis, and can be found in Pilinski et al. (2010). Figure 6 shows Pilinski et al. (2011) results for the C_D of a flat plate and sphere during solar minimum and maximum conditions. The constant parameters for this plot are T_W = 300 K, T_∞ = 900 K, and v_{rel} = 7800 m/s.

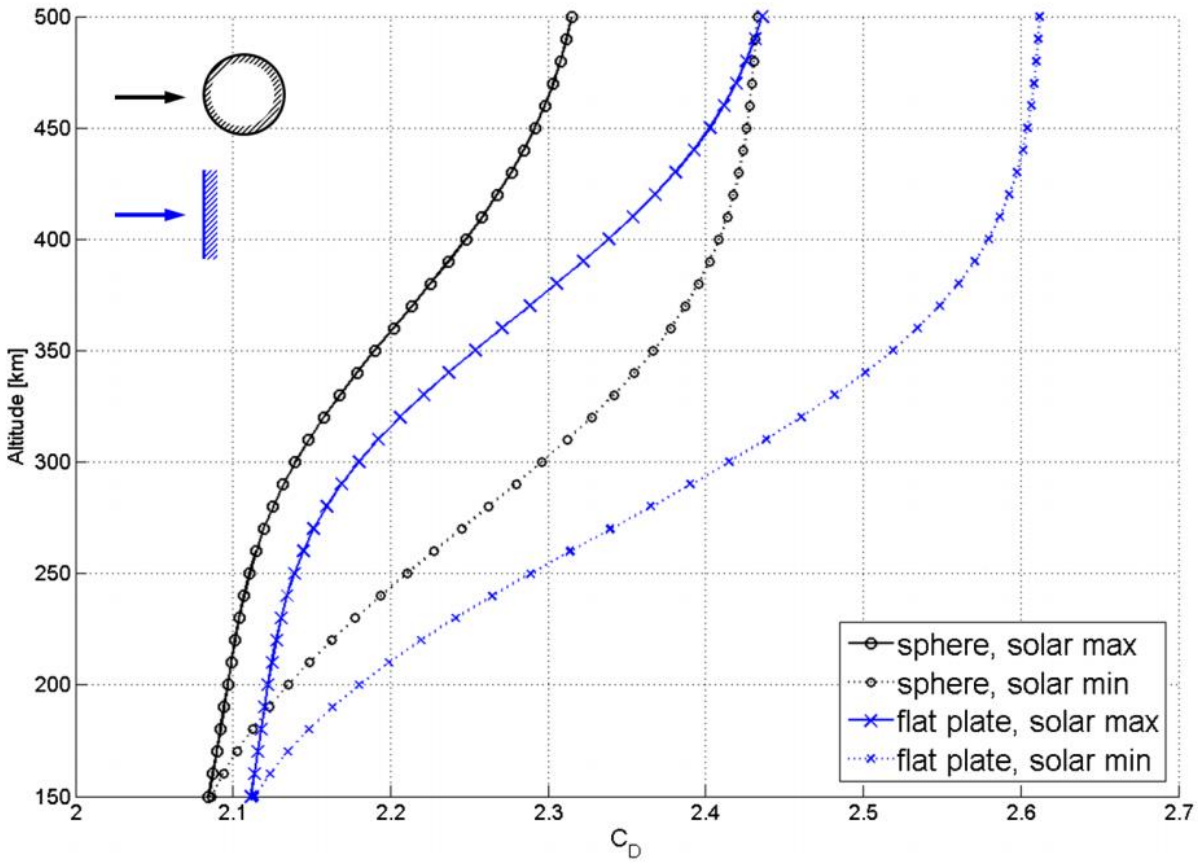

Figure 6: Drag coefficient for a sphere and flat plate during solar minimum and solar maximum conditions (Pilinski, 2011)

Moe and Moe (2006) give a similar graph for the C_D of four satellite shapes during solar minimum using the same closed-form solutions as Pilinski et al. (2011). Figure 7 shows the results obtained by Moe and Moe (2006).

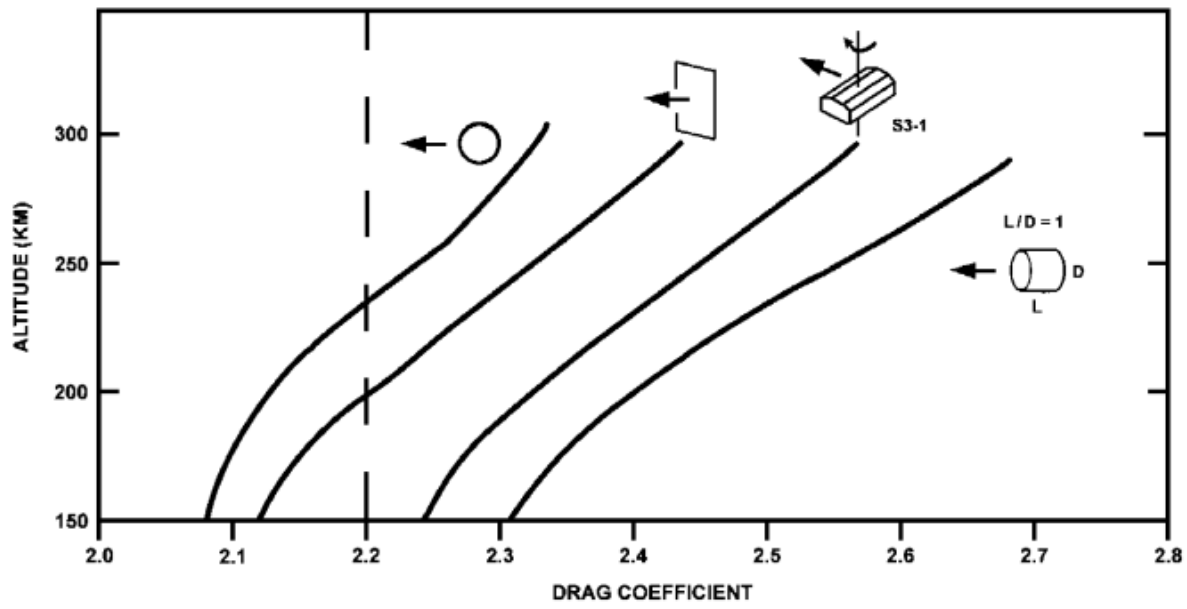

Figure 7: Drag Coefficients for four satellites shapes during solar minimum (Moe and Moe, 2006)

Additional graphs for solar minimum and solar maximum conditions for a variety of satellite shapes can be found in the work of Walker et al. (2014). The atmospheric models used by Walker et al. (2014) are the NRLMSISE 2000 atmospheric model (referred to as MSISE in the figures provided by Walker et al. (2014)) and the Global Ionosphere-Thermosphere Model (GITM). The graphs provided by Walker et al. (2014) are shown in Figure 8 and Figure 9 and are computed using the CLL GSI model.

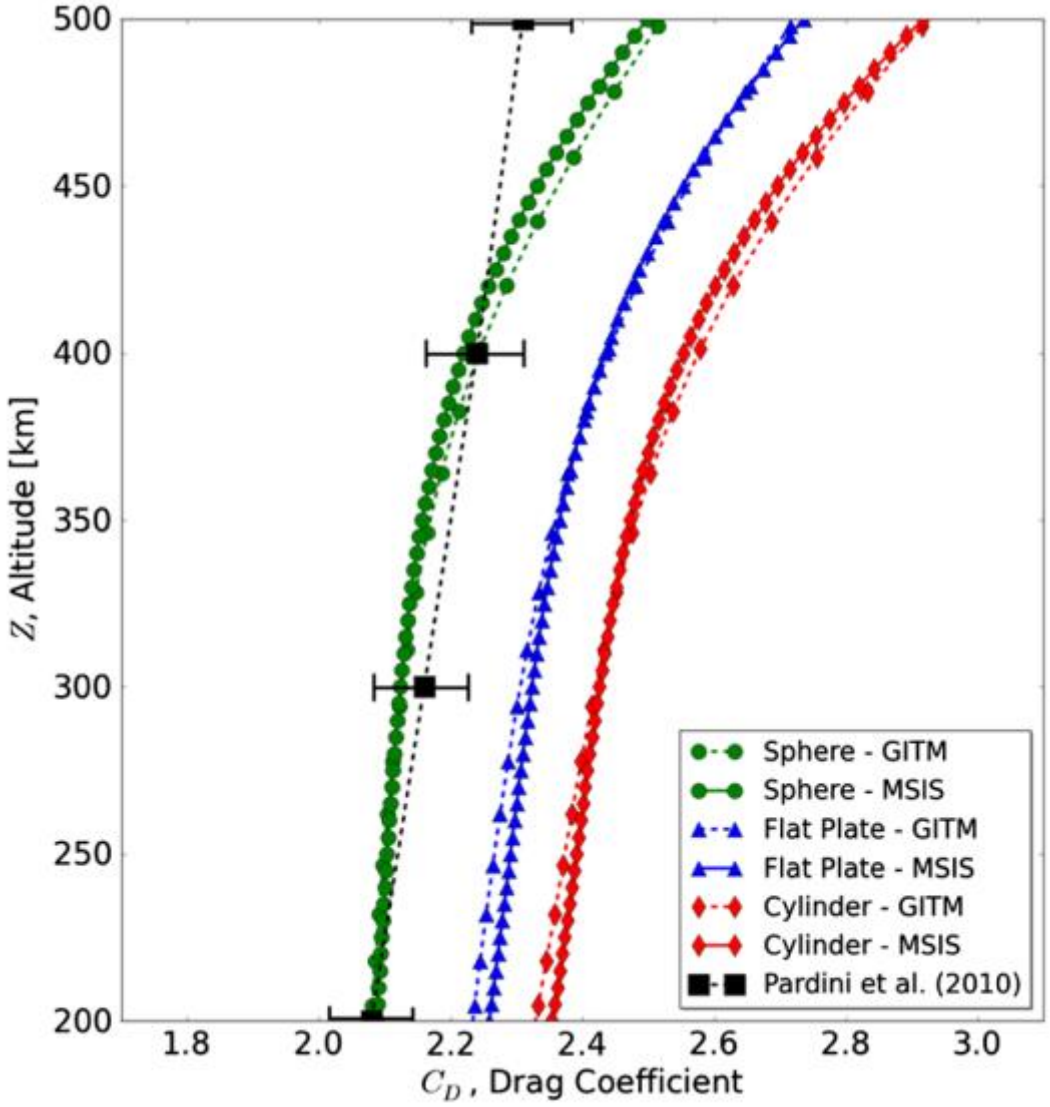

Figure 8: C_D vs. altitude for solar maximum conditions (Walker et al., 2014)

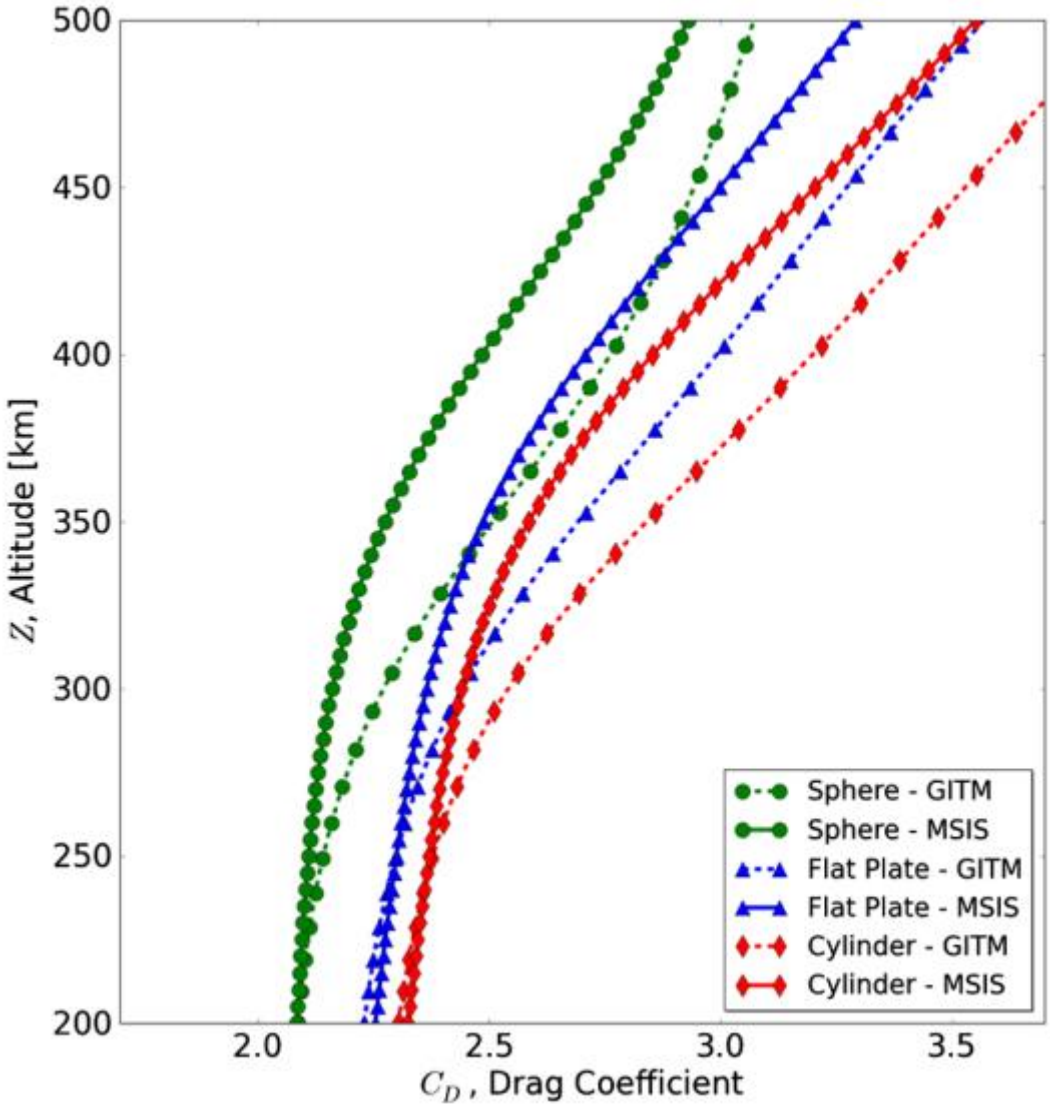

Figure 9: C_D vs. altitude for solar minimum conditions (Walker et al., 2014)

1.8.3. **Effects of Velocity Variation on the Drag Coefficient**

Mehta (2013) provided the information shown in Figure 10, which shows the sensitivity of the C_D for various satellite shapes relative to the velocity of the satellite. The velocity of the satellite is varied to simulate the differences in the satellite's altitude. The range of C_D according to Mehta (2013) is given in Table 7 for the expected velocity range of 6 to 9 km/s.

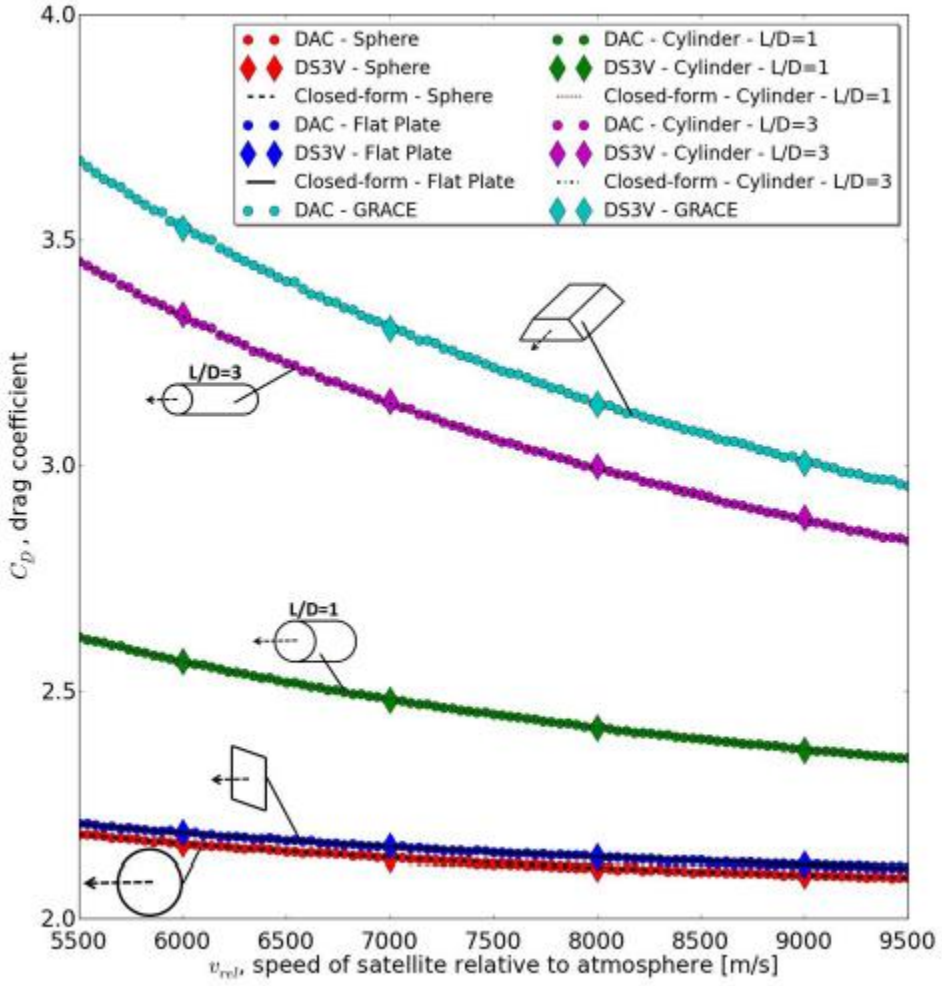

Figure 10: Drag coefficient sensitivity relative to velocity for different satellite geometries (Mehta, 2013)

Table 7: C_D values for Figure 10

Satellite	6 km/s	9 km/s
Sphere	2.16	2.08
Flat Plate	2.19	2.12
Cylinder L/D=1	2.56	2.33
Cylinder L/D=3	3.33	2.88
GRACE	3.53	3.90

1.8.4. **Effects of Accommodation Coefficient Variation on the Drag Coefficient**

Mehta (2013) in his analysis of the sensitivity of the C_D relative to the accommodation coefficient used two GSI models: The DRIA model and the CLL model, in order to simulate the effects varying the accommodation coefficient has on the C_D. Mehta used the DS3V program to compute the C_D with the DRIA model and the DAC to compute the C_D with the CLL model. The CLL model only produced results for an accommodation coefficient range from 0.5 to 1 since it requires the user to input a value for α_n and σ_t and assumes α_t and σ_t to be FMF unity. More information on this subject can be found in section 3.1.5 of Mehta's dissertation (2013). The values of C_D for the given range of α are shown in

Table 8.

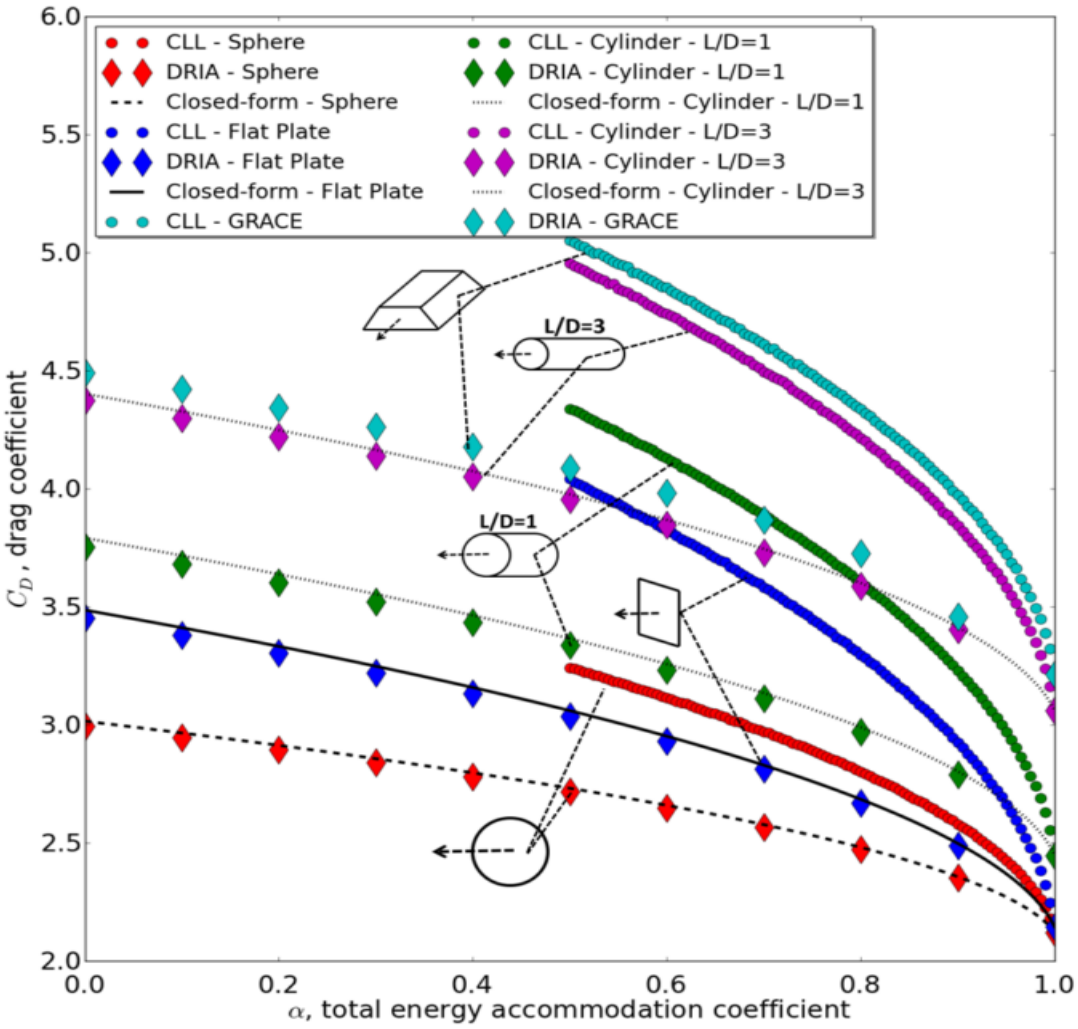

Figure 11: Drag coefficient sensitivity relative to the accommodation coefficient for different satellite geometries (Mehta, 2013)

Table 8: C_D values for Figure 11

Satellite	DRIA α=0.5	DRIA α=1	CLL α=0.5	CLL α=1
Sphere	2.72	2.12	3.05	2.12
Flat Plate	3.04	2.14	4.05	2.14
Cylinder L/D=1	3.34	2.45	4.35	2.45
Cylinder L/D=3	3.96	3.06	4.97	3.06
GRACE	4.09	3.21	5.09	3.21

1.8.5. **Previous Research on the Range of the Accommodation Coefficient for Spheres**

As mentioned earlier, the range of α used in the research of Pilinski et al. (2011) came from previous research performed by Bowman and Moe (2006), where the orbits of seven spherical satellites over the period of 1989-1990 during solar maximum conditions and 1994-1995 during solar minimum conditions were analyzed to produce a range of α over maximum and minimum solar conditions. Pilinski et al. (2010) shows the variations in alpha related to altitude and solar minimum and maximum conditions for multiple satellites in Figure 12. The data used for Figure 12 was obtained from Bowman and Moe (2006), Pardini et al. (2010), Moe et al. (1995), Imbro et al. (1975), Ching et al. (1977), and Beletsky (1970). Most of the satellite data used for this graph was from spherical satellites and most values were obtained empirically.

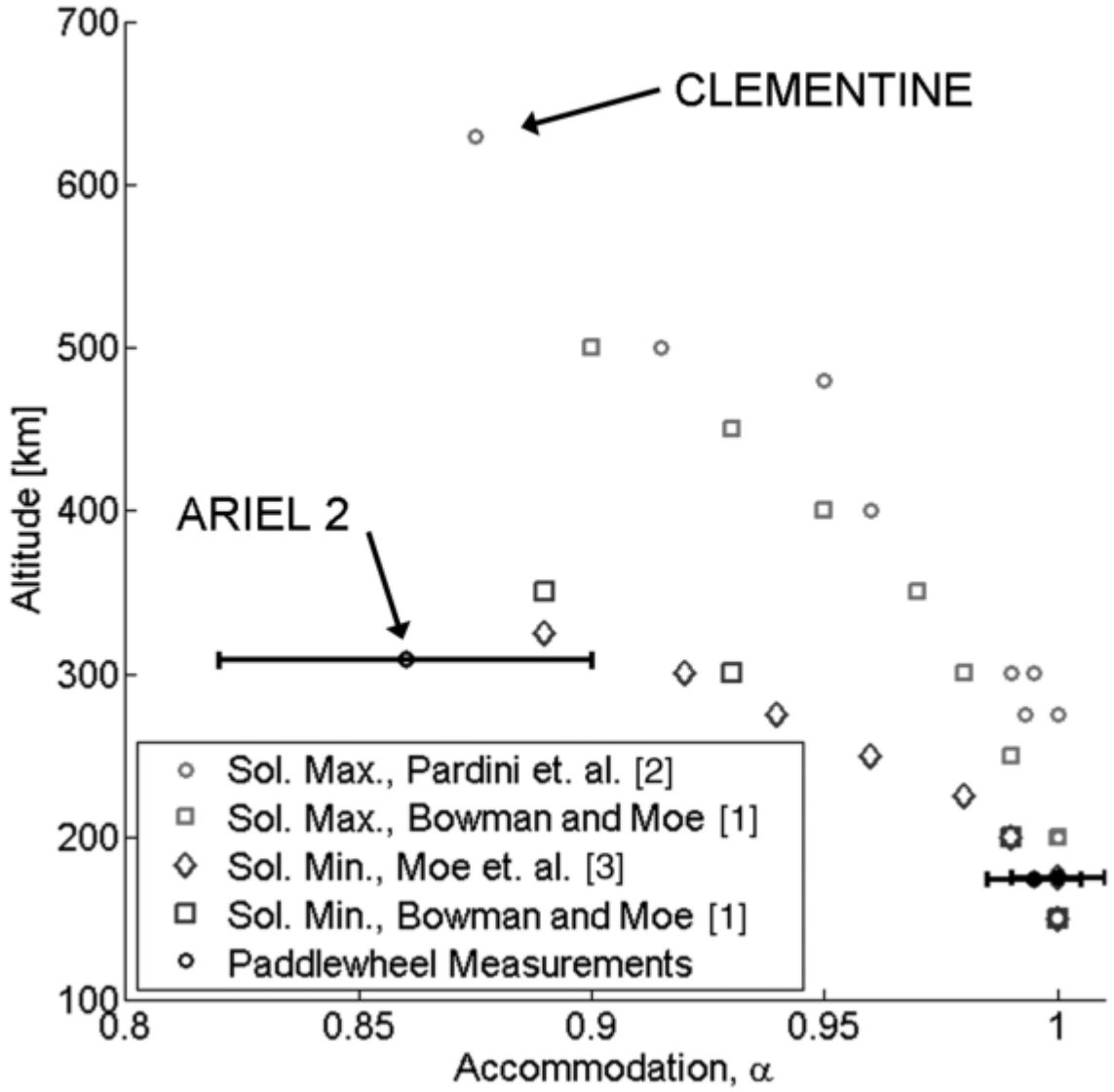

Figure 12: Estimate energy-accommodation coefficients for solar minimum and maximum conditions (Pilinksi et al., 2010)

Since the accommodation coefficient is dependent on the atmospheric conditions that the satellite is experiencing at its current altitude (namely the atmospheric temperature (T_i) and oxygen number density (n_o)), the altitude of the spacecraft is not a reliable variable for determining the satellite's current accommodation coefficient. In order to produce a more reliable way for determining the accommodation coefficient experienced by a satellite, Pilinski et al. (2010) relates the accommodation coefficient to the

product of the n_o and T_i experienced by the satellites analyzed by Bowman and Moe (2006). Pilisnki et al. (2010) do this by using the atmospheric model NRLMSISE 2000 to determine the average n_o and T_i experienced by each spherical satellite at the specific altitude for which their accommodation coefficient was calculated. Once the accommodation coefficients (38 data points total) were matched with their appropriate n_o and T_i product, they were fitted to an analytical model using a least-squares fit.

The analytical model chosen by Pilinksi et al. (2010) was the Langmuir isotherm, which for a certain constant temperature, relates the monolayer surface absorption fraction by a particular species (such as atomic oxygen) as a function of the partial pressure of that species (Adamson, 1990). Pilinski et al. (2010) chose this model because of its simplicity and because it had been used successfully to rectify atomic oxygen observations made by spaceborne pressure gauges (Moe and Moe, 1967). The Langmuir isotherm used by Pilinski et al. (2010) is shown in equation (16).

$$\alpha = \frac{K \cdot P}{1 + K \cdot P} \tag{16}$$

The variable K is a fitting parameter constant which Pilinski et al. (2010) set to 7.50 X 10^{-17}. This gave an average accommodation coefficient error of -0.9% and a standard deviation of ±1.7% between the accommodation coefficients determined from the analysis of the seven spherical satellites and the Langmuir isotherm. The variable P is the partial pressure component, which is the partial pressure divided by the Boltzmann's constant. Pilinski et al. (2010) set the variable P to equal the product of n_o and T_i in order to achieve the Langmuir isotherm shown in equation (17).

$$\alpha = \frac{7.50\ X\ 10^{-17} \cdot n_o \cdot T_i}{1 + 7.50\ X\ 10^{-17} \cdot n_o \cdot T_i} \tag{17}$$

Table 9 and Table 10 show the satellites that were analyzed by Bowman and Moe (2006) and the accommodation coefficients that were obtained from the analysis of them.

Table 9: Spherical Satellites used for determining the accommodation coefficients (Pilinski et. al., 2010) taken from Bowman and Moe (2006)

Type	Ref. no.	Obs. year	Alt. range, km	Inc.
Taifun-Yug	11796	1989	206–277	82.9
Taifun-Yug	13750	1989	232–377	65.8
Taifun-Yug	15446	1990	232–355	65.8
Calsphere	04958	1989	355–501	88.3
Taifun-Yug	21190	1995	205–302	65.8
ODERACS[a]	22990	1994	230–327	56.9
ODERACS[a]	22994	1994–1995	208–326	56.9

[a]ODERACS denotes Orbital Debris Radar Calibration Sphere.

Table 10: Accommodation coefficients used in Pilinski et al. (2010, 2011) computed by Bowman and Moe (2006)

Altitude, km	α solar max.	α solar min.
150	1.00	1.00
200	1.00	0.99
250	0.99	0.97
300	0.98	0.93
350	0.97	0.89
400	0.95	——
450	0.93	——
450	0.90	——

The results in Table 10 are a summation of the 38 data points (which were not given in Bowman and Moe (2006)) that Pilinksi et al. (2010) used to determine the accommodation coefficients for the seven spherical satellites. Pilinski et al. (2010) provided these 38 data points, which are shown in Table 11 and Table 12.

Table 11: Solar maximum values for $n_o \cdot T_i$ and α (Pilinski et al., 2010)

Obj.	Year	doy_o	doy_f	Alt.	$n_O \cdot T_i$	α
11796	89	22	24	272	1.86×10^{15}	0.985
11796	89	68	78	225	5.70×10^{15}	0.996
11796	89	165	171	198	7.60×10^{15}	1.000
13750	89	68	77	372	6.02×10^{14}	0.962
13750	89	151	155	347	5.93×10^{14}	0.971
13750	89	199	203	322	6.86×10^{14}	0.976
13750	89	232	236	296	1.27×10^{15}	0.981
13750	89	253	255	272	2.32×10^{15}	0.985
13750	89	263	266	234	3.71×10^{15}	0.994
13750	89	270	273	192	8.24×10^{15}	1.000
15446	89–-90	354	3	347	6.67×10^{14}	0.971
15446	90	31	35	322	7.52×10^{14}	0.976
15446	90	58	63	298	1.19×10^{15}	0.980
15446	90	81	84	271	2.06×10^{15}	0.985
15446	90	91	93	249	2.55×10^{15}	0.990
15446	90	99	102	218	4.32×10^{15}	0.997
4958	89	174	176	498	6.69×10^{13}	0.902
4958	89	227	229	448	1.96×10^{14}	0.931
4958	89	240	242	423	1.95×10^{14}	0.941
4958	89	248	250	395	4.07×10^{14}	0.952
4958	89	253	254	372	5.88×10^{14}	0.962
4958	89	257	258	346	7.56×10^{14}	0.971

Table 12: Solar minimum values for $n_o \cdot T_i$ and α (Pilinksi et al., 2010)

Obj.	Year	doy_o	doy_f	Alt.	$n_O \cdot T_i$	α
21190	94	339	342	298	2.89×10^{14}	0.931
21190	95	39	41	273	4.61×10^{14}	0.953
21190	95	69	71	249	8.84×10^{14}	0.971
21190	95	80	82	226	1.41×10^{15}	0.982
21190	95	88	89	198	2.92×10^{15}	0.991
22990	94	70	73	323	2.02×10^{14}	0.911
22990	94	145	148	298	2.35×10^{14}	0.932
22990	94	222	225	274	3.17×10^{14}	0.952
22990	94	245	248	249	6.12×10^{14}	0.971
22990	94	262	265	221	1.42×10^{15}	0.984
22994	94	106	108	323	2.41×10^{14}	0.911
22994	94	288	291	299	3.44×10^{14}	0.931
22994	94	352	355	273	4.39×10^{14}	0.953
22994	95	33	36	251	7.69×10^{14}	0.969
22994	95	48	50	225	1.36×10^{15}	0.982
22994	95	56	57	202	2.24×10^{15}	0.989

Pilinski et al. (2010) applied the Langmuir isotherm fit to the 38 data points shown in Table 11 and Table 12 to achieve the graph shown in Figure 13.

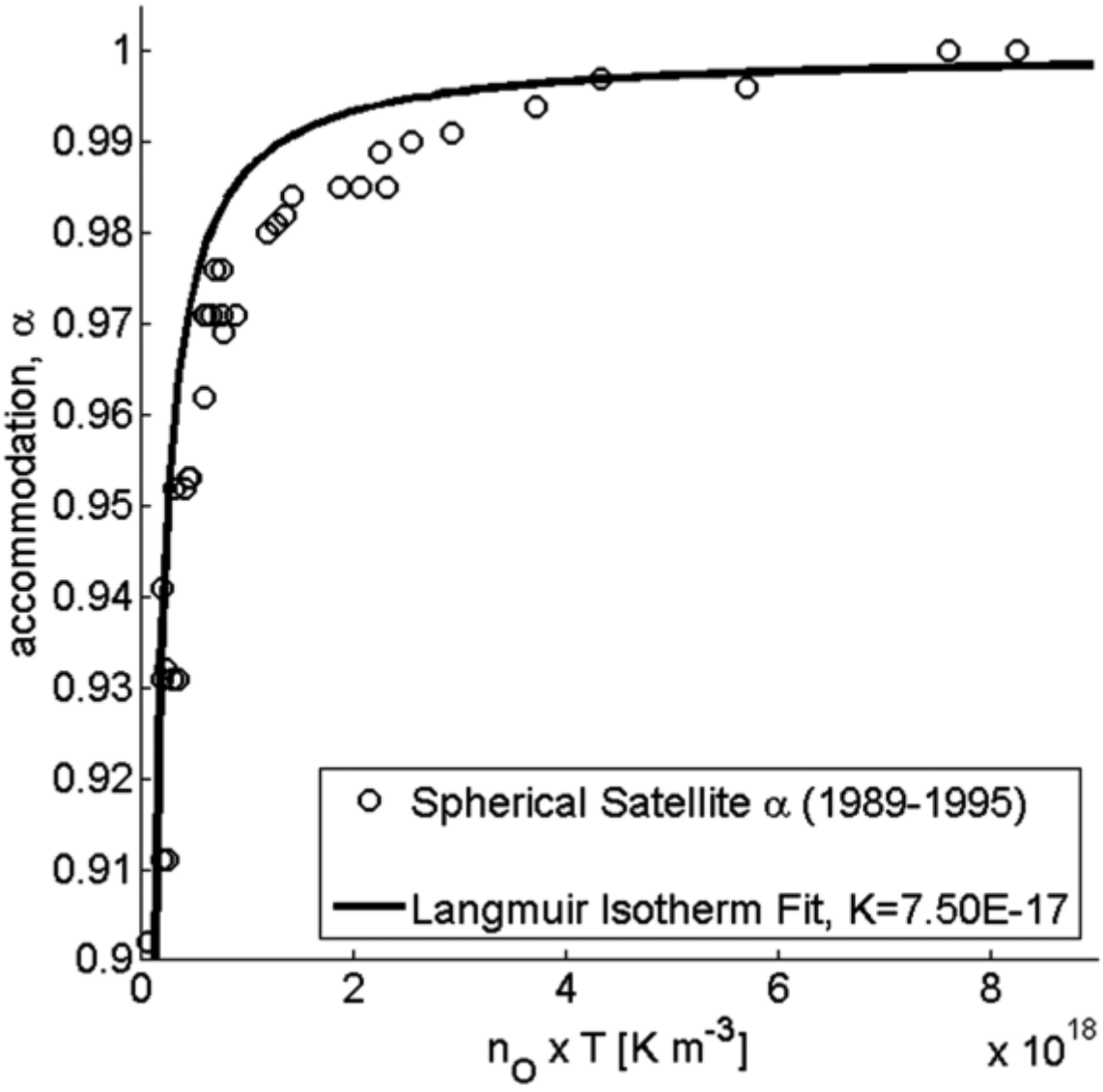

Figure 13: Accommodation coefficients as a function of $n_o \cdot T_i$ (Pilinski et al., 2010)

A nice approximate summation of the expected drag coefficients encountered by a variety of satellite shapes (including spherical) for three different accommodation coefficients is given in Moe et al. (1995) shown in Table 13, Table 14, and Table 15.

Table 13: C_D for α = 1.00 (Moe et al., 1995)

Temp.	M	Flat Plate	Cylinder + Flat Plates (L/D =1)		Cone θ = 30°	Cone θ = 60°	Sphere
500 K	18	2.131	2.332	2.187	2.069	2.114	2.094
500 K	22	2.117	2.300	2.169	2.062	2.103	2.084
1000 K	18	2.139	2.424	2.232	2.077	2.122	2.106
1000 K	22	2.124	2.382	2.208	2.069	2.109	2.094
1500 K	18	2.147	2.496	2.269	2.085	2.130	2.118
1500 K	22	2.131	2.447	2.241	2.075	2.116	2.103

Table 14: C_D for α = 0.95

Temp.	M	Flat Plate	Cylinder + Flat Plates (L/D = 1)		Cone θ = 30°	Cone θ = 60°	Sphere
500 K	18	2.353	2.555	2.362	2.180	2.307	2.242
500 K	22	2.347	2.530	2.349	2.177	2.302	2.237
1000 K	18	2.361	2.646	2.407	2.188	2.315	2.254
1000 K	22	2.354	2.612	2.388	2.184	2.308	2.247
1500 K	18	2.369	2.718	2.444	2.196	2.323	2.266
1500 K	22	2.361	2.677	2.421	2.190	2.315	2.257

TABLE 5. Drag Coefficients for the Case α = 0.90

Table 15: C_D for α = 0.90

Temp.	M	Flat Plate	Cylinder + Flat Plates (L/D = 1)		Cone θ = 30°	Cone θ = 60°	Sphere
500 K	18	2.480	2.682	2.462	2.244	2.417	2.327
500 K	22	2.476	2.658	2.450	2.241	2.413	2.323
1000 K	18	2.488	2.773	2.506	2.252	2.425	2.338
1000 K	22	2.482	2.740	2.489	2.248	2.420	2.332
1500 K	18	2.496	2.845	2.544	2.260	2.433	2.351
1500 K	22	2.489	2.805	2.522	2.254	2.426	2.342

The tables were generated using Sentman's (1961a) equations which assume complete diffuse angular distribution (DRIA) for the reemitted molecules (Moe et al. 1995). The values for the satellite incident velocity and surface temperature that were used for the C_D calculations were chosen to be 7600 m/s and

300 K. The variable (Temp.) in the above tables represents the atmospheric temperature for three different solar activity levels, and the variable (M) is the mean molecular mass.

An additional method for determining the accommodation coefficient is given in Walker et al. (2014), which also utilizes the Langmuir isotherm in the process of determining the accommodation coefficient. Walker et al. (2014) take a different approach to using the Langmuir isotherm than Pilinski et al. (2010); instead of using the Langmuir isotherm to calculate the accommodation coefficient from the partial pressure component (n_O T), Walker et al. (2014) use the Langmuir isotherm to calculate the fraction of the satellite's surface covered by atomic oxygen (θ). The equation for θ is shown in equation (18).

$$\theta = \frac{KP_O}{1 + KP_o} \tag{18}$$

K is the Langmuir adsorbate constant and P_O is the partial pressure of atomic oxygen. The variable θ can then be related to the total drag coefficient ($C_{D,T}$) of the satellite using equation (19).

$$C_{D,T} = (1 - \theta)C_{D,s} + \theta C_{D,ads} \tag{19}$$

The variables $C_{D,s}$ and $C_{D,ads}$ are the drag coefficients for a satellite with a clean surface and a surface completely covered by atomic oxygen. Both drag coefficients are calculated using the closed-form equations for Diffuse Reflection with Incomplete Accommodation (DRIA); these equations are discussed in section 2.8 of this document. The accommodation coefficient is set to 1 for $C_{D,ads}$ because the satellite is assumed completely covered in atomic oxygen, and the accommodation coefficient for $C_{D,s}$ is found by using the Goodman empirical model for the energy accommodation coefficient (Goodman and Wachmann, 1966) as shown in equation (20).

$$\alpha_s = \frac{2.4\mu}{(1 + \mu)^2} \tag{20}$$

μ is the ratio of the atomic mass of the atmosphere to the atomic mass of the satellite surface material. The equation for this ratio is shown in equation (29).

$$\mu = \frac{m_{atm}}{m_s} \tag{21}$$

Finally, in order to determine the correct Langmuir adsorbate constant, the equation for $C_{D,T}$ given in equation (19) is solved for θ producing equation (22).

$$\theta = \frac{C_{D,T} - C_{D,s}}{C_{D,ads} - C_{D,s}} \tag{22}$$

The equation is solved for θ by using fitted drag coefficients determined by Pardini et al. (2010) shown in Table 16.

Table 16: Fitted drag coefficients for spherical satellites at different altitudes (Pardini et al., 2010)

Satellite [catalog number]	Altitude	Fitted C_D
Cosmos 1427 [13750], Cosmos 1615 [15446]	200	2.08
Cosmos 1427 [13750], Cosmos 1615 [15446]	300	2.13
Calsphere 3 [4957], Calsphere 4 [4958], Calsphere 5 [4963]	300	2.16
Cosmos 1427 [13750], Cosmos 1615 [15446], Calsphere 3 [4957], Calsphere 4 [4958], Calsphere 5 [4963]	400	2.24
Calsphere 3 [4957], Calsphere 4 [4958], Calsphere 5 [4963]	500	2.31

Walker et al. (2014) propagated each satellite through the NRLMSISE 2000 atmospheric model with the SGP4 propagator based on two-line elements, and averaged the θ from equations (18, 22) when the altitude was within 25 km of the fitted drag coefficient. This was done by Walker et al. (2014) for three different GSI models: Maxwell's model, DRIA model, and the CLL model. The best-fit results for K that Walker et al. (2014) obtained through a least squares analysis are given in Table 17. The two Langmuir isotherms chosen for the DRIA and CLL GSI models are shown in Figure 14.

Table 17: Best-fit Langmuir adsorbate constants for three GSI models (Walker et al., 2014)

Gas–surface interaction model	Best-fit K
Diffuse reflection with incomplete accommodation	1.44E + 06
Maxwell's model	1.40E + 03
CLL model	2.89E + 06

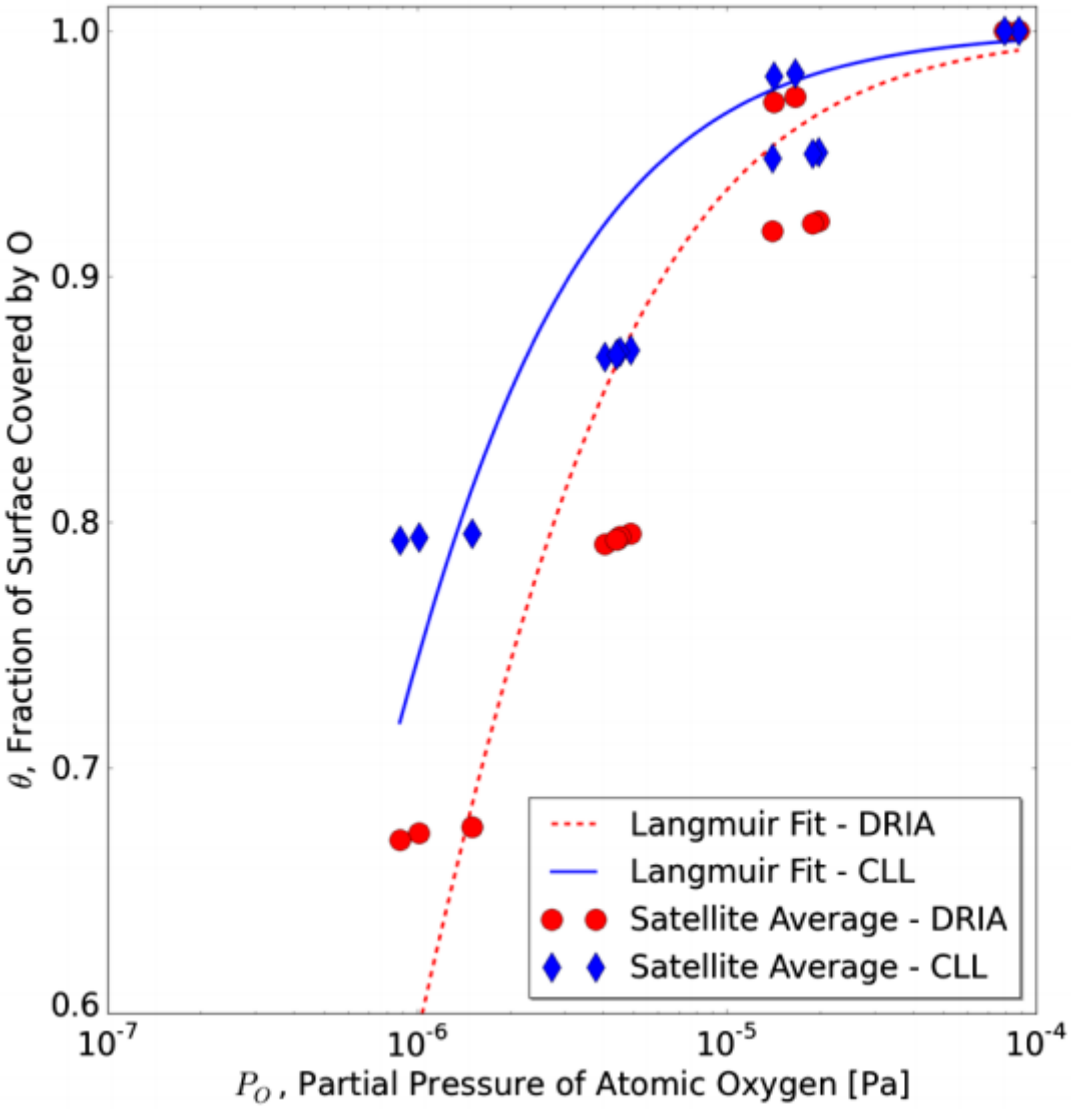

Figure 14: Langmuir isotherms for DRIA and CLL GSI models (Walker et al. 2014)

1.8.6. **Expected Results for ANDE-2's Drag Coefficient Range from Previous Research**

Since ANDE-2 operated throughout its lifespan during solar minimum conditions, the expected range of α should be approximately what Bowman and Moe (2006) and Pilinski et al. (2010) determined for solar minimum conditions. Therefore, the initial value for the accommodation coefficient for ANDE-2 at the beginning of its mission should be around 0.89-0.9, and near 1 during the end of its mission. Since the variation of α using the CLL model produces the greatest effect on the C_D of satellites, the highest possible value for the C_D of ANDE-2 according to Figure 11 would be around 2.6 for an α = 0.89-0.90 using the CLL model and 2.35 using the DRIA model/closed-form solution.

The last SLR readings for the ANDE-2 Caster satellite occurred on August 7, 2010 and March 27, 2010 for the ANDE-2 Pollux satellite putting the satellites at an altitude of around 220 km (Castor) and 200 km (Pollux). The relative velocities of the satellites would most likely have been around 7.2 km/s using equation (2) and α would have been close to 1 according to Table 10. Using Figure 10, which should give the smallest approximate value for C_D since it sets α = 1, gives a C_D for a spherical satellite traveling at 7.2 km/s to be approximately 2.125 (for the CLL and DRIA models). For the solution given by Moe et al. (1995), the lowest possible value for the C_D of a spherical satellite at α = 1 is given in Table 13 (Temp. = 500 K, M = 22) as approximately 2.08. The results for the expected approximate highest and lowest values of C_D that ANDE-2 will be expected to have during its mission lifetime are summarized in Table 18.

Table 18: Approximate Highest and Lowest values of C_D for ANDE-2

	CLL	**DRIA/Closed-Form**
Approximate Highest Expected value for C_D	2.60	2.35
Approximate Lowest Expected value for C_D	2.125	2.08

2. Methodology

This section deals with the process that the ODTK program uses to estimate the atmospheric densities experienced by the ANDE-2 satellites using SLR measurements and the method used in this thesis for determining the theoretical drag coefficients of the ANDE-2 satellites using the available SLR measurements. The ODTK scenario templates that were used in this research came from previous research performed by Lechtenberg (2015). These templates included optimal density and ballistic coefficient half-lives of 180 minutes and 1.8 minutes that were found in the research of Lechtenberg (2010). Since the research in this document involves determining the C_D of the ANDE-2 satellites using GSI models, the ballistic coefficient half-life found by Lechtenberg (2010) will not be used for the majority of this research as the *BC* will be estimated using physics-based equations and held constant for each specific day. Variations in the ballistic coefficient half-life will be examined in section 3.7.

The atmospheric density model that was used in the GSI calculations for this document was the NRLMSISE 2000 model, as it was easily accessible and available via MATLAB's Aerospace Toolbox under the function name *atmosnrlmise00*. This was used in conjunction with solar and magnetic indices that were obtained from Natural Resources Canada (2015) and the National Geophysical Data Center (2015b). The NRLMSISE 2000 model was also used since it was the most comprehensive model in the MATLAB Aerospace Toolbox and calculates atmospheric constituent number densities.

2.1. Satellite Laser Ranging (SLR)

In order to perform calculations in ODTK and make GSI drag coefficient predictions for the ANDE-2 satellites, position data for the ANDE-2 satellites is needed. These data come in the form of satellite laser ranging data which is distributed by the International Laser Ranging Service (ILRS) and is available on the ILRS website (Pearlman et al., 2002). The ILRS distributes several different types of SLR data for the ANDE-2 satellites, which come in either a Consolidated Range Data (CRD) format or a Consolidated Prediction Format (CPF). For this research, CPF laser ranging data (which comes in the form

of a .nrl file) will be used for calculations because it provides daily minute-by-minute updates of satellite position coordinates. The coordinates come in Cartesian form relative to the International Terrestrial Reference System (ITRF) reference frame (Pearlman et al., 2002), which is also commonly called the Earth Centered Earth Fixed (ECEF) reference frame (Vallado, 2007).

2.2. Precision Orbit Ephemerides

The Challenging Minisatellite Payload (CHAMP) and Gravity Recovery and Climate Experiment (GRACE) satellites were both utilized in the development of Precision Orbit Ephemeris (POE) derived density data. POE data are used in the ODTK's optimal orbit determination process to estimate the atmospheric density conditions experienced by a satellite. POE data are available from the Helmholtz Centre Potsdam website page at http://isdc.gfz-potsdam.de/. The data are available in the form of Precision Science Orbits (PSO) and Rapid Science Orbits (RSO).

2.3. Optimal Orbit Determination

Orbit determination is the process of estimating the orbit of a satellite as it is influenced by the gravitational fields of other bodies. A classic orbit determination problem involves the assumption that a satellite orbits a central point mass which influences the satellite solely with its gravitational field. The satellite parameters needed in order to predict its orbit around the central mass are at the very least the position and velocity vector, which can be broken into six Keplerian elements. These Keplerian elements are: (1) a, semi major axis (2) e, eccentricity (3) i_{inc}, inclination (4) Ω, right ascension of the ascending node (5) ω_p, argument of periapsis (6) tp or T_a, the time of perifocus or the true anomaly (Tapley et al., 2004). The initial time is denoted as t_0 and the initial state vector which contains the satellite's trajectory information is $\boldsymbol{X}_0$. The initial state vector is then integrated through equations of motion to a future time t in order to determine the future state vector $\boldsymbol{X}(t)$. The initial state variables are not precisely known since the observational data usually comes in the form of range, range-rate, azimuth, elevation, and other

observable quantities from ground tracking stations. This is because the observed measurements are often related by some nonlinear function of the state variables. (Tapley et al., 2004)

If the previous method of a simplistic two-body orbit determination method is used for the estimation of a satellite's trajectory, large errors in the estimation of the trajectory will quickly make it difficult to predict with any accuracy the future position of the satellite. This is especially true for artificial satellites in LEO (such as the ANDE-2 satellites) that experience a variety of other influences that directly affect their trajectory such as the oblateness of Earth, Earth albedo, solar radiation pressure, and atmospheric drag. Artificial satellites are also subject to increased sensitivity to some of these influences due to the satellite's relatively low mass density in comparison to naturally occurring satellites. (Tapley et al., 2004)

The ANDE-2 satellites require a more comprehensive model that takes into account the different influences that affect the motion of the satellites as they orbit the Earth. The ODTK program uses a more advanced and comprehensive optimal orbit determination algorithm that takes into account different influential forces that affect the satellite's flight path. This includes the atmospheric density, which ODTK estimates using its optimal orbit determination algorithm in unison with the previously mentioned atmospheric models in sections 1.6.1 to 1.6.4. Additionally, the ODTK program has the ability to use a least squares batch processor to refine the initial state vector, or it can use a filter/smoother scheme that will constantly refine the current state vector (Analytical Graphics, Inc.). A filter/smoother algorithm was used to process the ANDE-2 SLR data to produce the estimated atmospheric data.

A more complete description of what criteria need to be met in order for an orbit determination method to be deemed optimal is given in the ODTK "Theory and Algorithms" document (Wright, 2013, p. 16-17), which is given verbatim in the italicized text below.

1. *"Sequential processing (SP) is used to account for force modeling errors and measurement information in the time order in which they are realized.*

2. *Sherman's Theorem is applied (Sherman, 1955), (Sherman, 1958), (Meditch, 1969), (Kalman, 1963). To summarize, the optimal state estimate correction matrix $\Delta\hat{X}$ is the expectation of the state error matrix ΔX given the measurement residual matrix Δy.* That is: $\Delta\hat{X} = E\{\Delta X|\Delta y\}$.
3. *Linearization of state-estimate time transition and state-to-measurement representations are local in time, not global.*
4. *The state estimate structure is complete.*
5. *All state-estimate models and state-estimate-error model approximations are derived from appropriate physics of sensors and force modeling.*
6. *All measurement models and measurement-error model approximations are derived from appropriate sensor hardware definitions and associated physics, and measurement sensor performance.*
7. *Necessary conditions for real data include:*
    - *Measurement residuals approximate Gaussian white noise (Meditch, 1969), (Anderson and Moore, 1979).*
    - *McReynolds' filter-smoother consistency test is satisfied.*
8. *For simulated data: The state-estimate errors agree with the state-estimate error covariance function.*

The first six conditions define standards for optimal algorithm design and for the establishment of a realistic state-estimate error covariance function. The last two conditions enable validation: they define realizable test criteria for optimality.

2.4. Gauss-Markov Processes

Dynamic models often have issues with unmodeled and unexpected forces that act upon a spacecraft during orbit and give rise to inconsistencies in orbit determination problems. In order to

compensate for these unmodeled forces, a first-order Guass-Markov process is used. The Gauss-Markov process uses a Gaussian distribution and utilizes the Markov property. The Markov property simply states the probability density function should be dependent on the previous observation directly before the current observation. More information on this process is detailed in Tapley et al. (2004).

2.5. Gauss-Markov Half-Lives

The Gauss-Markov half-lives are user defined values that are associated with estimated quantities that are part of the Gauss-Markov processes. These estimated quantities exist in the state vector. The two estimated quantities with associated Gauss-Markov processes used in this research are the atmospheric density ratio ($\Delta\rho/\rho$) and the ballistic coefficient ratio ($\Delta BC/BC$). The ratios are a comparison of the density or ballistic coefficient corrections to the baseline atmospheric model or baseline ballistic coefficient values. The half-lives determine how long a previously estimated ratio affects the current estimated ratio. The half-life values for both the atmospheric density and ballistic coefficient can have their own specific half-life. (Analytical Graphics, Inc).

The technique for which these half-lives are implemented in the Gauss-Markov process is detailed in the ODTK help file (Analytical Graphics, Inc.). The help file illustrates the process by selecting a random scalar variable $x = x(t_k)$, which is either the density or ballistic coefficient, that satisfies equation (23).

$$x(t_{k+1}) = \Phi(t_{k+1}, t_k)x(t_k) + \sqrt{1 - \Phi^2(t_{k+1}, t_k)}w(t_k), \quad k \in \{1, 2, \ldots\} \tag{23}$$

The variable $w(t_k)$ is a random Gaussian white noise variable with a zero mean and a standard deviation that does not change. The transfer function equation for the variable Φ is given in equation (24).

$$\Phi(t_{k+1}, t_k) = e^{\alpha_m |t_{k+1} - t_k|} \tag{24}$$

The equation for the variable α_m is shown in equation (25).

$$\alpha_m = \frac{\ln(0.5)}{\tau} \tag{25}$$

The variable τ is the period defined by the user for the atmospheric density or ballistic coefficient half-life. (Analytical Graphics, Inc. and Vallado et al., 2010).

2.6. Sequential Filter Description

The SLR data for the ANDE-2 satellites are given on a per-minute basis, and thus provide the ability to update previous calculations with each new satellite position data point. The chosen method for analyzing these data is a sequential filtering algorithm that processes data as soon as it is received. The original sequential filtering algorithm was developed by Swerling (1959), but a more recent variation of the sequential filter been associated with the work done by Kalman (1960). And as a result of this association, the sequential filter is often referred to as the *Kalman filter*.

The sequential filter processes the SLR data for the ANDE-2 satellites and estimates a variety of state variables such as the spacecraft position vector, velocity vector, corrections to the atmospheric density and ballistic coefficient, as well as other parameters relevant to the simulation process. The algorithm for the sequential filter is described in Tapley et al. (2004).

Once the filtering process is complete, a smoother process is applied so that all the data will affect the entirety of the filter's calculations. The smoother takes the final output from the filter and processes the data backwards to the filter's initial state. More information on the sequential filter and smoother can be found in Tapley et al. (2004), and in the references suggested by Tapley et al. (2004), which are Sorenson (1985), Bierman (1977), Liebelt (1967), Tapley (1973), Gelb (1974), Maybeck (1979), Grewal and Andrews (1993), and Montenbruck and Gill (2001).

2.7. McReynolds Consistency Test for Filter/Smoother

The McReynolds filter/smoother consistency test is performed in the ODTK program in order test the validity of the force models. This test simply compares the difference between the filtered state (X_f) and the smoother state (X_s) over the square root of the difference between the covariance for the filter (σ^2_f) and smoother (σ^2_s). If the filter/smoother consistency stays within a value of 3, consistency is claimed. The McReynolds consistency inequality is shown in equation (26). (Vallado et al., 2010)

$$consistency = \left| \frac{X_f - X_s}{\sqrt{\sigma_f^2 - \sigma_s^2}} \right| \leq 3 \tag{26}$$

2.8. Cross-Correlation

Cross Correlation (*CC*) is a method by which two quantities that vary over time are compared to see the amount of correlation that exists between them. A perfect correlation between two quantities would be equal to 1, and a perfect inverse correlation between two quantities would be equal to -1. The equation for the cross correlation is given in equation (27).

$$CC(d) = \frac{\sum[(x_i - mx)(y_{i-d} - my)]}{\sqrt{\sum(x_i - mx)^2}\sqrt{\sum(y_{i-d} - my)^2}} \tag{27}$$

The variables *x* and *y* are the data arrays with *mx* and *my* being the average of those arrays where *i*=0, 1, 2, 3, …, *N*-1 (*N* is equal to the number of elements in the array). The variable *d* is the delay which can be defined as *d*=0, 1, 2, 3, …, N-1. (Bourke, 1996). The *CC* method will be used in this document to determine the zero-lag (*d*=0) cross correlation between the ODTK estimated ballistic coefficient and the atmospheric density difference. The atmospheric density difference is between the estimated and non-estimated (fixed) ballistic coefficient calculated atmospheric densities.

2.9. Density Dependence Analysis

The density dependence for different baseline atmospheric models was performed for days, weeks, months, solar activity, and geomagnetic activity. The analysis was performed by examining the density correction factor (*DCF*) and the unbiased standard deviation (*UBSTD*) for each atmospheric model in relation to the desired parameter of interest (date or solar/geomagnetic activity). The equations for the *DCF* and *UBSTD* are shown in equations (28-29).

$$DCF = \frac{\bar{\rho}_{Estimated}}{\bar{\rho}_{Model}} \tag{28}$$

$$UBSTD = \sqrt{\frac{1}{N-1}\sum_{i=1}^{N}(\rho_{Estimated} - DCF * \rho_{Model})^2} \tag{29}$$

$\rho_{Estimted}$ and ρ_{Model} are the estimated and model densities generated using the ODTK program. *N* is the number of data points chosen.

2.10. Physical Drag Coefficient

A physical drag coefficient is calculated by measuring the exchange of momentum and energy between the satellite and atmospheric molecules. The physical drag coefficient was set as a constant when implemented in the optimal orbit determination process for the desired period of interest (one day). The reason for using a physical drag coefficient over a fitted drag coefficient is due to the fact that fitted drag coefficient may be less accurate due to modeling errors. This is because the fitted drag coefficient absorbs errors from the optimal orbit determination process, especially errors from the atmospheric models being used in the calculations. Determining the coefficient of drag through the use of equations based on physics independently from orbit determination modeling parameters eliminates the possibility of error pollution from those specific parameters. However, the physical drag coefficient contains the errors inherent within the chosen drag coefficient theory.

2.10.1. **Closed-Form Equations for Gas-Surface Interaction**

The relative amount of kinetic energy lost by the molecule reflected from the satellite's surface is quantified as a fraction known as the accommodation coefficient (α). The accommodation coefficient compares the difference between the temperature of the incoming molecule ($T_{k,i}$) and reflected molecule ($T_{k,r}$) to the difference between the temperature of the incoming molecule and the satellite surface temperature (T_w). The accommodation coefficient can be determined by using equation (30), which was defined by Knudsen (1934).

$$\alpha = \frac{T_{k,i} - T_{k,r}}{T_{k,i} - T_w} \tag{30}$$

The difference between this equation and equation (6) is how the ratio of α is defined. The ratios can be related using the internal energy relation $E = C_v T$, where C_v is the streaming heat capacity of a gas molecule (Goodman, 1980). The kinetic incident and reflected temperatures must be calculated for monatomic particles only (such as atomic oxygen) and can be calculated using equations (31-32).

$$T_{k,i} = \frac{m_g \, v_{rel}}{3k_B} \tag{31}$$

$$T_{k,r} = T_{k,i}(1-\alpha) + \alpha T_w \tag{32}$$

The variable m_g is the mean molecular mass of the atmosphere, k_B is the Boltzmann constant and the variable v_{rel} is the relative velocity of the molecule in relation to the satellite, which was calculated using equation (2).

Equations (33-35) are closed-form DRIA solutions for calculating the coefficient of drag for three different basic satellite shapes: a flat plate, a sphere, and a cylindrical satellite. The axis of the spacecraft is assumed to be aligned with its velocity vector for these equations (Sentmann 1961b and Pilinski et al. 2010). For the purpose of this document, only equation (34) will be used since it is relevant to the spherical nature of the ANDE-2 satellites.

$$C_{d,fp} = \left(2 + \frac{1}{s^2}\right)\mathrm{erf}(s) + \frac{2}{\sqrt{\pi}s}e^{-s^2} + \frac{\sqrt{\pi}}{s}\sqrt{\frac{T_{k,r}}{T_\infty}} \tag{33}$$

$$C_{d,sp} = \left(\frac{4s^4 + 4s^2 - 1}{2s^4}\right)\mathrm{erf}(s) + \frac{2s^2 + 1}{\sqrt{\pi}s^3}e^{-s^2} + \frac{2\sqrt{\pi}}{3s}\sqrt{\frac{T_{k,r}}{T_\infty}} \tag{34}$$

$$C_{d,cy} = \left(2 + \frac{1}{s^2}\right)\mathrm{erf}(s) + \frac{2}{\sqrt{\pi}s}e^{-s^2} + \frac{\sqrt{\pi}}{s}\sqrt{\frac{T_{k,r}}{T_\infty}} + \frac{4}{\sqrt{\pi}s}\frac{L}{D} \tag{35}$$

The variable (s) is the speed ratio of the relative velocity of the satellite (v_{rel}) to the most probable speed of the incident particles (v_{mp}) and the function *erf* is the Gauss error function. T_∞ is the atmospheric temperature at the satellite's position and m_g is the mean molecular mass, which were both calculated using the MATLAB function *atmosnrlmsise00* (refer to section 2.10.2). Equations (36-38) define the solutions for the variables s, v_{mp} and *erf* (Pilinksi et al. 2010).

$$s = \frac{v_{rel}}{v_{mp}} \tag{36}$$

$$v_{mp} = \sqrt{\frac{2k_b T_\infty}{m_g}} \tag{37}$$

$$\text{erf}(s) = \frac{2}{\sqrt{\pi}} \int_0^s e^{-t^2} dt \tag{38}$$

2.10.2. **Baseline Atmospheric Model**

The baseline density model used in unison with the closed-form gas surface interaction equations was the NRLMSISE 2000 atmospheric model via the *atmosnrlmsise00* MATLAB function. A detailed explanation of the *atmosnrlmsise00* function can be found in the MATLAB help file in the aerospace toolbox section (MATLAB, 2014). The *atmosnrlmsise00* function requires nine inputs in order to determine the atmospheric composition and temperature at a given location and altitude. The nine input requirements for the *atmosnrlmsise00* function are given below in the same order in which they are implemented in the function (MATLAB, 2014). The variable *m* stands for the number of days being analyzed. Because each day is analyzed individually in the program used to determine the satellite drag coefficient, the variable *m* is 1.

Inputs

1. *Altitude in meters: m-by-1 array*
2. *Geodetic latitude in degrees: m-by-1 array with angles between -180 and 180 degrees.*
3. *Longitude in degrees: m-by-1 array with angles between -180 and 180 degrees.*
4. *Year: m-by-1 array using date format yyyy. Example: 1999 or 2009.*
5. *Day of Year: m-by-1 array using numbers 1-365 for a non-leap year, and numbers 1-366 for leap year. m-by-1 array. Example: Feb. 7, 2009 = 38.*

6. *Universal Time (UT) in seconds: m-by-1 array using numbers 0-86400.*
7. *$F_{10.7}$ Average: m-by-1 array with 81 day average centered on day of year.*
8. *$F_{10.7}$ Daily: m-by-1 array with observed $F_{10.7}$ flux for the previous day.*
9. *Magnetic Index: use an m-by-7 array containing the magnetic index information.*
    a. *Daily magnetic index (AP).*
    b. *3 hour ap for current time.*
    c. *3 hour ap for 3 hours before current time.*
    d. *3 hour ap for 6 hours before current time.*
    e. *3 hour ap for 9 hours before current time.*
    f. *Average of eight 3 hour ap indices from 12 to 33 hours before current time.*
    g. *Average of eight 3 hour ap indices from 36 to 57 hours before current time.*

The two output parameters given by the *atmosnrlmsise00* function are shown below in the same order in which they are output by the function (MATLAB, 2014).

Outputs

1. *Temperature: an m-by-2 array containing temperature information in Kelvin.*
    a. *Exospheric temperature.*
    b. *Temperature at altitude.*
2. *Density: an m-by-9 array of densities.*
    a. *Number density of helium (ρ_{He}), in $1/m^3$.*
    b. *Number density of atomic oxygen (ρ_O), in $1/m^3$.*
    c. *Number density of nitrogen (ρ_{N2}), in $1/m^3$.*
    d. *Number density of oxygen (ρ_{O2}), in $1/m^3$.*
    e. *Number density of argon (ρ_{Ar}), in $1/m^3$.*
    f. *Total mass density, in kg/m^3.*

g. *Number density of hydrogen (ρ_H), in 1/m^3.*

h. *Number density of atomic nitrogen (ρ_N), in 1/m^3.*

i. *Anomalous oxygen number density, in 1/m^3.*

The mean molecular mass used in equations (31, 37) was calculated using equations (39-40).

$$\rho_{Total} = \rho_{He} + \rho_O + \rho_{N2} + \rho_{O2} + \rho_{Ar} + \rho_H + \rho_N \tag{39}$$

$$m_g = (\rho_{he} * H_e + \rho_O * O + \rho_{N2} * N_2 + \rho_{O2} * O_2 + \rho_{Ar} * A_r + \rho_H * H + \rho_N * N) * \left(\frac{AMU_{mass}}{\rho_{Total}}\right) \tag{40}$$

The variables used in equations (39-40) are as listed:

H_e is the atomic mass of helium in Atomic Mass Units (AMU). $H_e = 4.003\ AMU$.

O is the atomic mass of atomic oxygen. $O = 15.999\ AMU$.

N_2 is the atomic mass of nitrogen. $N_2 = 28.014\ AMU$.

O_2 is the atomic mass of oxygen. $O_2 = 31.998\ AMU$.

A_r is the atomic mass of argon. $A_r = 39.948\ AMU$.

H is the atomic mass of hydrogen. $H = 1.008\ AMU$.

N is the atomic mass of atomic nitrogen. $N = 14.007\ AMU$.

AMU_{mass} is the conversion from *AMU* to *kg*. $AMU_{mass} = 1.66053886\ X\ 10^{-27}\ \frac{kg}{AMU}$

2.10.3. **Latitude and Longitude Calculations**

The coordinates for the ANDE-2 satellites come in ECEF Cartesian form coordinates, and as a result, must be converted into geodetic latitude and longitude coordinates in order to be input into the *atmosnrlmsise00* function. The algorithm used for this conversion comes from Vallado (2007) and is shown in the italicized text below.

Given the position vector: $r_{ECEF_{sat}} = r_i + r_j + r_k$

$$r_{\delta sat} = \sqrt{r_i^2 + r_j^2}$$

$$\sin(\alpha_l) = \frac{r_j}{r_{\delta sat}} \qquad \cos(\alpha_l) = \frac{r_i}{r_{\delta sat}}$$

Perform a quadrant check for α_l. Once the correct α_l is determined, longitude=α_l.

$$\tan(\delta) = \frac{r_k}{r_{\delta sat}}$$

Let $\phi_{gd} = \delta$

LOOP

$$C_{\oplus} = \frac{R_{\oplus}}{\sqrt{1 - e_{\oplus}^2 \sin^2(\phi_{gd})}}$$

$$\tan(\phi_{gd}) = \frac{r_k + C_{\oplus} e_{\oplus}^2 \sin(\phi_{gd})}{r_{\delta}}$$

UNTIL $\phi_{gd} - \phi_{gd_{old}} < Tolerance = 0.001$

2.10.4. **Temperature Variation for Satellite Surface**

The expected maximum (T_{MAX}) and minimum (T_{MIN}) satellite surface temperatures were calculated using the thermal equations for the surface of a spherical satellite from Brown (2002). The equations assume a worst-case hot-temperature scenario and a worst-case cold-temperature scenario for the satellite at some specific altitude (*H*). Since the ANDE-2 satellites are constructed out of aluminum, the solar absorptivity (α_s) and inferred (IR) emissivity (ε_{IR}) properties were taken to be of polished aluminum. However, the ANDE-2 satellites' surfaces were not only painted aluminum, but were partially covered in retro-reflectors. The reason for using the thermal properties of polished aluminum was partially for the simplification of calculations, but also due to the lack of information regarding the thermal properties of the other materials and percentage of surface coverage by those materials. The values used for the polished

aluminum thermal properties were taken from table 7.2 from Brown (2002, p. 386). The equations for the surface temperature of a spherical satellite are shown in equations (41-44

$$K_a = 0.657 + 0.54\left(\frac{R_E}{R_E + H}\right) - 0.196\left(\frac{R_E}{R_E + H}\right)^2 \tag{41}$$

$$F_{S-e} = 0.5\left[1 - \frac{(H^2 + 2HR_E)^{0.5}}{H + R_E}\right] \tag{42}$$

$$T_{MAX-S} = \left[\frac{\left(\frac{G_s\alpha_s}{4} + q_{IR}\varepsilon_{IR}F_{S-e} + G_s a_b \alpha_s K_a F_{S-e} + \frac{Q_W}{\pi D^2}\right)}{\sigma\varepsilon_{IR}}\right]^{\frac{1}{4}} \tag{43}$$

$$T_{MIN-S} = \left[\frac{\left(q_{IR}\varepsilon_{IR}F_{S-e} + \frac{Q_W}{\pi D^2}\right)}{\sigma\varepsilon_{IR}}\right]^{\frac{1}{4}} \tag{44}$$

The variables used in the calculations are as follows:

K_a is the reflection of collimated incoming solar energy off of a spherical Earth factor.

$F_{s\text{-}e}$ is the view factor from a sphere to Earth.

R_E is the radius of the Earth. R_E = 6378.137 km

G_s is the solar constant. Gs = 1371 ± 5W/m^2

q_{IR} is the Earth IR emission. q_{IR} = 237 ± 21W/m^2

a_b is the albedo. a = 0.3 ± 0.05

σ Stefan-Boltzmann Constant. σ = 5.67 X 10^{-8} W/(m^2-K^4)

H is the altitude of the spacecraft. $H \approx$ 200-350 km

Q_W is the electrical power dissipation. Q_W is assumed to be 0 W.

D is the diameter of the spacecraft. D = 0.2412 m.

The average maximum and minimum temperature were calculated using equations (41-44) for the ANDE-2 satellites over an altitude of 200-350 km and were found to be approximately 484.5 K and 192 K.

2.10.5. **Accommodation Coefficient**

Three methods for determining the accommodation coefficient are utilized in this research for use in the closed-form GSI equations. The three methods for the determining the accommodation coefficients that ANDE-2 experienced while in orbit are given below:

1. The accommodation coefficient was determined by using a cubic spline interpolation method to interpolate the data obtained by Bowman and Moe (2006) (shown in Figure 12) over variations in altitude. The accommodation coefficient for the satellite was updated with each satellite position update relative to the satellite altitude. This provides an altitude data fit method for determining the accommodation coefficient that will subsequently not be as affected by variations in solar and geomagnetic activity as were the following methods. It will also provide an approximate answer from empirical data. Since the ANDE-2 satellites were only active during solar minimum, the accommodation coefficients used were from column two of Figure 12.

2. The accommodation coefficient was determined using the method described in Pilinski et al. (2010) which matches the Langmuir isotherm to 38 previously determined accommodation coefficients obtained by Bowman and Moe (2006) for spherical satellites in LEO. At each satellite position update, the partial pressure component ($P=n_o\ T_i$) was calculated for the corresponding altitude that the satellite was at and was used to calculate the accommodation coefficient. According to Pilinski et al. (2010), due to the lack of

empirically determined accommodation coefficients for spherical satellites, any accommodation coefficient that is below 0.85 should not be used for modeling satellite drag.

3. The accommodation coefficient was determined using the method developed by Walker et al. (2014) where the surface coverage fraction of atomic oxygen (θ) is calculated using the Langmuir isotherm equation and fitting constant K determined by Walker et al. (2014) for the DRIA method. The partial pressure of atomic oxygen (P_O) was calculated using the ideal gas law since the density of atomic oxygen (ρ_o) and the atmospheric temperature (T_∞) can both be determined from the NRLMSISE 2000 atmospheric model. The equation for the ideal gas law is shown in equation (3) and the alternate version solved for P_O is shown in equation (45).

$$P_o = \frac{n_o R T_\infty}{V} \tag{45}$$

R is the universal gas constant, 8.314 J/Mol*K, and V is the volume (given as 1 m^3 by *atmosnrlmsise00* for each density). The variable n_o is the number of moles of atomic oxygen which can be obtained by dividing the density of atomic oxygen (ρ_o) given by *atmosnrlmisis00* by Avogadro's number which is approximately $6.0221X10^{23}$ 1/moles.

3. Results

3.1. Preliminary Results

Several days were analyzed using the ODTK program and the original ballistic coefficient as determined by Lechtenberg (2015). Two different scenarios were run for each day: (1) the ballistic coefficient was estimated using the ballistic coefficient half-life of 1.8 minutes (2) the ballistic coefficient was held constant for each day. The atmospheric densities determined for each day and each model were subtracted to obtain the difference between the two ballistic coefficient scenarios. The zero-time offset cross correlation between the density difference and estimated ballistic coefficient was calculated to see the level of correlation between the results. The results are shown in Table 19.

Table 19: Cross correlation between estimated BC and atm. difference

Cross Correlation Numbers				
Dates	**CIRA 1972**	**Jacchia 1971**	**Jac-Bow 2008**	**NRLMSISE 2000**
17-Aug-09	-0.7122	-0.7112	-0.6148	-0.7158
13-Sep-09	-0.6759	-0.2657	-0.6725	-0.6847
6-Oct-09	-0.7886	-0.7893	-0.7893	-0.7845
6-Apr-10	-0.7046	-0.7732	-0.7693	-0.7896
6-Jun-10	-0.6271	-0.7361	-0.6554	-0.6995
6-Aug-10	-0.5469	-0.5802	-0.6103	-0.7152

A perfect inverse correlation between the results would be -1. However, many of the results are generally lower than -0.75. This still shows a strong inverse correlation between the density difference and the estimated ballistic coefficient and therefore a fitted ballistic coefficient that is potentially absorbing errors. This could be occurring because of poor density estimates or other modeling errors.

A closer look at the estimated drag coefficient shows how poorly estimated the ballistic coefficient was. The estimated drag coefficient for August 17, 2009 is shown in Figure 15.

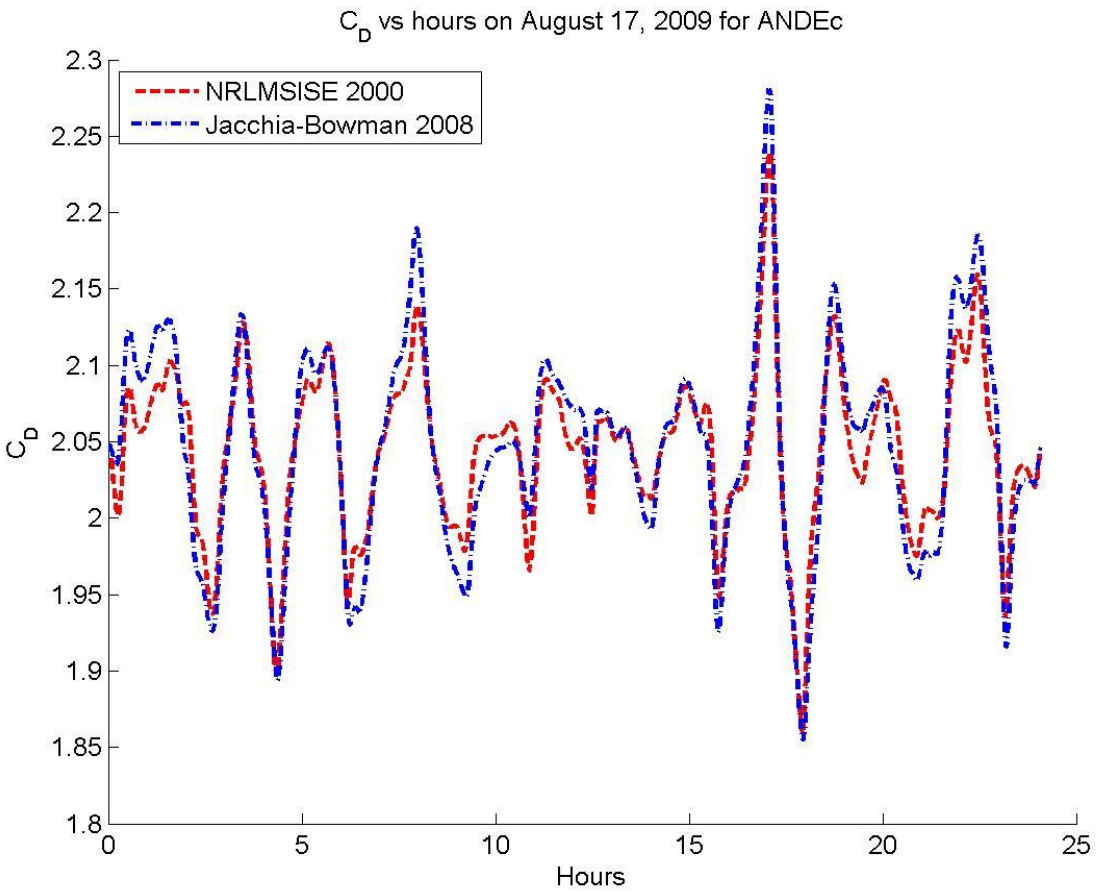

Figure 15: Estimated drag coefficient for August 17, 2009

The drag coefficient varies by as much as 0.43 between the highest and lowest estimated drag coefficient. This is approximately the expected difference between the highest and lowest drag coefficients over the entire lifespan of ANDE-2 as shown in Table 18. This shows that the estimated drag coefficient is likely absorbing significant errors from the different atmospheric models using the optimal orbit determination method. This also proves the necessity for the drag coefficient to be calculated through other means such as the physics based GSI method.

3.2. Solar and Geomagnetic Activity over ANDE-2 Lifespan

Two of the major contributors to variations in the atmospheric density and temperature are the solar and geomagnetic activity levels. This means that the accommodation coefficient models that include the effects of variations in the atmospheric density levels of oxygen and atmospheric temperature will ultimately lead to changes in the drag coefficient of the satellite for said variations. This should mean that abrupt changes in the solar and geomagnetic levels may produce noticeable changes in the C_D for ANDEc during its lifespan. Figure 16 shows the solar and geomagnetic activity levels experienced by ANDEc over its lifespan.

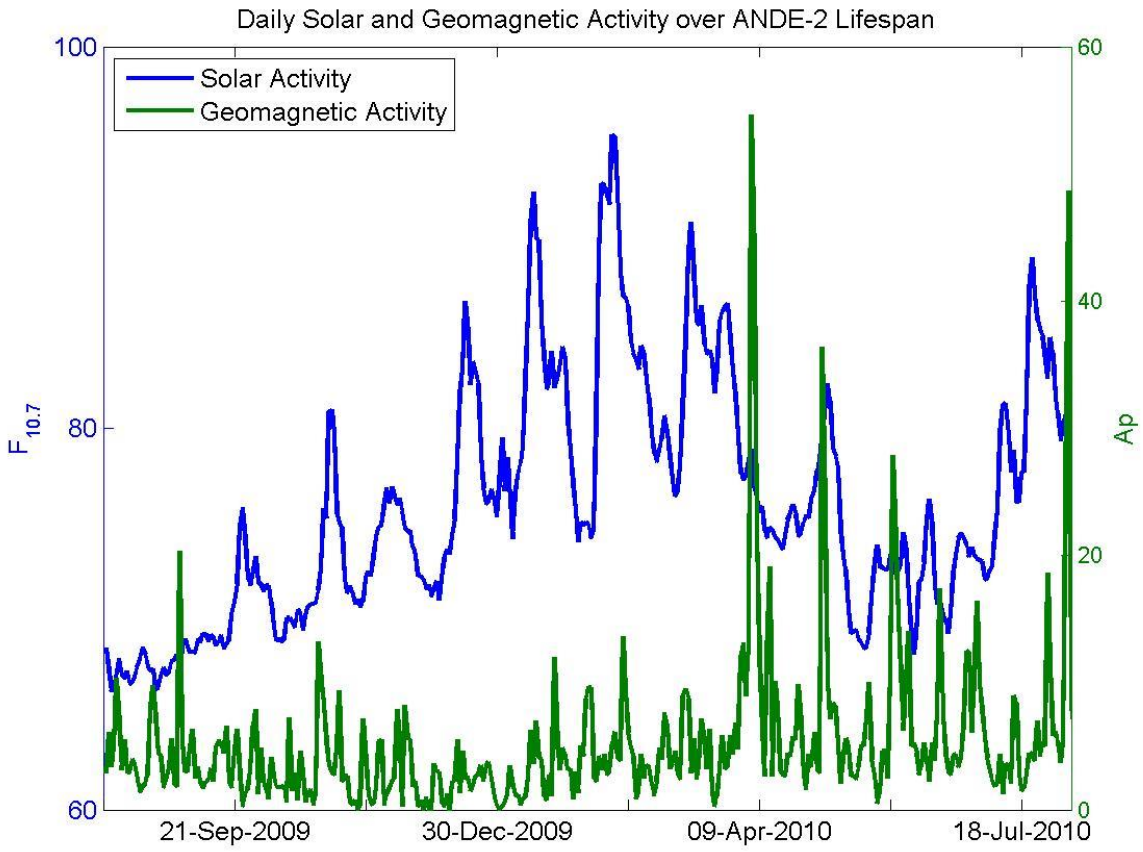

Figure 16: Solar and Geomagnetic activity of ANDEc lifespan

3.3. Drag Coefficients over ANDE-2 Lifespan

ANDEc and ANDEp remained relatively close for a short period of time near the beginning of their mission and thus should have seen some similarities in their drag coefficients and derived atmospheric densities. Figure 17 shows the arc distance separation between ANDEc and ANDEp over a fifteen day period.

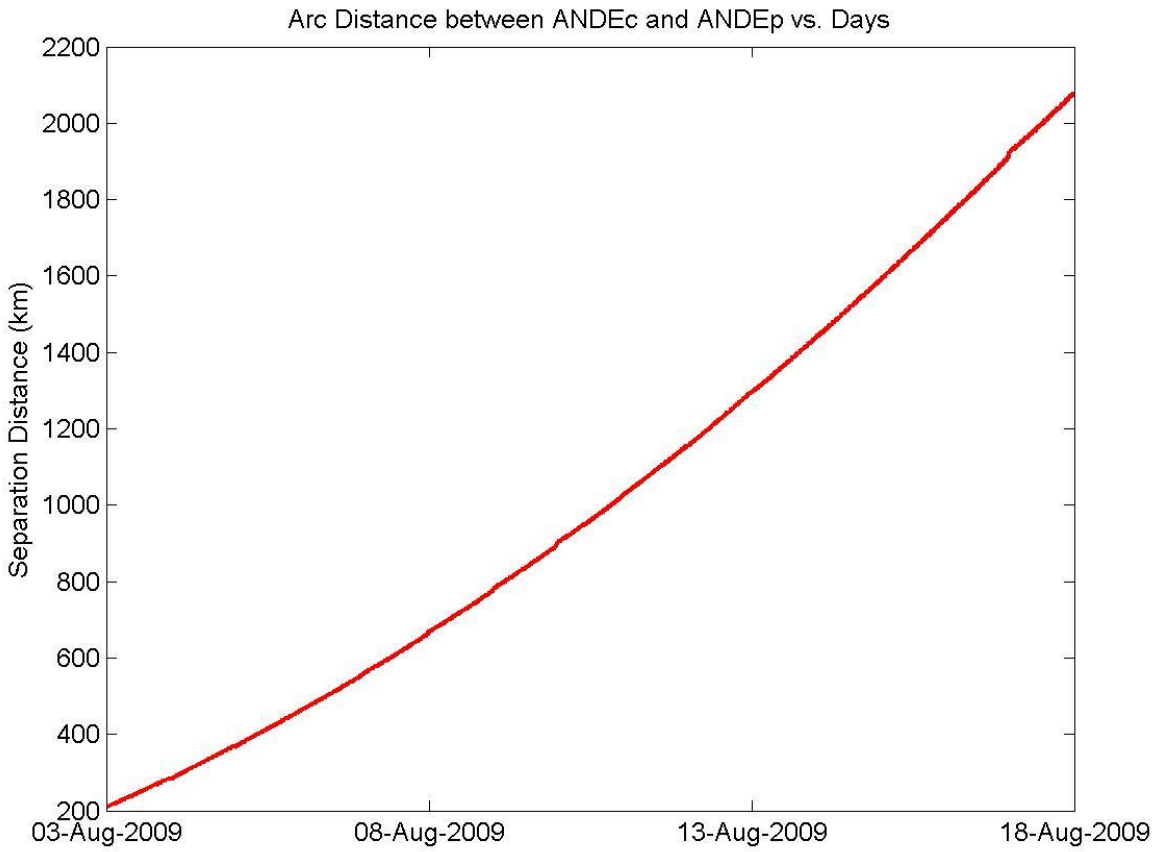

Figure 17: Arc separation distance between ANDEc and ANDEp

Figure 17 shows that the separation distance between ANDEc and ANDEp increases exponentially. However, the satellites should be close enough within this time span to see similarities in the drag coefficients and POE derived densities.

The three different accommodation models mentioned in section 2.10 were used in unison with the DRIA GSI model to determine the drag coefficients ANDEc and ANDEp experienced over their operational lifespan. Each day was analyzed individually and an average drag coefficient was determined for each day and each temperature of interest: expected highest, expected lowest, and average. Figure 18 and Figure 19 show the expected C_D over ANDEc's and ANDEp's lifespan using the altitude data fit method for the accommodation coefficient determination.

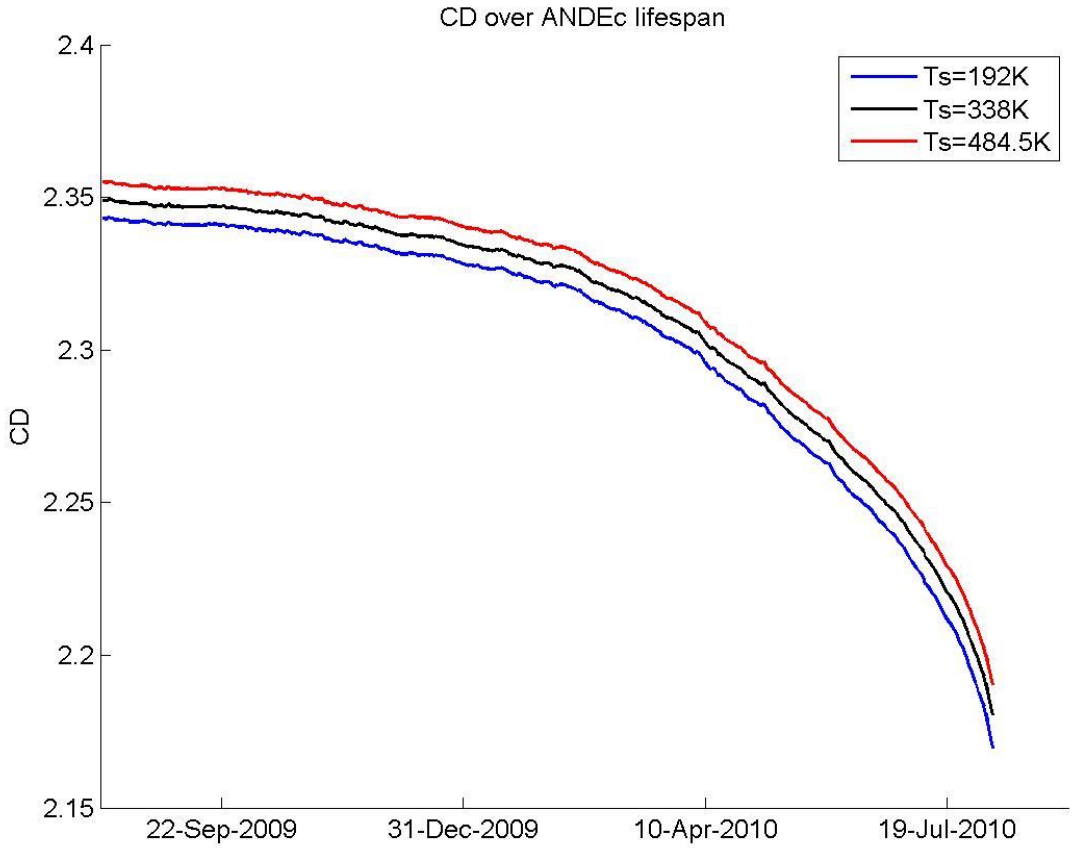

Figure 18: C_D over ANDEc lifespan using altitude data fit (Bowman and Moe, 2006)

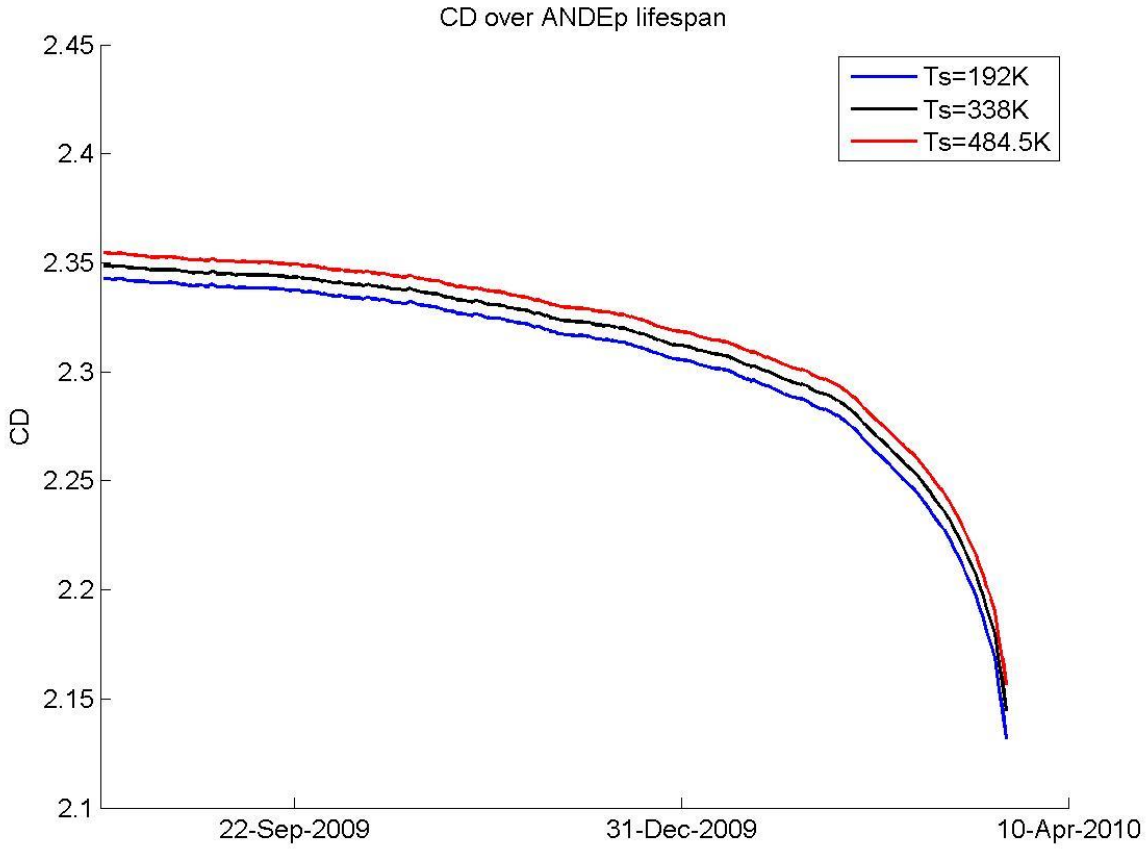

Figure 19: C_D over ANDEp lifespan using altitude data fit (Bowman and Moe, 2006)

The altitude data fit method shows a steady decline in C_D over much of ANDEc's lifespan with a particular sharp decline around May 2010 and ANDEp begins to decline sharply around February 2010. This is because of ANDEp's lower mass, which made it more susceptible to the effects of drag. The daily average C_D follows ANDEc's altitude trend and shows no variation from solar and geomagnetic activity. This particular method of calculating C_D merely supplies an approximate answer based on empirical evidence that can be compared to the other semi-empirical models examined in this thesis.

The second method used for determining the C_D over ANDEc's and ANDEp's lifespan involved using the Langmuir Isotherm method developed by Pilinski et al. (2010). Because this method relates the empirical data for the accommodation coefficients back to the atmospheric conditions, variations in the C_D caused by solar and geomagnetic activity are evident in the C_D graphs shown in Figure 20 and Figure 21.

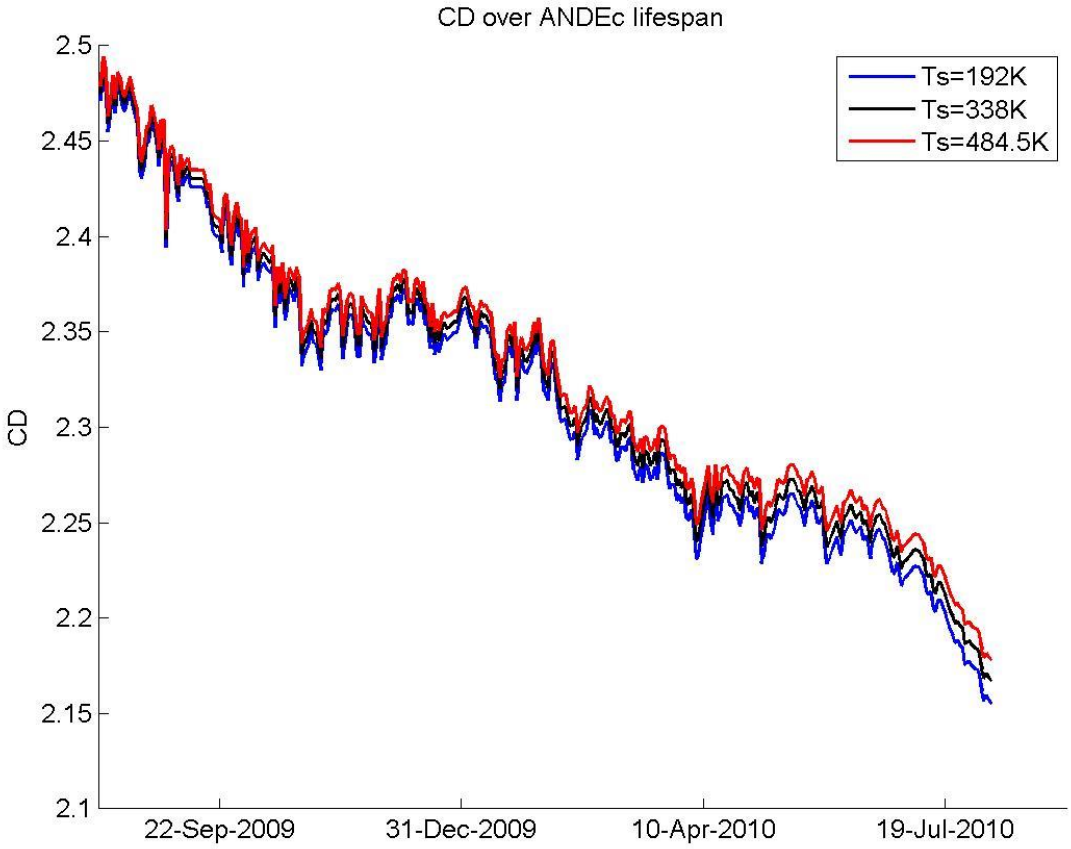

Figure 20: C_D over ANDEc lifespan using Langmuir isotherm (Pilinski et al., 2010)

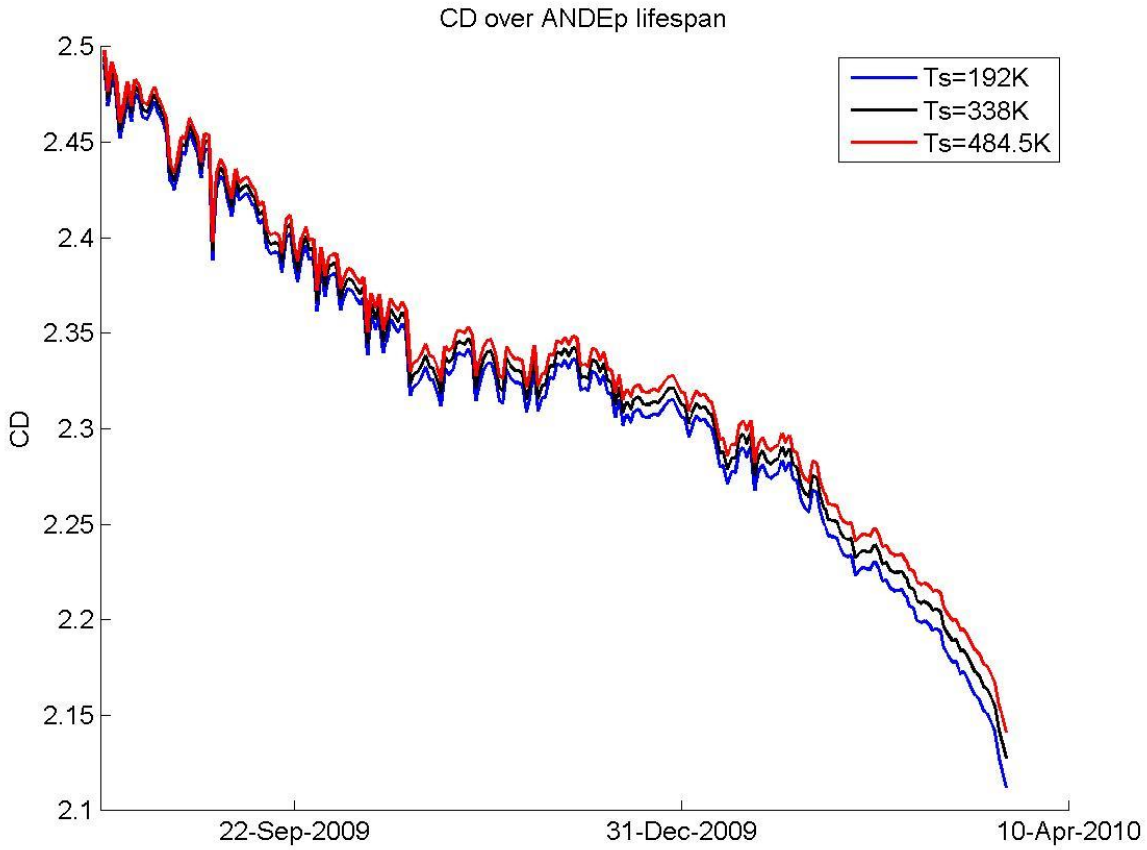

Figure 21: C_D over ANDEp lifespan using Langmuir isotherm (Pilinski et al., 2010)

The sharp decline at the beginning of ANDEc's and ANDEp's life is likely caused because of the asymptotic nature of the Langmuir isotherm for low atmospheric density conditions and due to the error that is associated with this method for below 0.85 accommodation coefficient conditions. The graph begins to level off near October of 2009 where the accommodation coefficient began to reach 0.85. This leveling off may also be due to the increase in solar activity at that time around the beginning of October 2009. The large downward spike around the end of October 2009 and subsequent downward spikes around April 2010 and May 2010 seem to correspond to the geomagnetic storms around those times.

The third method for determining the C_D over ANDEc's and ANDEp's lifespan used the Langmuir isotherm method developed by Walker et al. (2014) and is shown in Figure 22 and Figure 23.

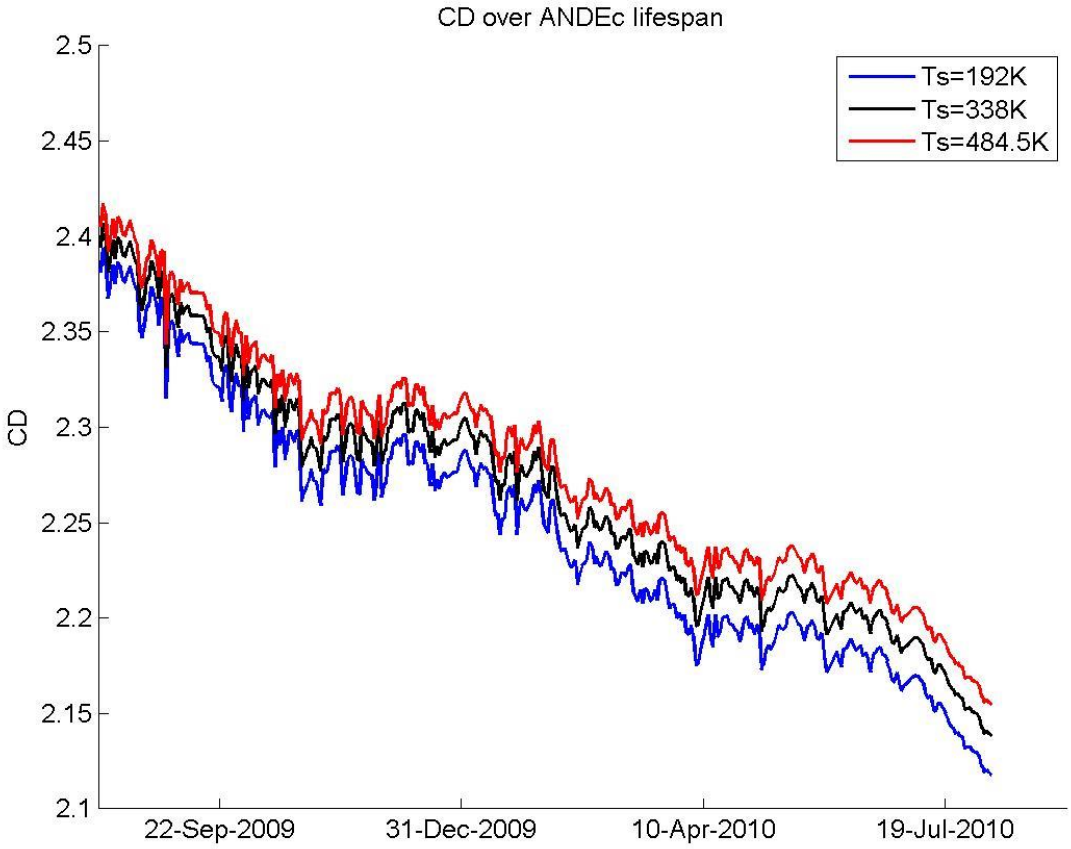

Figure 22: C_D over ANDEc lifespan using Langmuir Isotherm (Walker et al., 2010)

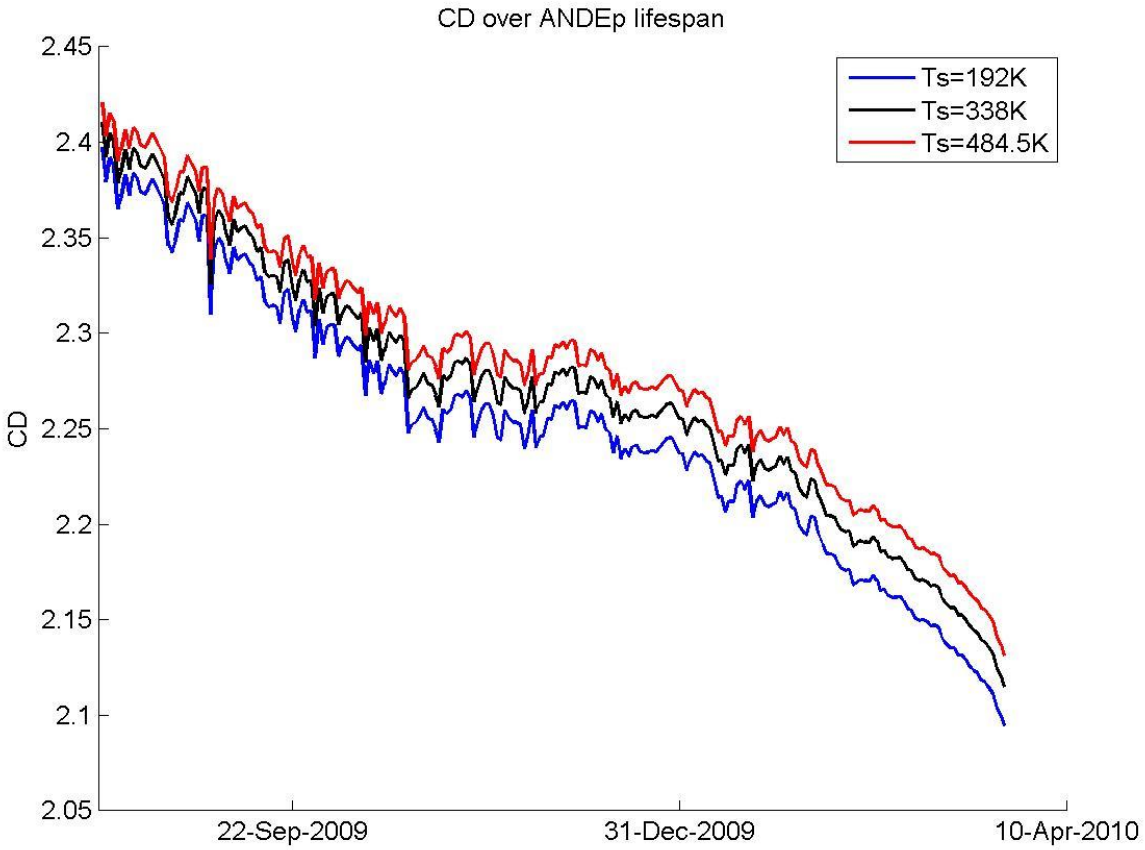

Figure 23: C_D over ANDEp lifespan using Langmuir Isotherm (Walker et al., 2010)

Because this method related the Langmuir isotherm to the fraction of the satellite's surface covered by atomic oxygen, variations in the C_D over each day are slightly different from the C_D obtained using the Pilinski et al. (2010) method. This is especially evident at the end of ANDEc's lifespan with the large separation between the three different C_D lines corresponding to the satellite surface temperature. This is because the C_D variation over each day is less dramatic with this particular method than the Pilinski et al. (2010) method. This will be more evident in the following sections.

A comparison between all three accommodation coefficient models is shown in Figure 24 and Figure 25. The Langmuir isotherm model developed by Walker et al. (2010) provides significantly smaller

C_D values than the other two models. Two things may be responsible for this difference: (1) The molecular mass of the ANDE-2 satellites was simply assumed to be aluminum. In reality, the satellite was covered by retro-reflectors that most likely had a different molecular mass density. This would have contributed to a different total molecular mass thereby raising or lowering the value of the expected C_D. (2) The model was developed using empirical C_D data obtained by satellites during periods of high solar activity. The Pilinski et al. (2010) method utilized empirical data from satellites that experienced both high and low solar conditions. The Walker et al. (2010) method did not. This could have contributed to a model that is biased at low solar activity, especially since Walker et al. (2014) used altitude as one of the parameters in their fit calculations.

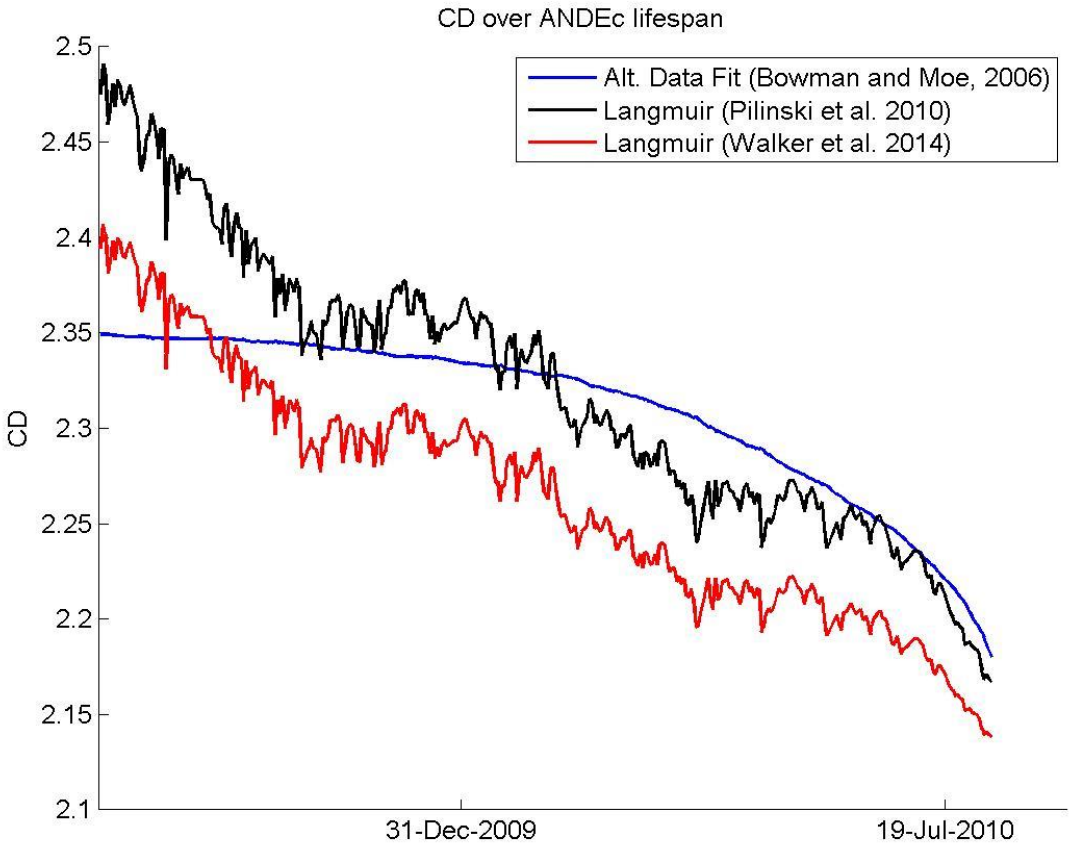

Figure 24: C_D over ANDEc lifespan using all three accommodation coefficient models at average temperature

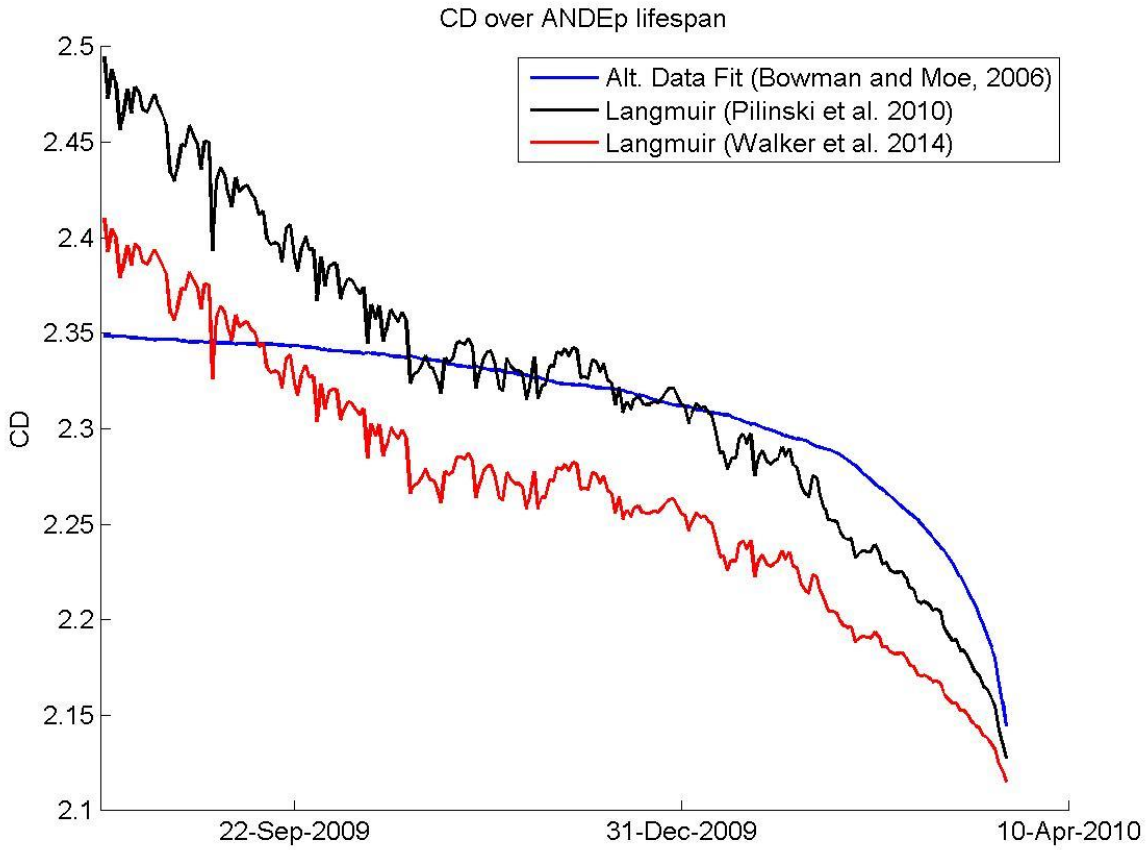

Figure 25: C_D over ANDEp lifespan using all three accommodation coefficient models at average temperature

Because the Langmuir isotherm model developed by Walker et al. (2010) seemed that it may be biased at lower solar conditions and consequentially lead to lower drag coefficients, the Langmuir isotherm developed by Pilinski et al. (2010) will be used as the baseline accommodation coefficient model.

3.4. Daily Drag Coefficient Variations for ANDE-2

The arc distance separation between ANDEc and ANDEp around August 6, 2009 was approximately 500 km. This day was chosen because some of the data for the earlier days contained possibly inaccurate data, which produced poor estimated atmospheric density results. Figure 26 shows the comparison between ANDEc's and ANDEp's drag coefficients for August 6, 2009.

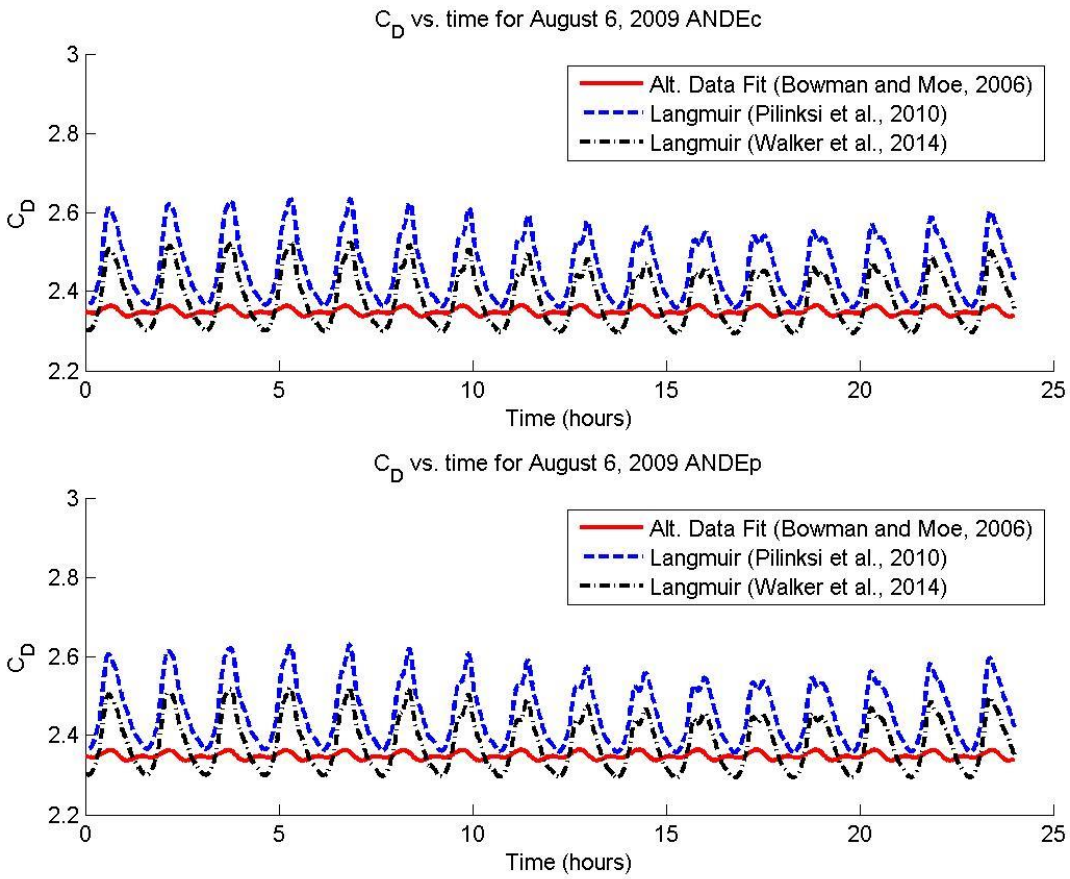

Figure 26: Drag coefficient comparison for ANDEc and ANDEp on August 6, 2009

The difference between the two plots is virtually indistinguishable. Figure 27 shows the difference between ANDEc's and ANDEp's drag coefficients for the same day.

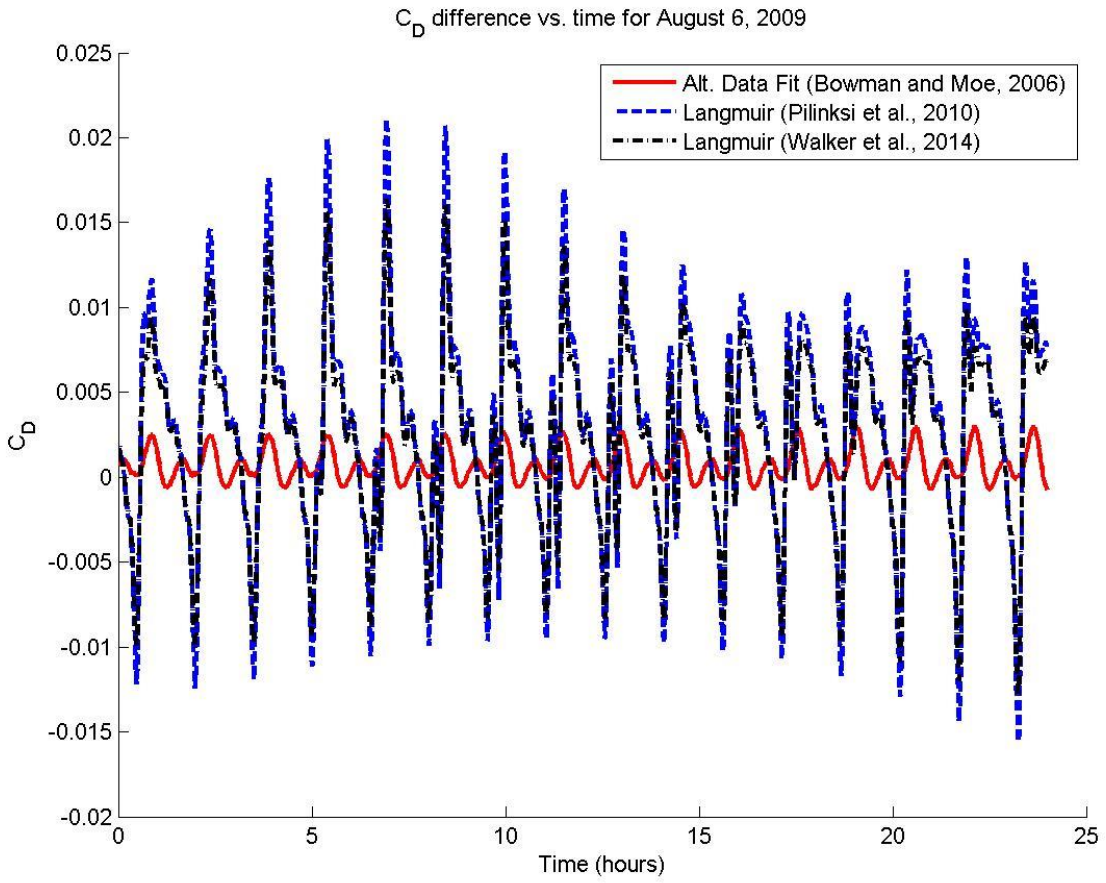

Figure 27: Difference between ANDEc and ANDEp drag coefficients on August 6, 2009

The variation in C_D for ANDEc and ANDEp is small. Therefore, the estimated densities for this day should also be small. The next three days will only be analyzed for ANDEc due to its longer lifespan.

Three drag coefficient plots are shown below for three days over ANDEc's lifespan in the following figures. For the purpose of simplification, only the C_D plots using the average temperature are included in the graphs, which include C_D plots using the three accommodation coefficient models. The C_D averages for each day and each temperature are listed in Table 20 and the abbreviations used in this table are as follows: altitude data fit (Bowman and Moe (2006)) (ADF), Langmuir isotherm using Pilinski et al. (2010) method (LP), and Langmuir isotherm using Walker et al. (2014) method (LW). The difference in the C_D

over the satellite surface's maximum and minimum temperatures is relatively small and differs most at the end of ANDEc's life. The reason for the greater variation in the C_D relative to the satellite's surface temperature is due to the reduction in variation of C_D as the accommodation coefficient converges to 1.

Table 20: Average drag coefficients for different days and temperatures

Average Drag Coefficients									
Dates	ADF T=192K	LP T=192K	LW T=192K	ADF T=338K	LP T=338K	LW T=338K	ADF T=484.5K	LP T=484.5K	LW T=484.5K
6-Oct-09	2.34	2.39	2.31	2.35	2.39	2.33	2.35	2.40	2.34
6-Feb-10	2.32	2.32	2.25	2.33	2.33	2.27	2.33	2.33	2.28
6-Aug-10	2.17	2.16	2.12	2.18	2.17	2.14	2.19	2.18	2.16

Figure 28 shows the variations in C_D over a 24 hour period using the three different accommodation models at the average expected temperature. The day October 6, 2009 was chosen because the accommodation coefficient for that day was slightly above 0.85 (α=0.864), and therefore was above the value Pilinski et al. (2010) deemed acceptable. The altitude data fit method provided the least amount of variation in C_D as expected since this model did not take into account variations in the atmospheric composition. The other two methods that did take into account variations in the atmospheric composition showed greater variations in C_D by as much as approximately 0.24. This is due to the nature of the Langmuir isotherm's shape which causes greater variations in the accommodation coefficient for night and day differences in the temperature and atmospheric composition.

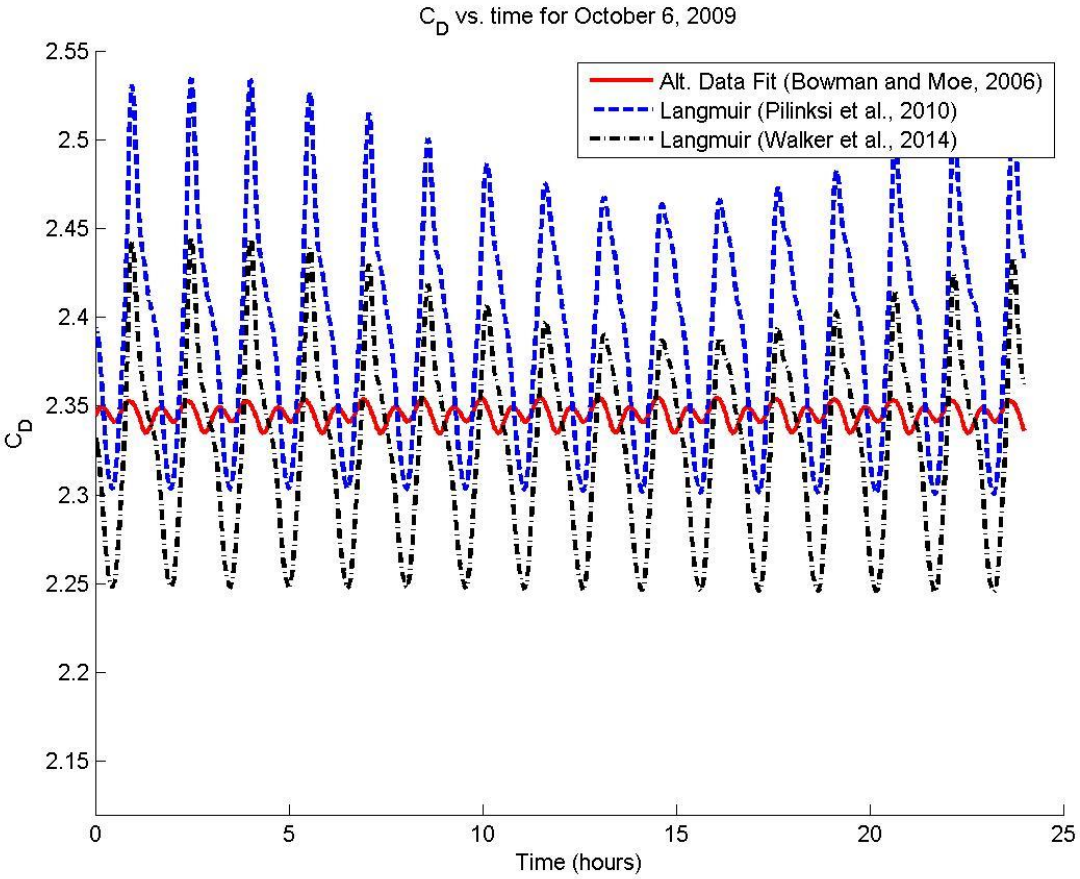

Figure 28: C_D vs. time for October 6, 2009 using the three accommodation coefficient models for ANDEc

The graph shown in Figure 29 depicts the C_D variations throughout February 6, 2010. The variations in the drag coefficients calculated using the Langmuir isotherm method are about half of what they were for the day previously shown. This is an expected result as the Langmuir isotherm varies less as the atmospheric density goes up.

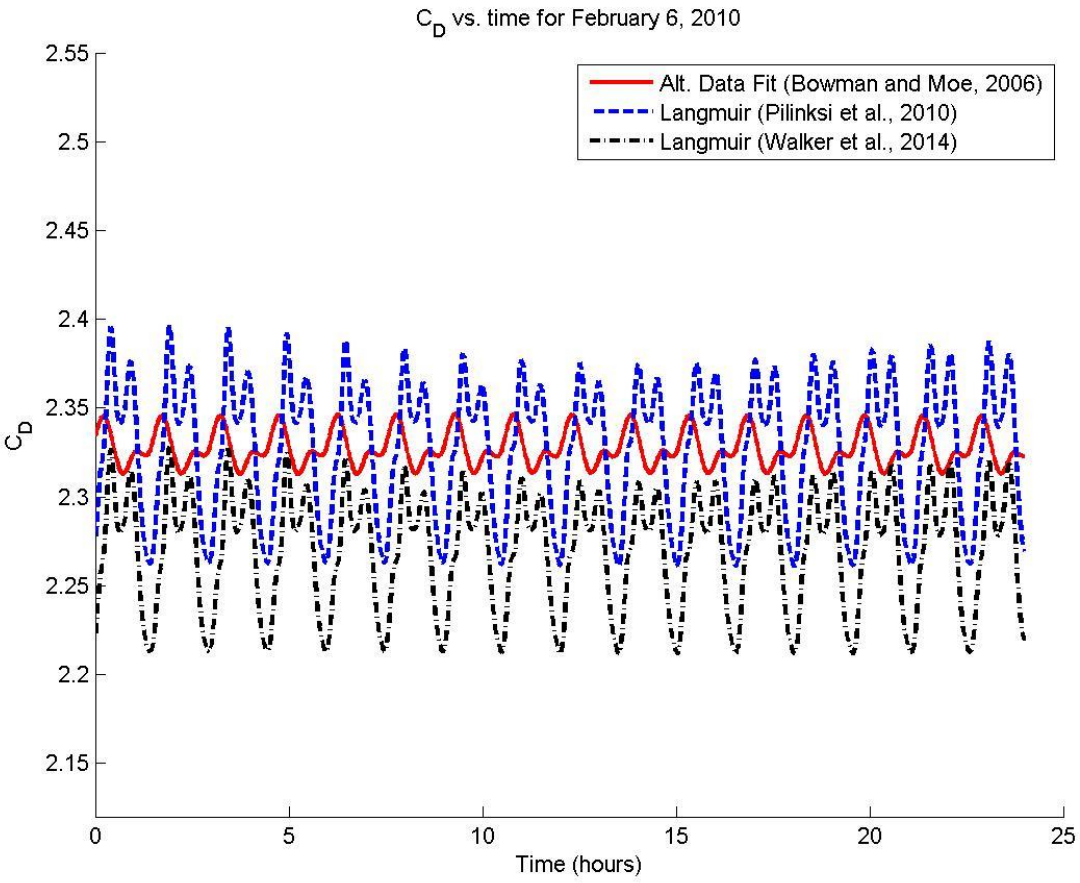

Figure 29: C_D vs. time for February 6, 2010 using the three accommodation coefficient models for ANDEc

Figure 30 shows the variations in the C_D on August 6, 2010, which is near the end of ANDEc's life. The variations in the C_D for this day are far less than the variations in C_D for the previously shown days. As previously mentioned, this is due to the accommodation coefficient converging to 1 as the atmospheric pressure increases.

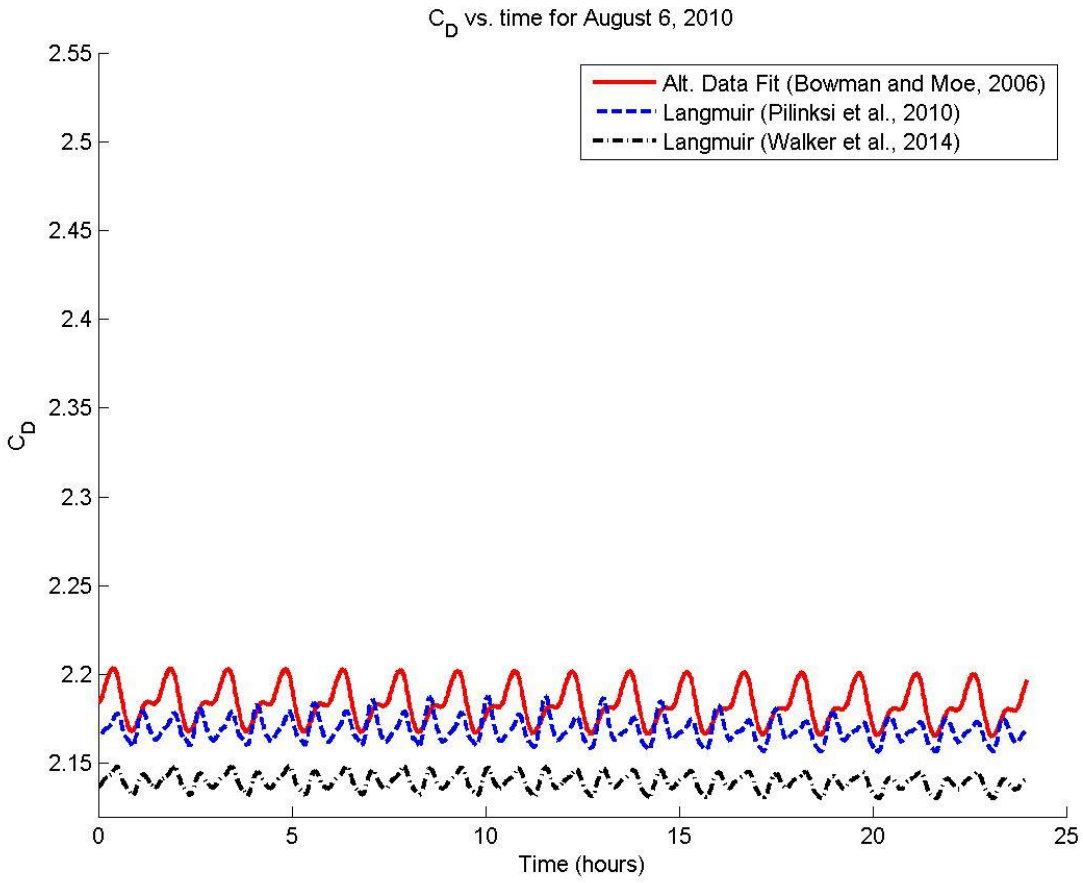

Figure 30: C_D vs. time for August 6, 2010 using the three accommodation coefficient models for ANDEc

Figure 31 and Figure 32 help visualize the reason for variations in the C_D being greater for satellite surface temperature variations at the end of ANDEc's life. The drag coefficients for both graphs were calculated using the Langmuir isotherm method from Pilinski et al. (2010).

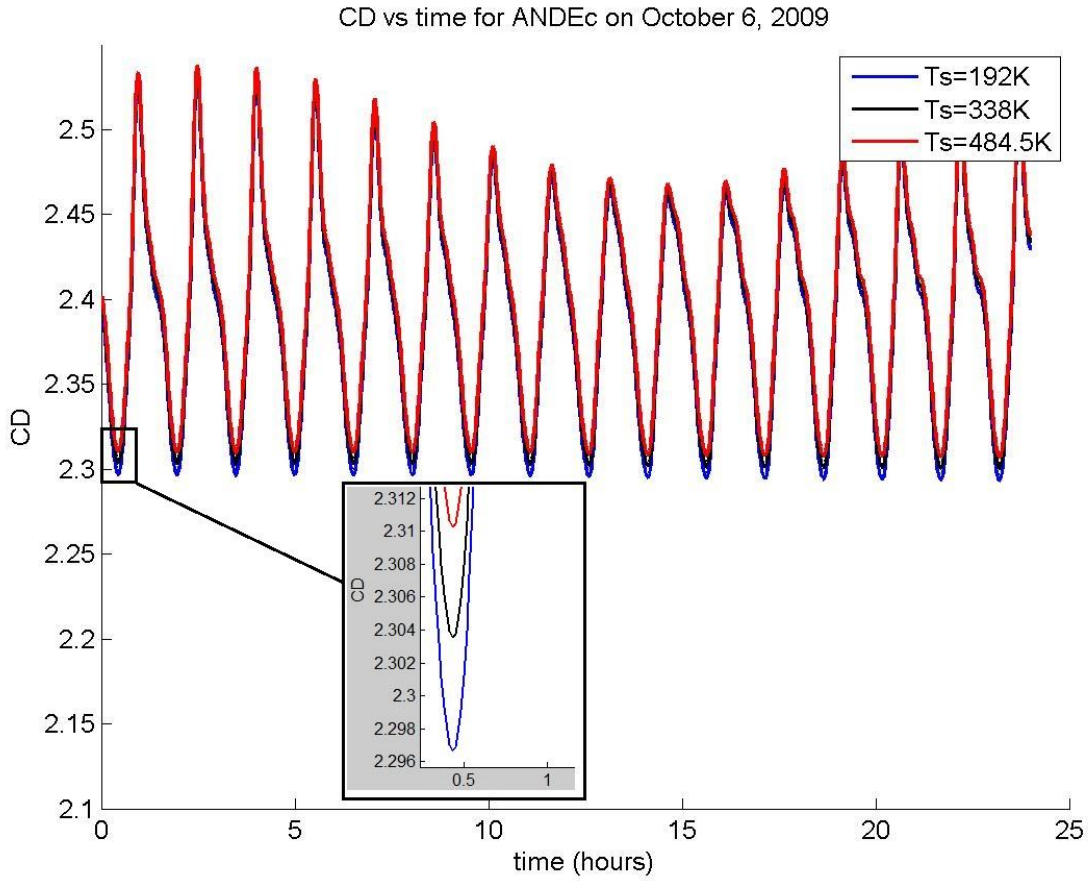

Figure 31: C_D vs. time for different satellite surface temperatures for ANDEc on October 6, 2009

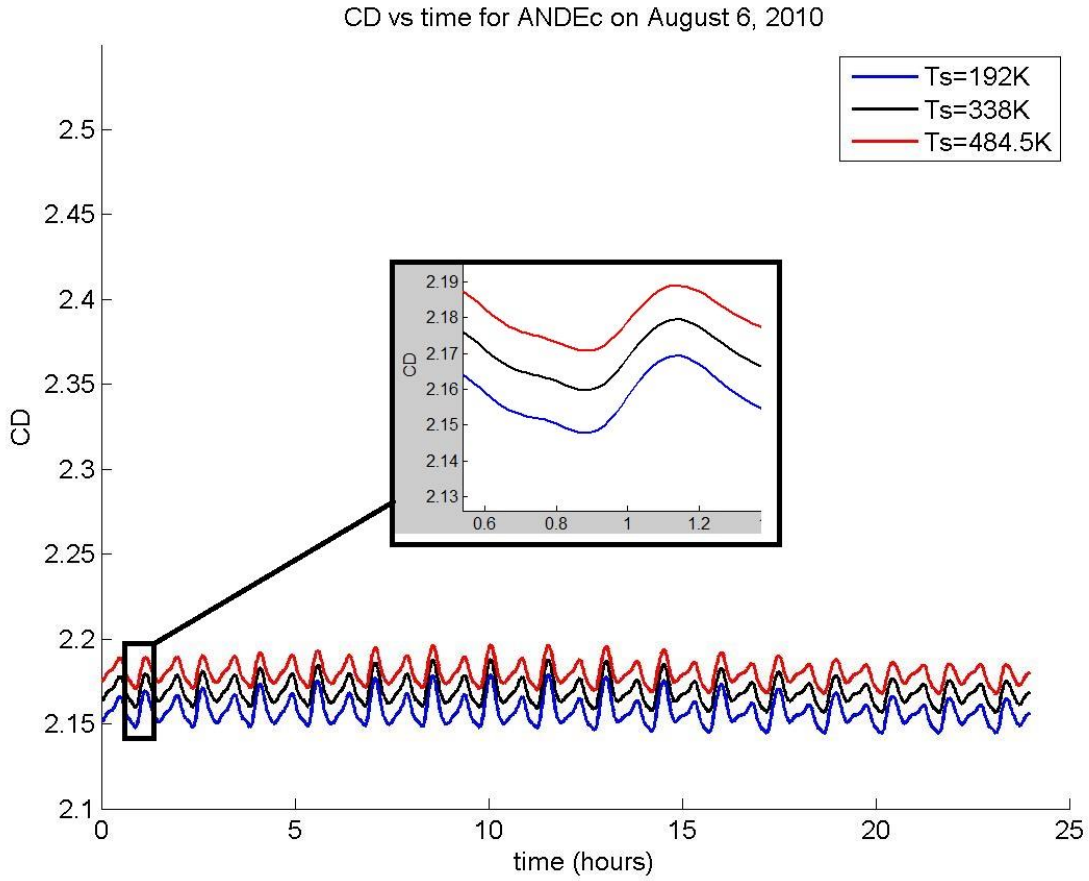

Figure 32: C_D vs. time for different satellite surface temperatures for ANDEc on August 6, 2010

The separation between the maximum and minimum C_D for each satellite surface temperature is relatively close for both days (about 0.014-0.028), but the total variation in the C_D for each satellite surface temperature decreased as the satellite experiences higher atmospheric density and thereby higher atmospheric pressure. This means that variations in the surface temperature of a satellite will affect the C_D most at the end of that satellite's lifespan. However, the variation of the satellite's surface temperature only causes at most about a 2% difference in the C_D.

3.5. Atmospheric Density Analysis for Various Days

The drag coefficients for ANDEc and ANDEp on August 6, 2009 were both 2.46. The estimated atmospheric densities from now on will be referred to as Precision Orbit Ephemeris (POE) derived densities. Figure 33 shows the model and POE derived densities for ANDE-2 on August 6, 2009.

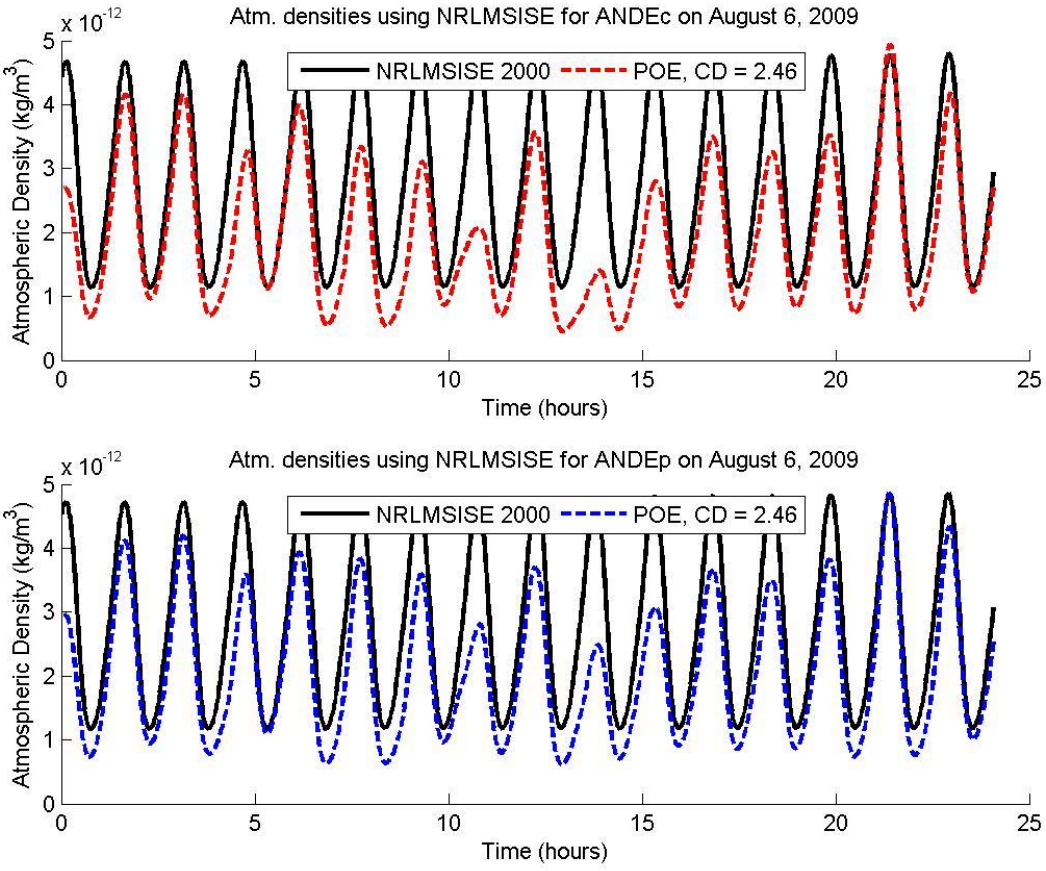

Figure 33: Model and POE derived densities for ANDEc and ANDEp on August 6, 2009

As expected, both satellites exhibited similar model and POE derived densities with minor visible dissimilarities. This is expected as the satellites were not close to one another but would pass through similar atmospheric conditions at relatively similar altitudes.

The atmospheric densities for the three days chosen in section 3.4 are shown in the following figures. The max and min C_D values are 2.6 and 2.08 as were found in the introduction and are plotted on each graph along with the C_D obtained using the Langmuir isotherm (Pilinski et al., 2010) (LP), and the original C_D found by Lechtenberg (2015) using the 1.8 ballistic coefficient half-life (BCHL).

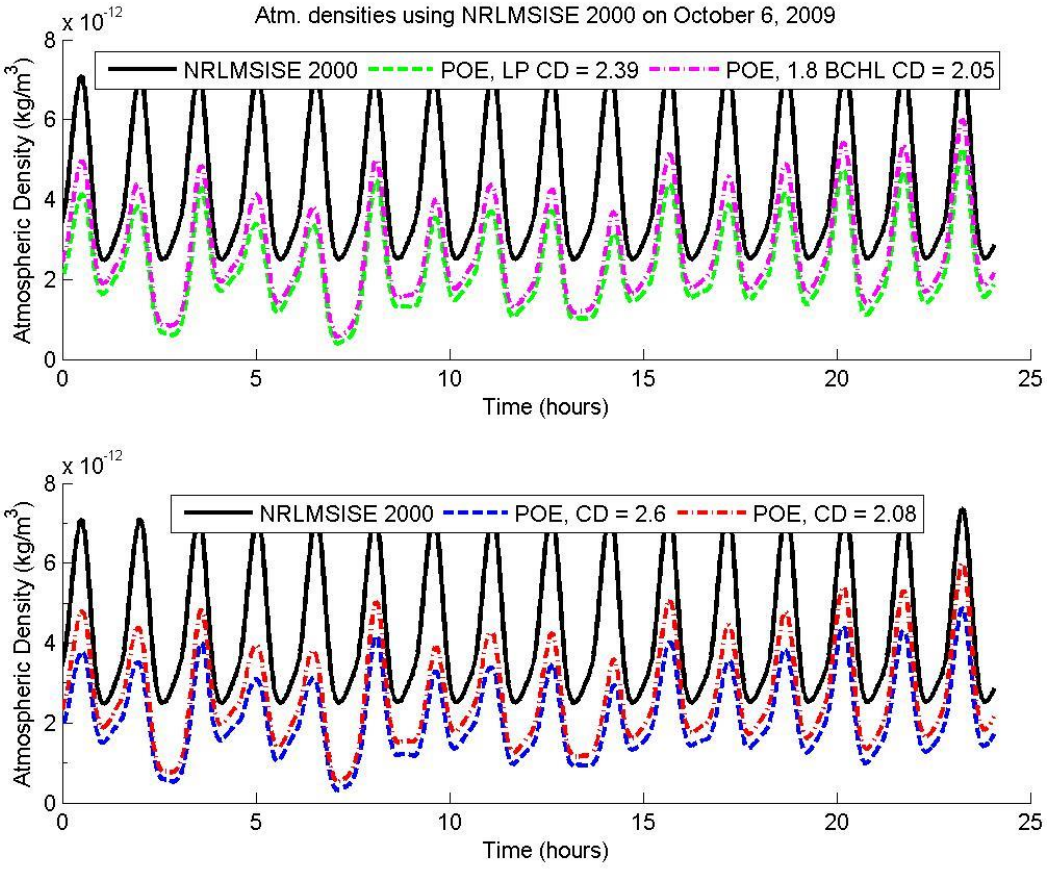

Figure 34: Atmospheric density for ANDEc on October 6, 2009

Figure 34 shows that the NRLMSISE 2000 model atmospheric densities are overestimated compared to all POE derived densities.

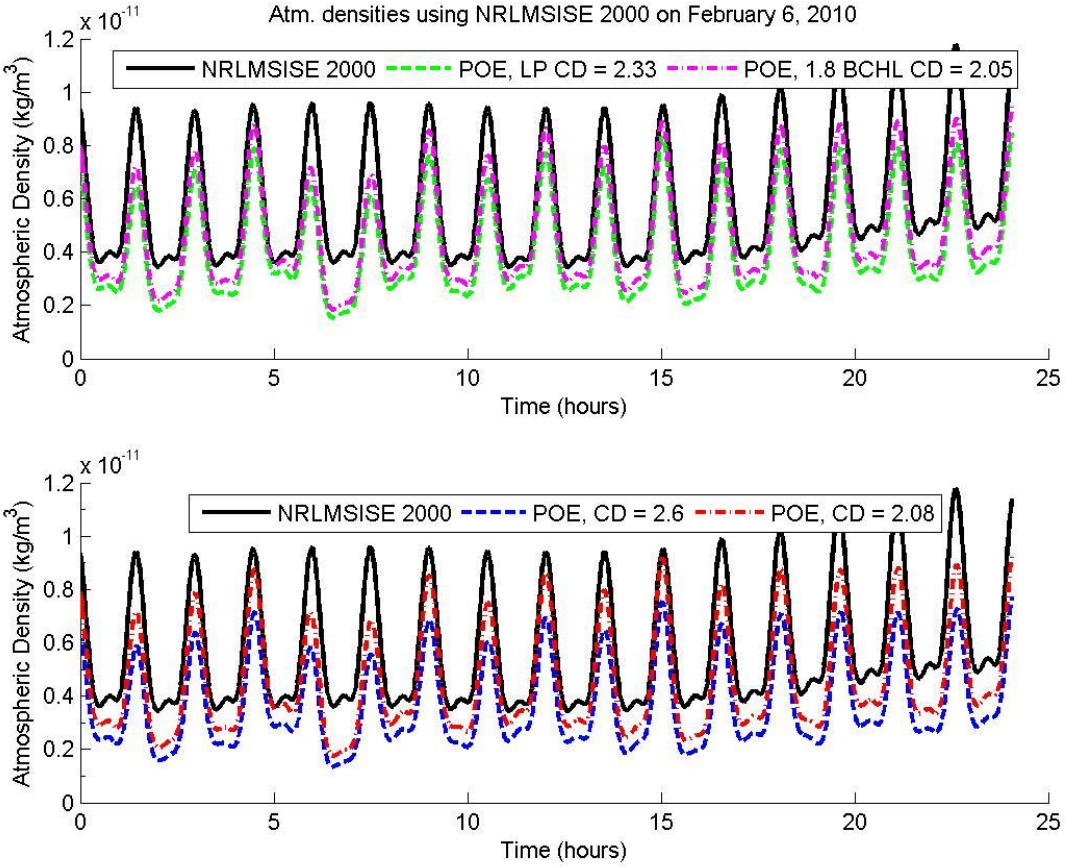

Figure 35: Atmospheric density for ANDEc on February 6, 2010

Figure 35 shows the atmospheric densities for ANDEc during the middle of its life. The NRLMSISE 2000 densities are still higher than the POE derived densities.

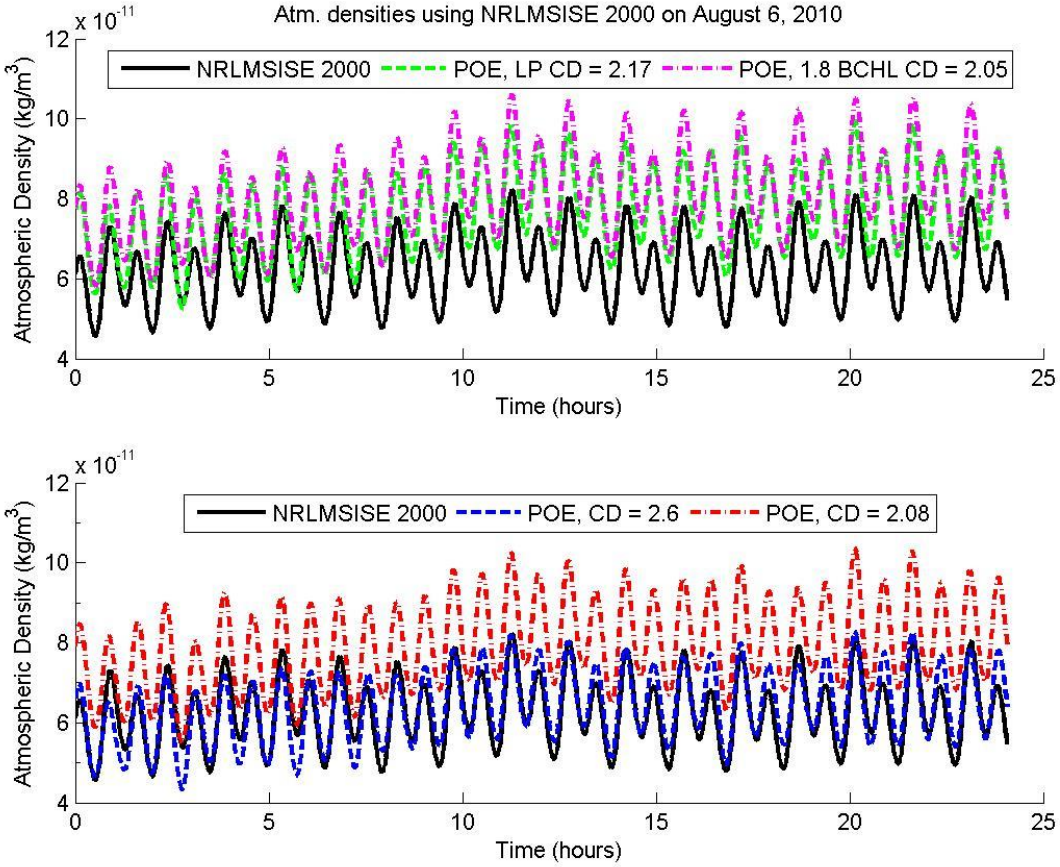

Figure 36: Atmospheric density for ANDEc on August 6, 2010

Figure 36 show the atmospheric densities for ANDEc near the end of its life. The NRLMSISE-00 atmospheric density here is considerably underestimated compared to most of the POE derived densities.

3.6. Density Dependence Analysis for Different Atmospheric Models

The density dependency plots and tables in this section were developed as a comparison to the results found by Lechtenberg (2015). The results here were produced using better C_D data. The density data in this section was obtained by performing individual runs in the ODTK program for each specific day. Each day was assigned a drag coefficient obtained using the GSI equations with the Langmuir isotherm (Pilinski et al., 2010) and the average expected temperature. The drag coefficients used in this section are shown in Figure 20.

3.6.1. Daily Density Dependence for ANDE-2

The density data were binned into daily bins and examined for variations in the *DCF* and *UBSTD* for the day, solar activity, and geomagnetic activity experienced by ANDEc and ANDEp over their life spans.

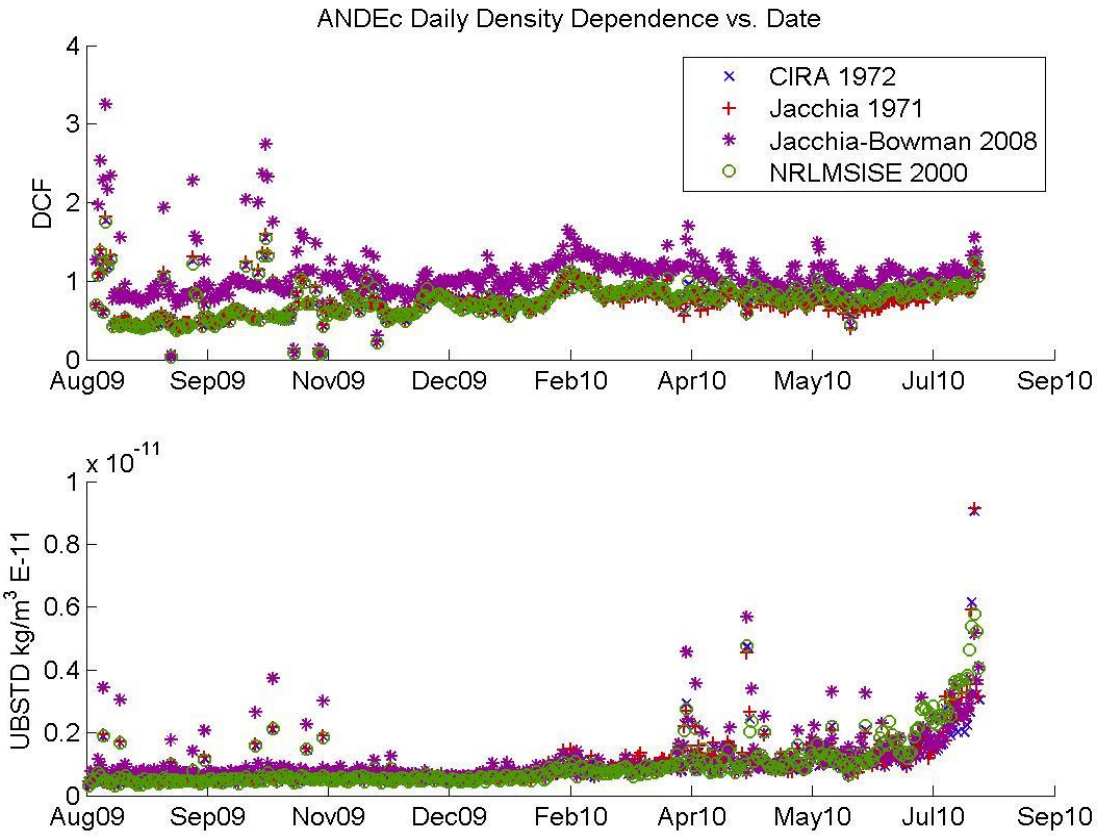

Figure 37: Daily variations in the *DCF* and *UBSTD* for ANDEc

The *UBSTD* increases sharply at the end of ANDEc's life around July 2010. This is most likely due to the decaying orbit of the ANDEc satellite which re-entered on August 18, 2010. The outliers are possibly due to inaccurate initial conditions that resulted in subsequent observations being discarded according to Lechtenberg (2015).

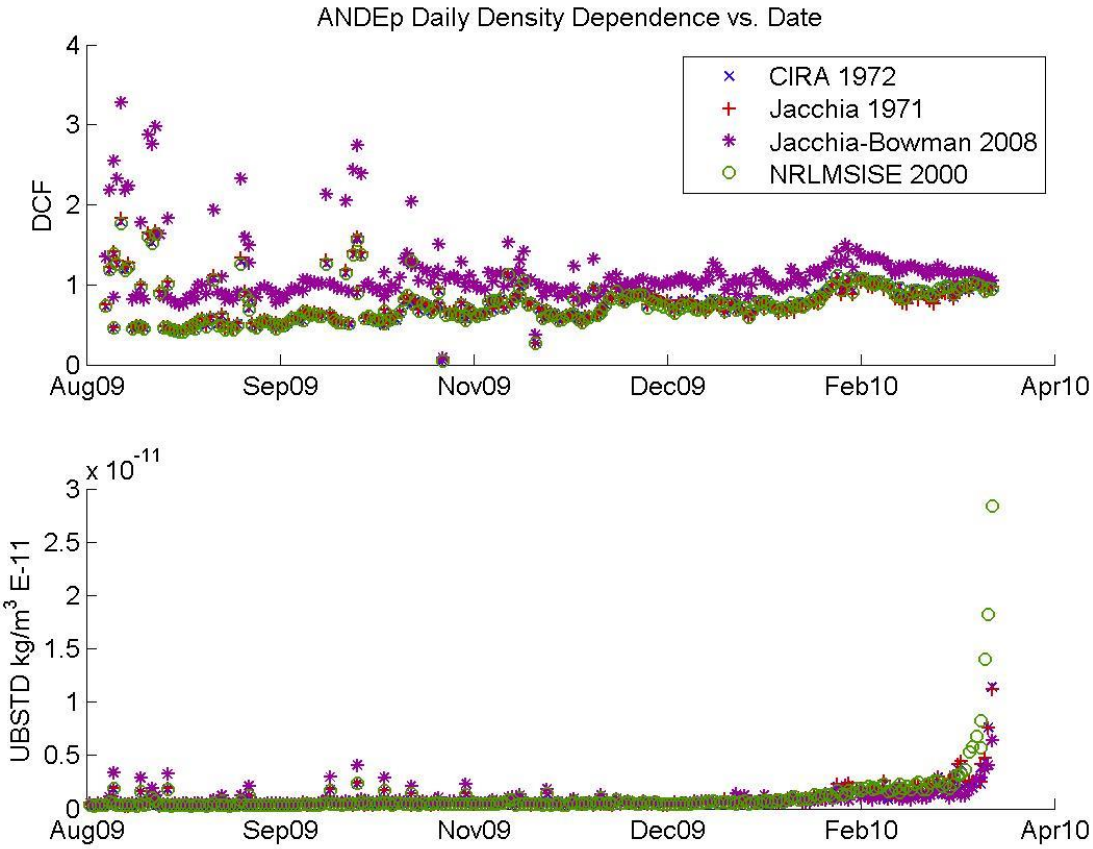

Figure 38: Daily variations in the *DCF* and *UBSTD* for ANDEp

Figure 38 shows the same basic trend for the DCF and UBSTD experienced by ANDEc over its lifespan with a sharp upward trend for the UBSTD at the end of ANDEp's life. The larger numbers for the UBSTD at the end of ANDEp's life in comparison to the UBSTD values at the end of ANDEc's life, is likely due to the fact that ANDEp's SLR orbit data were available for the last day before its re-entry date. ANDEc's SLR data were only available till about 10 days before its re-entry date. The SLR data for ANDEp's last few days were also for lower altitudes than ANDEc's end-of-life SLR data.

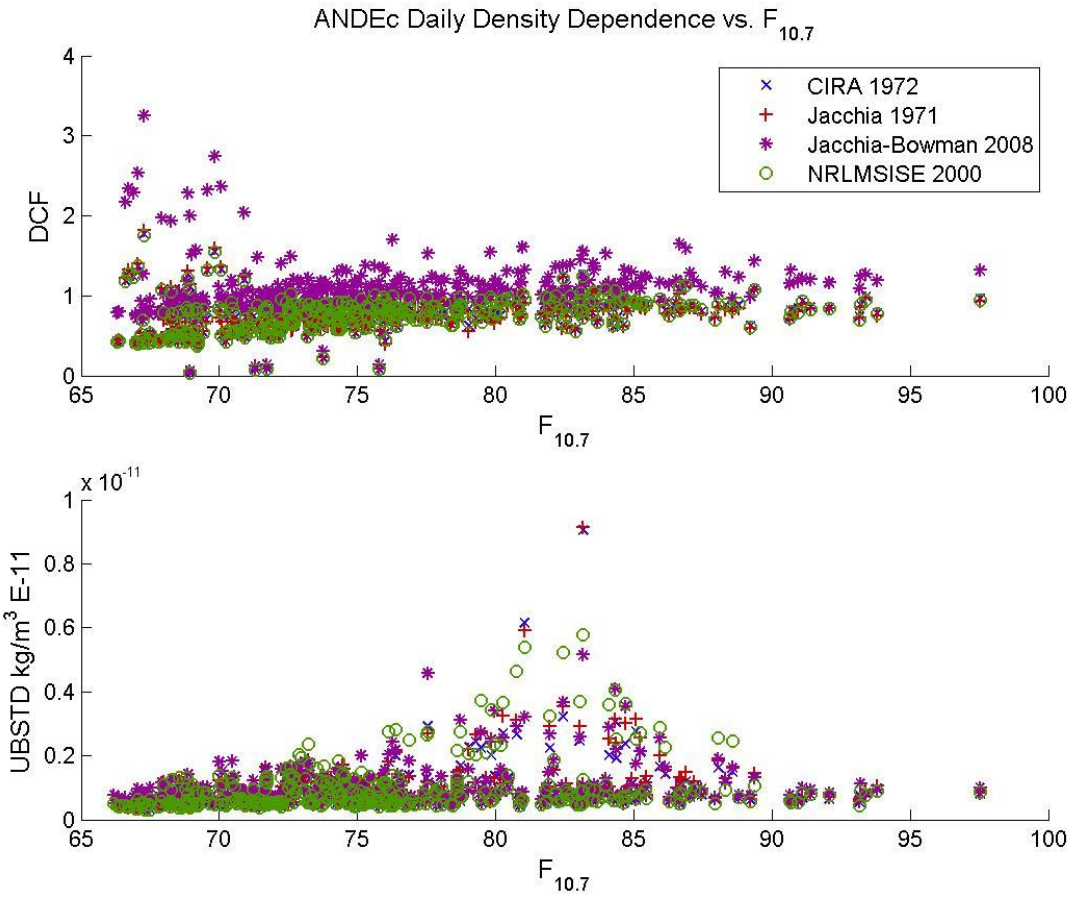

Figure 39: Variations in the *DCF* and *UBSTD* for ANDEc relative to daily solar activity

The *DCF* and *UBSTD* appear to have little dependence on the solar activity. The *UBSTD* increases around 80 to 85 $F_{10.7}$ which is likely due to those solar activity levels being near the end of ANDEc's life.

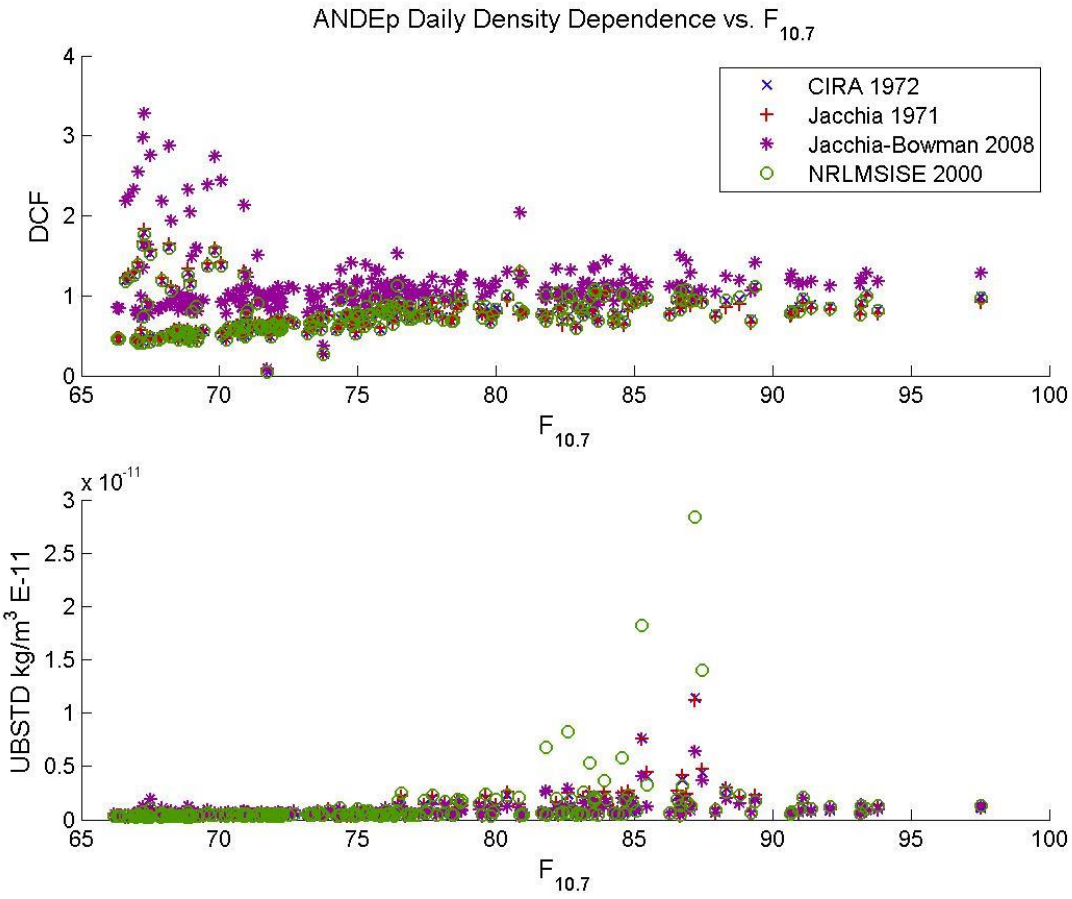

Figure 40: Variations in the *DCF* and *UBSTD* for ANDEp relative to daily solar activity

Little dependence for the DCF and UBSTD is evident in Figure 40. The higher UBSTD values correspond to the solar activity at the end of ANDEp's life.

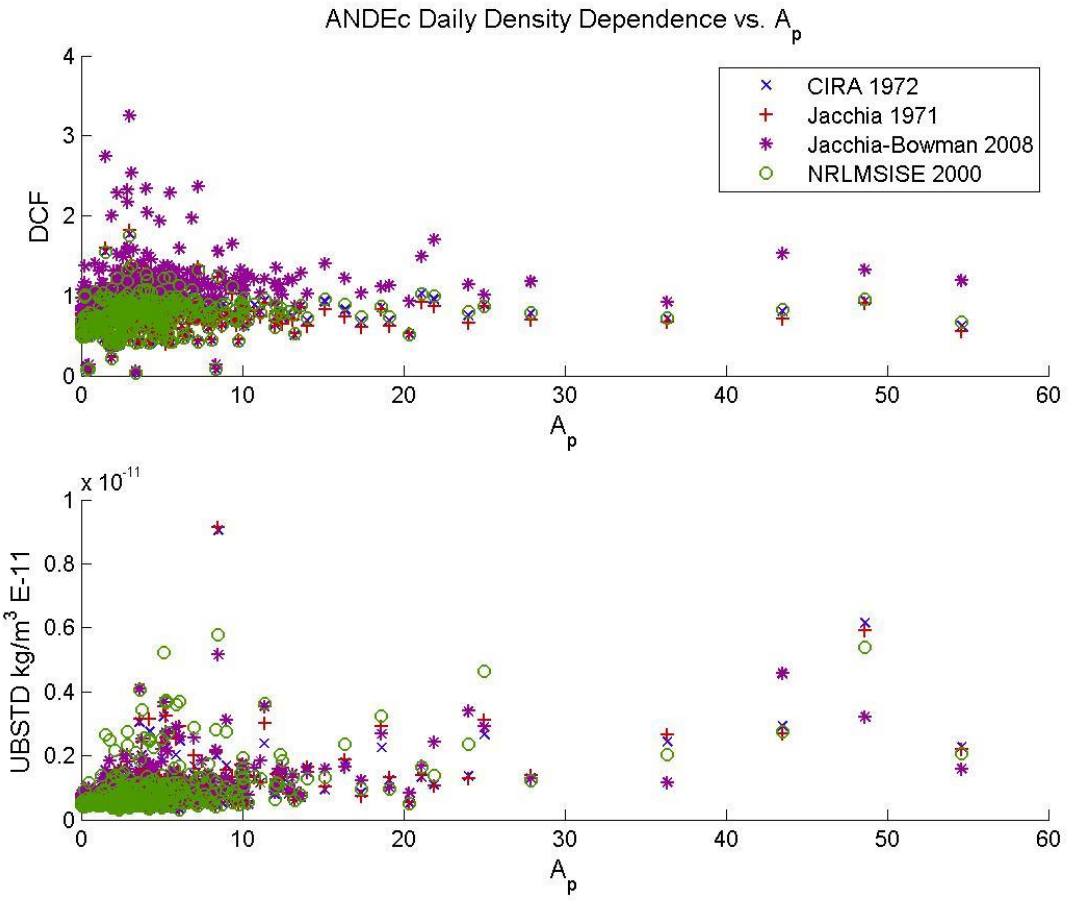

Figure 41: Variations in the *DCF* and *UBSTD* for ANDEc relative to daily geomagnetic activity

The daily geomagnetic activity levels seem to have little effect on the *DCF* and *UBSTD*. A slight upward trend is noticeable in the *UBSTD* as the geomagnetic activity level increases; this is in line with the findings of Lechtenberg (2015).

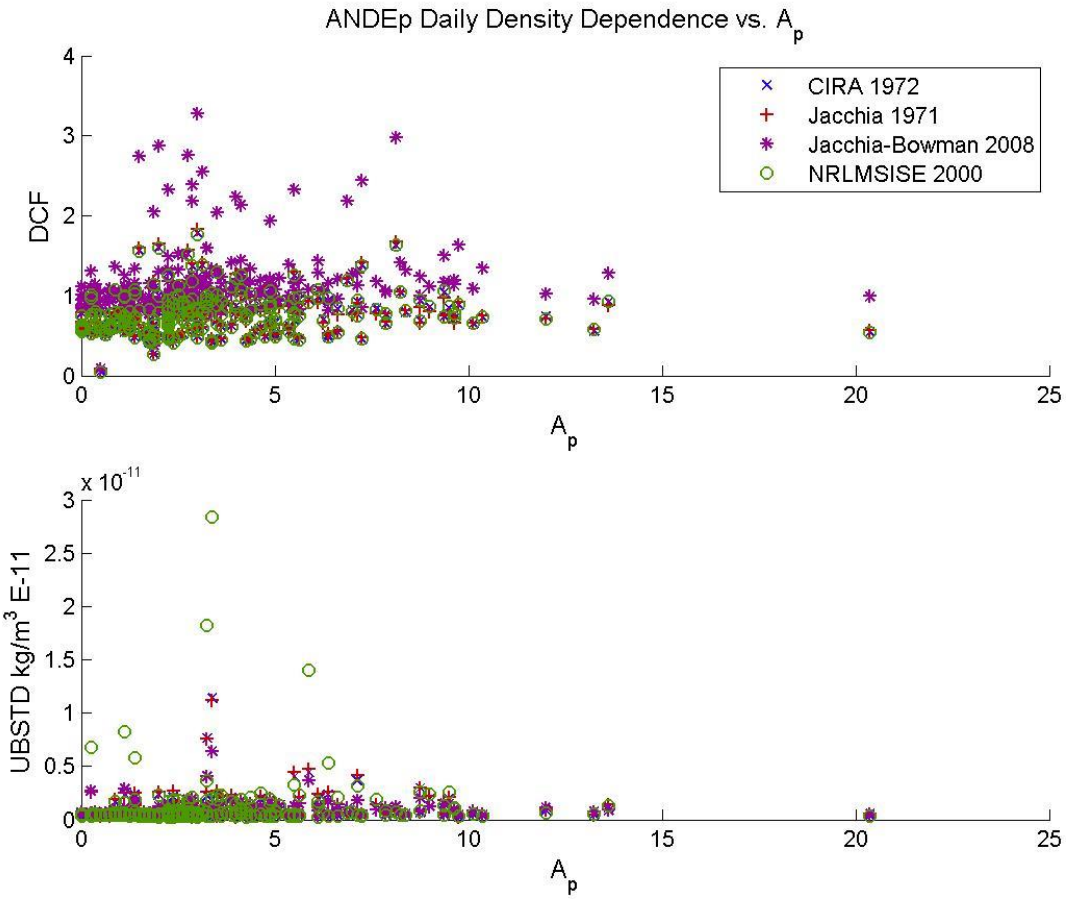

Figure 42: Variations in the *DCF* and *UBSTD* for ANDEp relative to daily geomagnetic activity

Little dependence for the DCF and UBSTD is evident in Figure 42. The higher UBSTD values correspond to the geomagnetic activity at the end of ANDEp's life.

3.6.2. **Weekly Density Dependence for ANDE-2**

The density data were binned into weekly bins and examined for variations in the *DCF* and *UBSTD* for the week, average weekly solar activity, and average weekly geomagnetic activity experienced by ANDEc and ANDEp over their life spans.

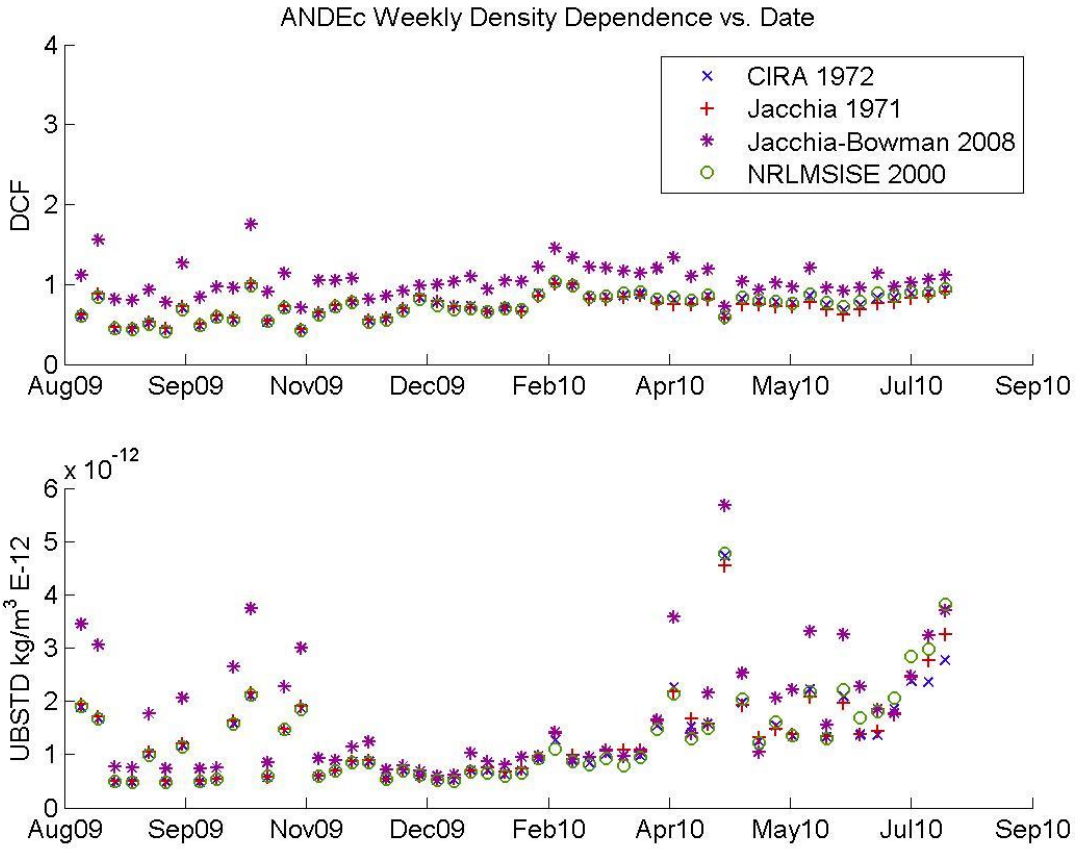

Figure 43: Weekly variations in the *DCF* and *UBSTD* for ANDEc

The weekly density dependence results are similar to the result obtained for the daily density dependence results. Towards the end of ANDEc's life, the *UBSTD* begins to increase around May of 2010.

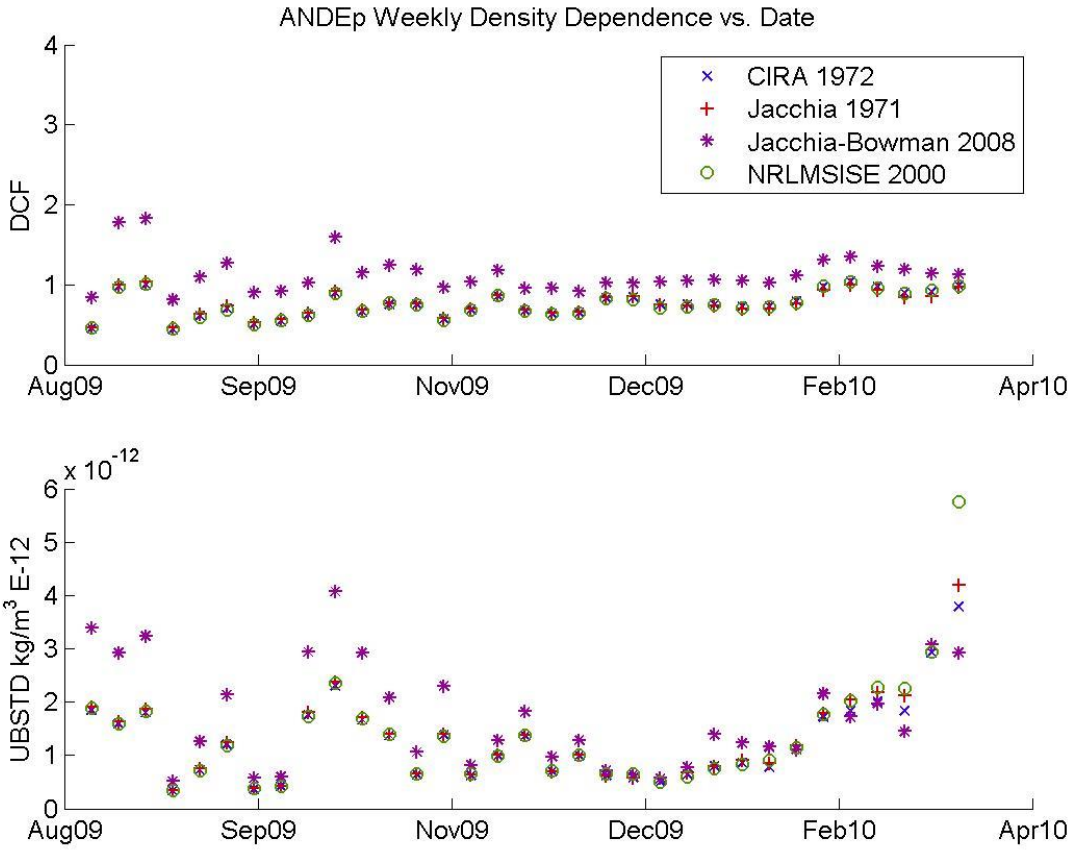

Figure 44: Weekly variations in the *DCF* and *UBSTD* for ANDEp

The DCF seems to show a slight upward trend towards the end of ANDEp's life, with the UBSTD showing a similar trend to the UBSTD in Figure 38.

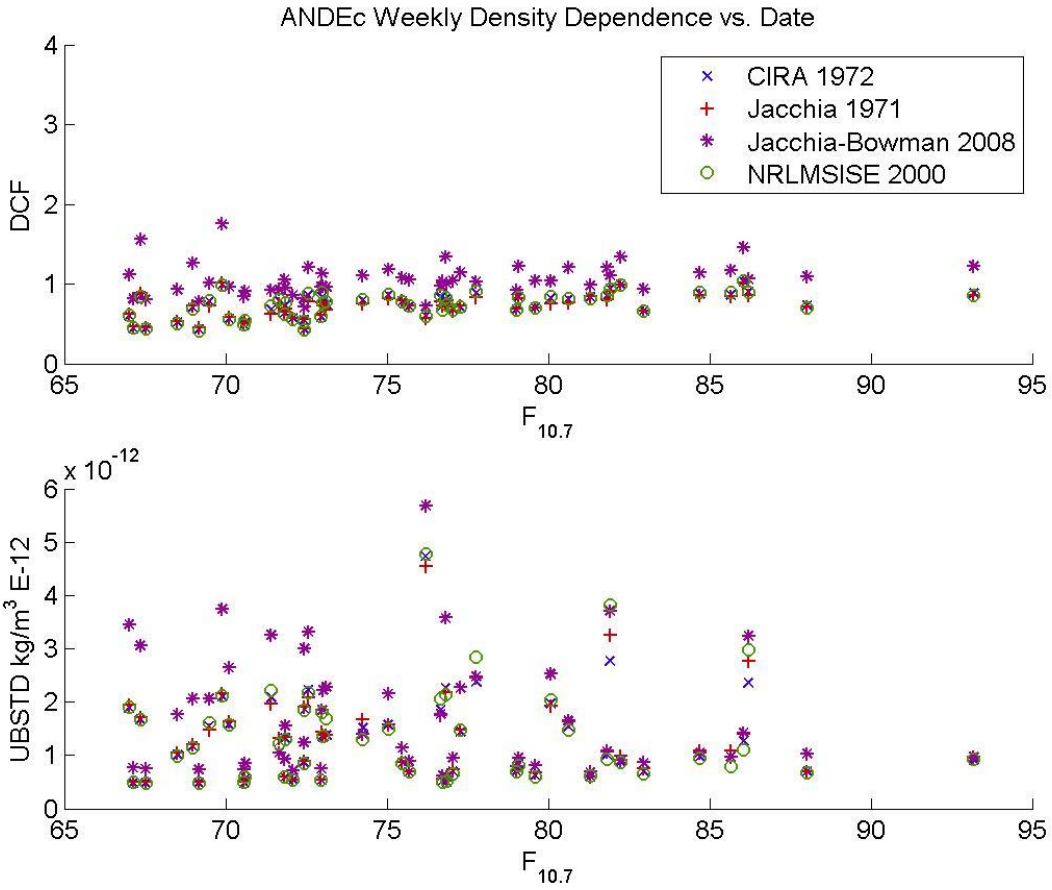

Figure 45: Variations in the *DCF* and *UBSTD* for ANDEc relative to weekly solar activity

The *DCF* and *UBSTD* show no apparent trend in relation to the solar activity levels as shown by Figure 45.

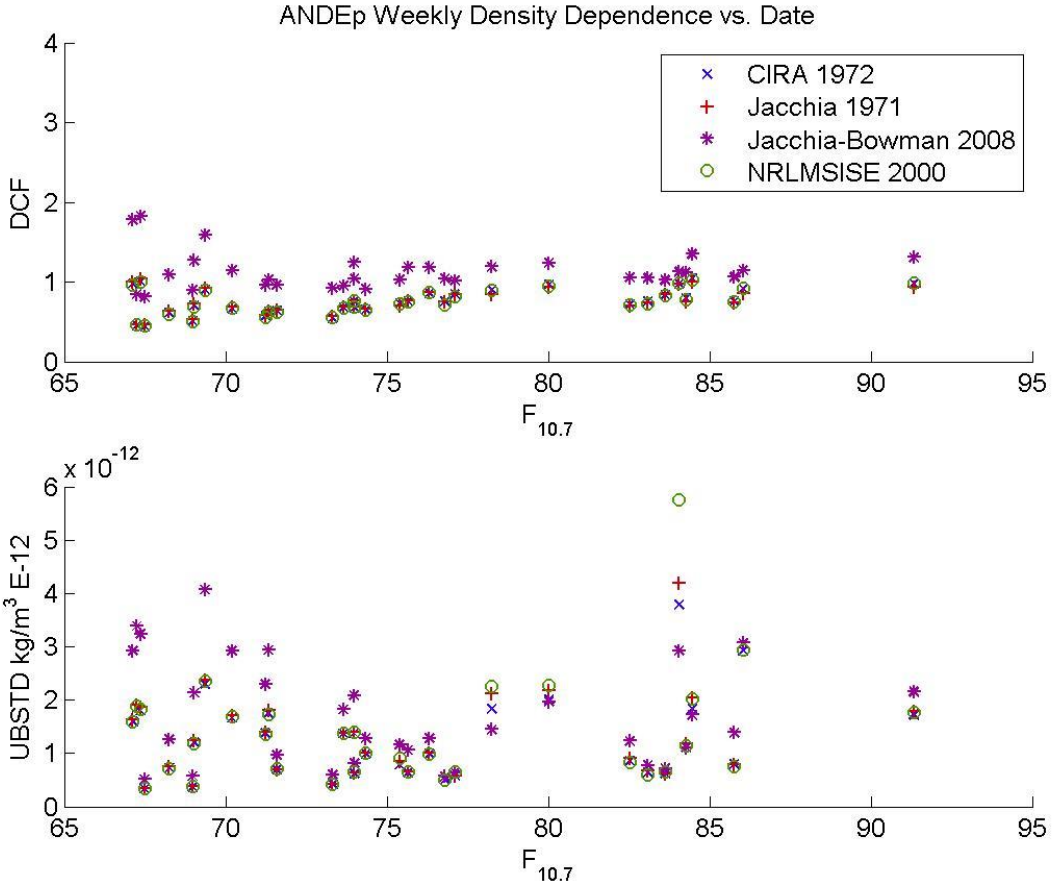

Figure 46: Variations in the *DCF* and *UBSTD* for ANDEp relative to weekly solar activity

No trend for the UBSTD and DCF is evident in Figure 46.

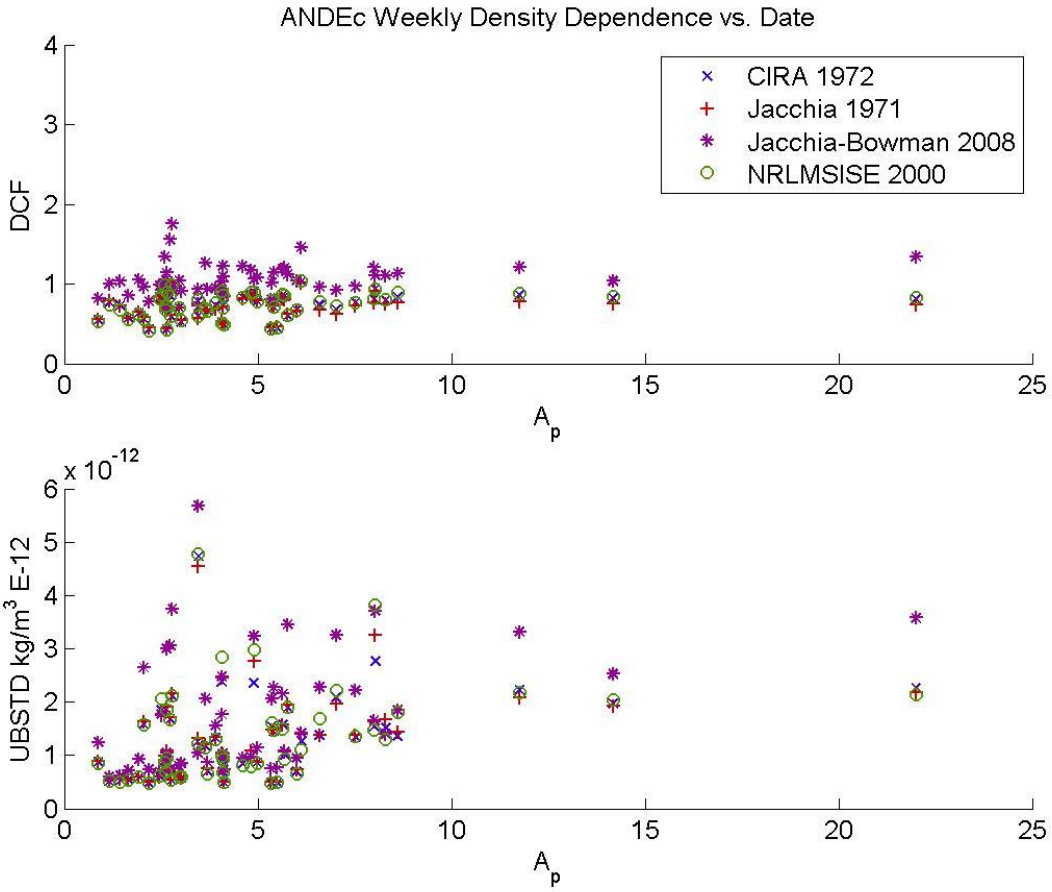

Figure 47: Variations in the *DCF* and *UBSTD* for ANDEc relative to weekly geomagnetic activity

Figure 47 shows that the weekly density dependence on the geomagnetic activity levels appears to show no trend. Most of ANDEc's operational life was during very low geomagnetic activity levels which makes it difficult to determine any noticeable trend of density error in relation to the geomagnetic activity levels.

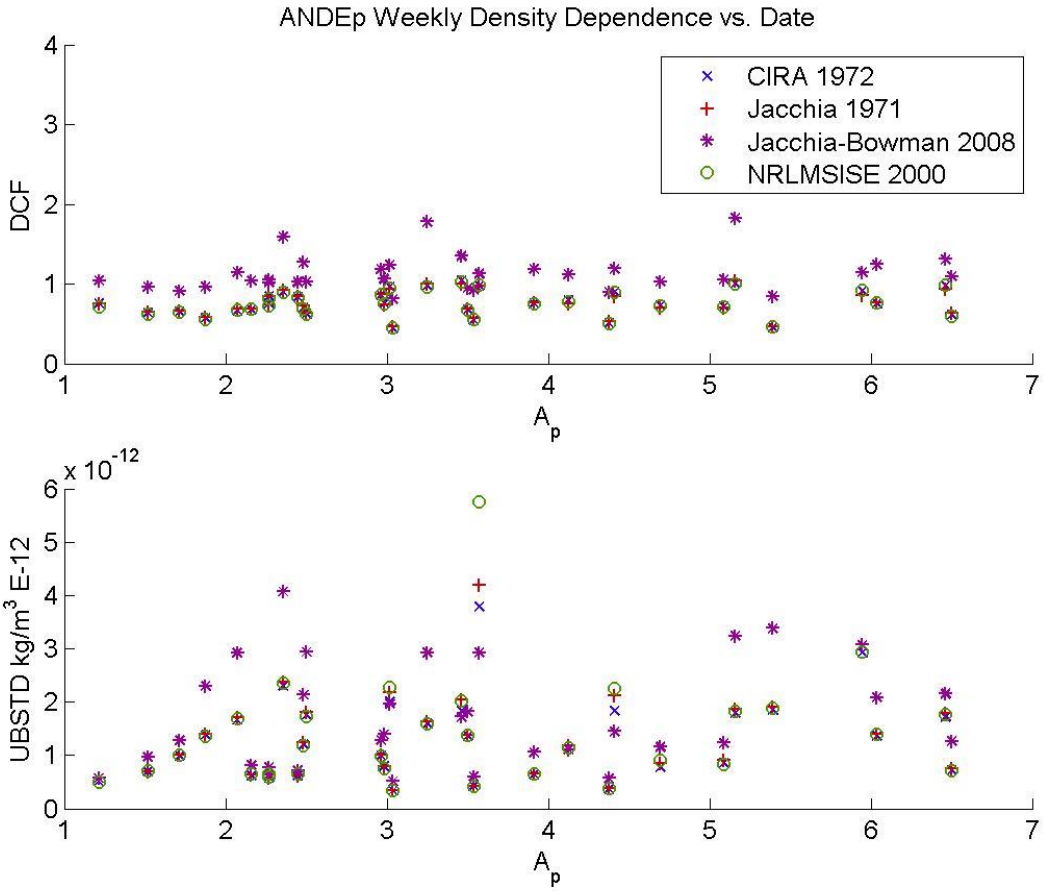

Figure 48: Variations in the *DCF* and *UBSTD* for ANDEp relative to weekly geomagnetic activity

No trend for the UBSTD and DCF is evident in Figure 48.

3.6.3. **Solar and Geomagnetic Effects on Density for ANDE-2**

The DCF and UBSTD were examined for solar and geomagnetic activity levels by determining the mean DCF and UBSTD for low and moderate solar and geomagnetic activity levels. Since there were no data for elevated or high solar and geomagnetic activity levels, only results for low and moderate levels will be shown. Lechtenberg's (2015) tables are included for comparison.

Table 21: DCF for low and moderate solar conditions for ANDE-2

DCF				
ANDEc				
Solar Activity	CIRA 1972	Jacchia 1971	NRLMSISE 2000	Jac-Bow 2008
Low	0.659	0.650	0.664	1.018
Moderate	0.819	0.800	0.820	1.106
ANDEp				
Solar Activity	CIRA 1972	Jacchia 1971	NRLMSISE 2000	Jac-Bow 2008
Low	0.668	0.683	0.663	1.127
Moderate	0.857	0.838	0.848	1.137

Table 22: DCF for low and moderate solar conditions for ANDEc (Lechtenberg, 2015)

Solar Activity Level	CIRA 1972	Jacchia 1970	NRLMSISE 2000	Jacchia-Bowman 2008
Low	0.726	0.731	0.724	0.903
Moderate	0.812	0.821	0.803	0.929

The DCF for low solar activity conditions remains constantly lower than the DCF for high solar conditions which is in line with the findings of Lecthenberg (2015). This means that the accuracy for most models is better during moderate solar activity conditions with the exception of the Jacchia-Bowman 2008 model, which appears more accurate for low solar activity conditions. Low solar condition DCFs were lower than Lechtenberg's (2015) results for all models except the Jacchia-Bowman 2008 model.

Table 23: *UBSTD* for low and moderate solar conditions for ANDE-2

UBSTD in kg/m^3 X 10^-12				
ANDEc				
Solar Activity	CIRA 1972	Jacchia 1971	NRLMSISE 2000	Jac-Bow 2008
Low	0.707	0.727	0.745	0.886
Moderate	1.044	1.113	1.165	1.141
ANDEp				
Solar Activity	CIRA 1972	Jacchia 1971	NRLMSISE 2000	Jac-Bow 2008
Low	0.410	0.420	0.429	0.591
Moderate	1.183	1.273	1.790	1.027

Table 24: *UBSTD* for low and moderate solar conditions in kg/m^3 for ANDEc (Lechtenberg, 2015)

Solar Activity Level	CIRA 1972	Jacchia 1970	NRLMSISE 2000	Jacchia-Bowman 2008
Low	1.112	1.084	1.073	1.032
Moderate	0.970	0.932	0.887	0.926

Table 23 shows that the precision for all models appears to be better during low solar activity conditions, with the CIRA 1972 and Jacchia 1971 models performing best. Low solar condition UBSTD results were better than the low solar condition UBSTD results found by Lechtenberg (2015), but were worse for moderate solar conditions.

Table 25: DCF for low and moderate geomagnetic conditions for ANDEc

DCF				
ANDEc				
Geomagnetic Activity	CIRA 1972	Jacchia 1971	NRLMSISE 2000	Jac-Bow 2008
Low	0.732	0.722	0.733	1.050
Moderate	0.782	0.729	0.803	1.171
ANDEp				
Geomagnetic Activity	CIRA 1972	Jacchia 1971	NRLMSISE 2000	Jac-Bow 2008
Low	0.761	0.759	0.754	1.132
Moderate	0.690	0.688	0.694	1.114

Table 26: DCF for low and moderate geomagnetic conditions for ANDEc (Lechtenberg, 2015)

Geomagnetic Activity Level	CIRA 1972	Jacchia 1970	NRLMSISE 2000	Jacchia-Bowman 2008
Quiet	0.750	0.755	0.745	0.914
Moderate	0.533	0.567	0.601	0.648

The *DCF* for low geomagnetic activity conditions also remained lower for low geomagnetic activity conditions, which is opposite the findings of Lechtenberg (2015). The DCF accuracy was better for moderate geomagnetic activity levels in comparison to Lechtenberg's (2015) results. Once again, the Jacchia-Bowman 2008 model seemed more accurate during low solar activity conditions.

Table 27: UBSTD for low and moderate geomagnetic conditions for ANDEc

UBSTD in kg/m^3 X 10^-12				
ANDEc				
Geomagnetic Activity	CIRA 1972	Jacchia 1971	NRLMSISE 2000	Jac-Bow 2008
Low	0.810	0.851	0.878	0.945
Moderate	1.486	1.557	1.672	1.668
ANDEp				
Geomagnetic Activity	CIRA 1972	Jacchia 1971	NRLMSISE 2000	Jac-Bow 2008
Low	0.788	0.837	1.099	0.803
Moderate	0.610	0.664	0.611	0.766

Table 28: UBSTD for low and moderate geomagnetic activity conditions in kg/m^3 for ANDEc (Lechtenberg, 2015)

Geomagnetic Activity Level	CIRA 1972	Jacchia 1970	NRLMSISE 2000	Jacchia-Bowman 2008
Quiet	1.082	1.052	1.033	1.009
Moderate	0.980	0.919	0.887	0.949

For ANDEc, Table 27 shows that Jacchia-Bowman 2008 model was less precise than the other models for low geomagnetic activity levels, but that the NRLMSISE 2000 model was least precise for moderate geomagnetic activity levels. Precision was also better for low geomagnetic activity conditions which are opposite the findings of Lechtenberg (2015).

More data were available for low geomagnetic activity level conditions. This means some potential biases may be present in the geomagnetic activity level results. For instance, the majority of geomagnetic storms occurred near the end of ANDEc's life, this is also when ANDEc's orbit began to decay rapidly resulting in an increase in the UBSTD. Therefore, the results for moderate geomagnetic activity levels may be biased due to the uncertainty obtained from ANDEc's decaying orbit.

The DCFs and UBSTDs for ANDEp during low geomagnetic activity conditions were higher than the DCFs and UBSTDs for moderate geomagnetic activity conditions. These results likely contain an altitude bias because of so few moderate geomagnetic activity level DCF and UBSTD data points.

3.6.4. **Altitude Density Dependence for ANDE-2**

Since biases may be present in the previously shown density dependency plots and tables for ANDEc, the density dependence based on altitude was also examined. Results are shown in Table 29 and Table 30.

Table 29: DCF for different altitudes for ANDEc

DCF				
ANDEc				
Altitude (km)	CIRA 1972	Jacchia 1971	NRLMSISE 2000	Jac-Bow 2008
350-300	0.702	0.704	0.698	1.076
300-250	0.787	0.735	0.807	1.007
250-200	0.978	0.953	0.978	1.165
ANDEp				
Altitude (km)	CIRA 1972	Jacchia 1971	NRLMSISE 2000	Jac-Bow 2008
350-300	0.706	0.716	0.698	1.114
300-250	0.897	0.855	0.891	1.196
250-200	0.964	0.955	0.963	1.106

Table 29 shows that for all models except the Jacchia-Bowman 2008 model that the DCF went up consistently with lower altitude. The Jacchia-Bowman 2008 model's DCF remained roughly constant.

Table 30: UBSTD for different altitudes for ANDEc

UBSTD in kg/m^3 X 10^-12				
ANDEc				
Altitude (km)	CIRA 1972	Jacchia 1971	NRLMSISE 2000	Jac-Bow 2008
350-300	0.625	0.651	0.614	0.778
300-250	1.145	1.118	1.348	1.294
250-200	3.131	3.511	3.857	2.973
ANDEp				
Altitude (km)	CIRA 1972	Jacchia 1971	NRLMSISE 2000	Jac-Bow 2008
350-300	0.432	0.443	0.450	0.594
300-250	1.247	1.394	1.152	1.100
250-200	4.120	4.316	9.037	2.659

Table 30 shows that the precision of all models went down over the lifespan of ANDEc. This is relatable to the findings shown in Figure 37 and shows that the UBSTD results were less precise at lower altitudes. The DCFs for ANDEp became more accurate towards the end of ANDEp's life and the UBSTDs becoming increasingly less precise towards the end of ANDEp's life. The DCF and UBSTD results for the entire lifespan (altitude span) of ANDEc and ANDEp are shown in Table 31 and Table 32.

Table 31: DCF for ANDEc's lifespan

DCF				
ANDEc				
Altitude (km)	CIRA 1972	Jacchia 1971	NRLMSISE 2000	Jac-Bow 2008
350-200	0.737	0.722	0.739	1.061
ANDEp				
Altitude (km)	CIRA 1972	Jacchia 1971	NRLMSISE 2000	Jac-Bow 2008
350-200	0.759	0.758	0.753	1.132

Table 31 shows that all models accept the Jacchia-Bowman 2008 atmospheric model overestimated the atmospheric density for most of ANDE-2's lifespan. The Jacchia-Bowman 2008 model was the most accurate model throughout ANDE-2's lifespan and the Jacchia 1971 model was the least accurate model throughout ANDEc's lifespan. The NRLMSISE 2000 model was the least accurate throughout ANDEp's lifespan.

Table 32: UBSTD for ANDEc's lifespan

UBSTD in kg/m^3 X 10^-12				
ANDEc				
Altitude (km)	CIRA 1972	Jacchia 1971	NRLMSISE 2000	Jac-Bow 2008
350-200	0.871	0.914	0.949	1.010
ANDEp				
Altitude (km)	CIRA 1972	Jacchia 1971	NRLMSISE 2000	Jac-Bow 2008
350-200	0.783	0.832	1.086	0.802

Table 32 shows that the CIRA 1972 model was the most precise model for estimating atmospheric density over ANDE-2's lifespan and the Jacchia-Bowman 2008 model was the least precise model for estimating atmospheric density over ANDEc's lifespan.

3.7. Effect of varying the Ballistic Coefficient Half-Life

The ballistic coefficient half-life (BCHL) was increased in order to see what effect it would have on the ballistic coefficient estimate and POE derived atmospheric density. Figure 49 shows the drag coefficients for October 6, 2009 using five different methods for estimating the ballistic coefficient: a constant BC with no ballistic coefficient half-life, a ballistic coefficient half-life of 1.8 minutes, a ballistic coefficient half-life of 90 minutes (1 orbit approximately), a ballistic coefficient half-life of 1 day, and a ballistic coefficient half-life of 1 week. The C_D used was 2.39. The atmospheric model used was the NRLMSISE 2000 model.

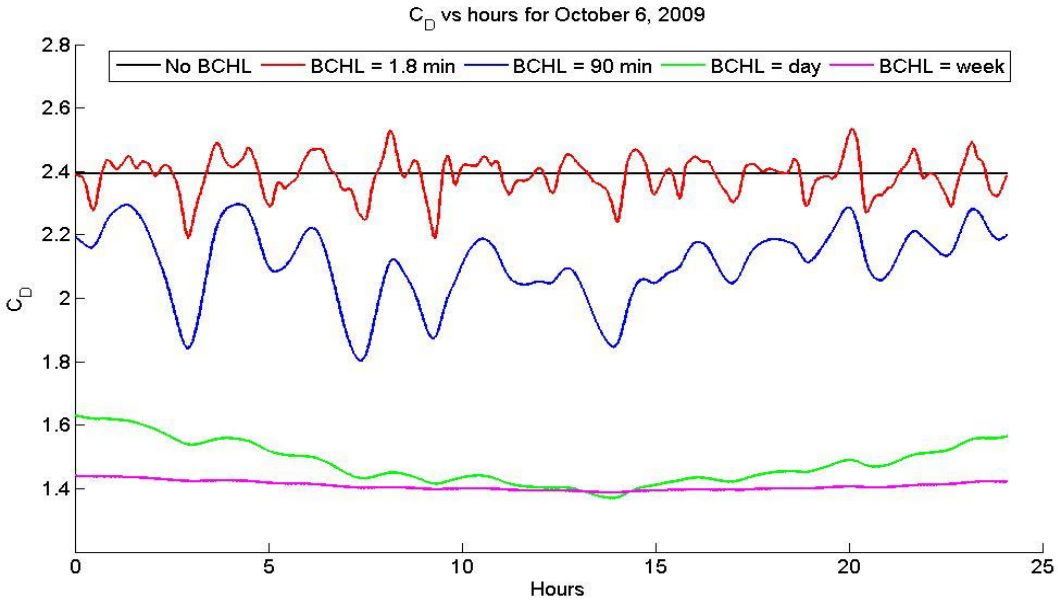

Figure 49: Different C_D estimates using different ballistic coefficient half-lives for ANDEc

The atmospheric densities for each ballistic coefficient half-life are shown in Figure 50.

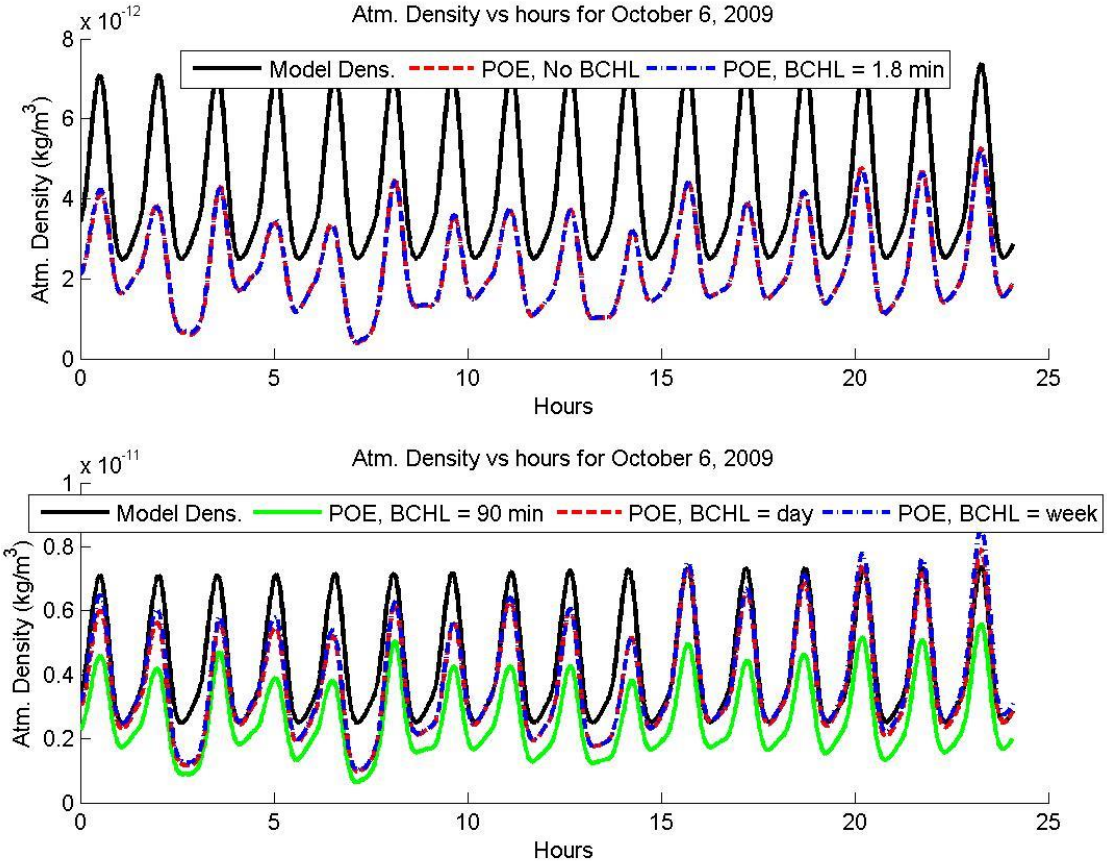

Figure 50: Different atmospheric density estimates using different ballistic coefficient half-lives for ANDEc

As the ballistic coefficient half-life is increased, the drag coefficient begins to form a downward trend eventually converging to approximately 1.4, this results in a closer fit to the atmospheric model's density which would suggest that a higher ballistic coefficient half-life results in an increase in error absorption from the atmospheric model. The POE derived density using the ballistic coefficient half-life of 1.8 minutes showed little difference in comparison to POE derived density with no ballistic coefficient half-life. This seems to show that shorter ballistic coefficient half-lives produce more realistic results than longer ballistic coefficients half-lives do. It also shows that estimating ballistic coefficient may be unnecessary.

4. Conclusions and Future Work

The obvious limitation to determining the drag coefficients of any spherical satellite using gas-surface interaction equations is the determination of a correct accommodation coefficient. Much of this limitation arises from the fact that the empirically determined drag coefficient data used in these semi-empirical accommodation coefficients models cannot be correctly matched with the theoretical model used (such as the Langmuir isotherm). Furthermore, the empirical satellite drag data must be related back to the atmospheric composition for which it was calculated. In the case of Pilinski et al. (2010) the empirically obtained drag coefficient data were related back to the encountered atmospheric composition by using the NRLMSISE 2000 model. This of course means that some error will be present in those calculations, as well as biased toward the NRLMSISE 2000 model. The accommodation coefficient model developed by Walker et al. (2014) related the empirically obtained drag coefficient data points back to their corresponding altitudes, and then fit the Langmuir isotherm to those points in the method described in section 1.8.5. This may have caused a bias at low solar activity levels and produced lower C_D values for ANDEc than it would have actually encountered. An interesting future project would be to recreate the Walker et al. (2014) method using empirical spherical satellite drag coefficient data for both high and low solar activity levels.

The POE derived densities were generally overestimated by the atmospheric models except for the Jacchia-Bowman 2008 model which generally underestimated the POE derived densities as shown in Table 29. Model densities were especially overestimated during the earlier part of ANDEc's life at higher altitudes using the CIRA 1972, Jacchia 1971, and NRLMSISE models. The maximum and minimum drag coefficients were used to calculate the atmospheric density to show variations in the POE derived density for changes in C_D, as well as to bound the POE derived densities calculated using the GSI obtained drag coefficients. The root mean square (RMS) difference error in the POE derived densities calculated using the maximum and minimum drag coefficient is approximately 8 to 15 percent for the days examined. This shows the importance of determining the correct drag coefficient for the each specific day being analyzed.

The ballistic coefficient half-life of 1.8 minutes produced little variation in the POE derived densities in comparison to the POE derived density using a constant ballistic coefficient. When the ballistic coefficient half-life was increased, the fitted drag coefficient decreased in its value and eventually converged to the value of 1.4 as shown in Figure 49. The drag coefficient value of 1.4 is not a realistic drag coefficient value in relation to any research regarding the drag coefficients of spherical satellites mentioned in this document. This is likely due to the absorption of errors from the atmospheric model used, and is evident in how the POE derived densities for the long ballistic coefficient half-lives match the atmospheric model densities. Therefore, shorter ballistic coefficient half-lives likely produce more accurate POE derived density data. And as shown in Figure 50, may not provide relevant change to the POE derived densities in relation to non-ballistic coefficient half-life derived POE derived densities.

Due to the fact that ANDE-2 was only operational during low solar and geomagnetic activity levels any meaningful information on errors encountered using the previously mentioned atmospheric models is difficult to determine. This means that any corrections to these atmospheric models for higher levels of solar and geomagnetic activity should be further investigated using the additional analysis of other satellites. Three other satellites that should be investigated would be the Atmospheric Neutral Density Experiment Risk Reduction (ANDERR) satellites and the Special Purpose Inexpensive Satellite (SPINSAT).

References

Adamson, A. W., *Physical Chemistry of Surfaces*, 5th ed., Wiley, New York, 1990

Analytical Graphics, Inc., "Orbit Determination Tool Kit Help," *Orbit Determination Tool Kit*, Version 6.4.1.

Anderson, B. D. O., and Moore, J. B., *Optimal Filtering*, Prentice-Hall, New Jersey, 1979.

Beletskty, V. V., "An Estimate of the Character of the Interaction Between the Airstream and a Satellite," *kosmicheskie Issledovaniya*, Vol. 8, No. 2, 1970, pp. 206-217 (in Russian).

Bierman, G. J., *Factorization Methods for Discrete Sequential Estimation*, Academic Press, New York, 1977.

Bird, G. A., "Approach to Translational Equilibrium in the Rigid Sphere Gas." *Physics of Fluid*, Vol. 6, 1963, pp. 1518.

Bird, G. A., *Molecular Gas Dynamics and the Direct Simulation of Gas Flows*, Oxford Science publication, New York, 1994.

Bird, G. A., "Visual DSMC Program for Three-Dimensional Flows: The DS3V Program User's Guide," G.A.B Consulting Pty Ltd, Version 2.5, October 2006.

Bourke, P., "Cross Correlation," August 1996, Web. July 23, 2015. http://paulbourke.net/miscellaneous/correlate/

Bowman, B. R., and Moe, K., "Drag Coefficient Variability at 175-500 km from the Orbit Decay Analyses of Spheres." *Advances in the Astronautical Sciences*, AAS 05-257, Vol. 123, 2006, pp. 117-136.

Bowman B. R., Tobiska W. K., Marcos F. A., Huang C. Y., Lin C. S., and Burke W. J., "A New Empirical Thermospheric Density Model JB2008 Using New Solar and Geomagnetic Indices," AIAA 2008-6438, AIAA/AAS Astrodynamics Specialist Conference, Honolulu, HI, August 2008.

Brown, C. D., *Elements of Spacecraft Design*, AIAA Education Series, American Institute of Aeronautics and Astronautics, Inc., Reston VA, 2002, Ch. 7, pages 373-406.

Cercignani, C., and Lampis, M., "Kinetic Models for Gas-Surface Interactions," *Transport Theory and Statistical Physics* Vol. 1, Issue 2, 1971, pp. 101-114. doi: 10.1080/00411457108231440.

Ching, B. K., Hickman, D. R., and Straus, J. M., "Effects of Atmospheric Winds and Aerodynamic Lift on the Inclination of the Orbit of the S3-1 Satellite," *Journal of Geophysical Research*, Vol. 82, No. 10, 1977, pp. 1474-1480.

COSPAR Working Group IV, *COSPAR International Reference Atmosphere*, Akedemie-Verlag, Berlin, 1972.

Earth Observation Portal, "ANDE-2" Web June 2, 2015. https://directory.eoportal.org/web/eoportal/satellite-missions/a/ande-2.

Gelb, A. (ed.), *Applied Optimal Estimation*, Massachusetts Institute of Technology Press, Cambridge, Ma, 1974.

Goodman, F. O., and Wachmann, H. Y., "Formula for Thermal Accommodation Coefficient," Massachusetts Inst. Of Technology, Fluid Dynamcis Lab. Rept. 66-1, Cambridge, MA, 1966.

Graziano, B. P., "Computational Modelling of Aerodynamics Disturbances on Spacecraft within a Concurrent Engineering Framework," PhD Thesis, Cranfield University, 2007.

Gregory, J. C., and Peters, P. N., "A Measurement of the Angular Distribution of the 5eV Atomic Oxygen Scattered off a Solid Surface in Earth Orbit. *Proceedings of the 15th International Symposium on Rarefied Gas Dynamics, vol. 2,* B. G. Teubner, Stuttgart, Germany, 1987, pp. 644-659.

Grewal, M. S., and A. P. Andrews, *Kalman Filtering: Theory and Practice*, Pretice Hall, 1993.

Goodman, F., "Thermal Accommodation Coefficients," *Journal of Physics and Chemistry*, Vol. 84, 1980, pp. 1431-1445.

Harrison, I. K., and Swinerd, G. G., "Analysis of Satellite Laser Range Data to Investigate Satellite Aerodynamics," *Planetary and Space Science,* Vol. 42, No.8, 1995, PP. 1023-1033.

Hedin, A. E., Hinton, B. B., and Schmitt, G. A., "Role of Gas-Surface Interaction in the Reduction of OGO 6 Neutral Particle Mass Spectrometer Data," *Journal of Geophysical Research*, Vol. 78, 1973, pp. 4651-4668.

Heimholtz Centre Potsdam GFZ German Research Centre for Geosciences (GFZ), "Kp index archive." Web May 7, 2015. http://www.gfz-potsdam.de/sektion/erdmagnetfeld/daten-dienste/kp-index/archiv/.

Hinchen, J. J., and Foley, W. M., "Scattering of Molecular Beams by Metallic Surfaces," *Rarefied Gas Dynamics,* Ed. De Leeuw, J. H., Academic Press Inc., New York, 1966.

Imbro, D. R., Moe, M. M., and Moe, K., "On Fundamental Problems in the Deduction of Atmospheric Densities from Satellite Drag," *Journal of Geophysical Research,* Vol. 80, No. 22, 1975, pp. 3077-3086.

Jacchia L. G., *Revised Static Models for the Thermosphere and Exosphere with Empirical Temperature Profiles*, SAO Special Report No. 332, Smithsonian Institution Astrophysical Observatory, Cambridge, MA, 1971.

Kalman, R. E., "New Methods in Wiener Filtering Theory," *Proceedings of the First Symposium on Engineering Applications of Random Function Theory and Probability*, edited by J. L. Bogdanoff and F. Kozin, John Wiley & Sons, New York, 1963.

Knechtel, E. D., and Pitts, W. C., "Experimental Momentum Accommodation on Metal Surfaces of Ions near and above Earth-Satellite Speeds," *Rarefied Gas Dynamics,* Supplement 5, No. 2, 1969, pp. 1257-1266.

Knudsen, M., *The Kinetic Theory of Gases*, Methuen Publ., London, 1934.

Lechtenberg, T. F., Density Model Corrections Derived from Orbit Data to Characterized Upper Atmospheric Density Variations, PhD Dissertation, University of Kansas, 2015.

Lechtenberg T., "Derivation and Observability of Upper Atmospheric Density Variations Utilizing Precision Orbit Ephemerides," M. S. Thesis, Department of Aerospace Engineering, University of Kansas, 2010.

Liebelt, P. B., *An Introduction to Optimal Estimation*, Addison-Wesley, Reading, MA, 1967.

Lord, R. G., "Some Extensions to the Cercignani-Lampis Gas-Surface Scattering Kernal," *Physics of Fluids*, Vol.3, No. 4, 1991a, pp. 706-710.

Lord, R. G., "Application of the Cercignani-Lampis Scattering Kernal to Direct Simulation Monte Carlo Calculations", *17th International Symposium on Rarefied Gas Dynamics*, Ed. Beylich, A. E., VCH Aachen, 1991b, pp. 1427-1433.

MATLAB, version R2014a, Help File, Aerospace Toolbox, Mathworks, Inc., Natick, Massachusetts, 2014.

Maybeck, P. S., *Stochastic Models, Estimation and Control*, Vol. 1, Academic Press, 1979.

Meditch, J. S., *Stochastic Optimal Linear Estimation and Control*, McGraw-Hill, New York, 1969.

Mehta, P. M., Thermospheric Density and Satellite Drag Modeling, PhD Dissertation, University of Kansas, 2013.

Mehta, P. M., Walker, A., and McLaughlin, C., "Comparing Physical Drag Coefficients Computed Using Different Gas-Surface Interaction Models," *Journal of Spacecraft and Rockets*, Vol. 47, No. 6, May-June 2014.

Moe, K., and Moe, M., "The Effect of Absortion on Densities Measured by Orbiting Pressure Gauges," *Planetary and Space Science*, Vol. 15, 1967, pp. 1329-1332.

Moe, M. M., and Moe, K., "The Role of Kinetic Theory and Das-Surface Interactions in Measurements of Upper-Atmospheric Density," *Planetary and Space Science*, Vol 17, No. 5, 1969, pp. 917-922.

Moe, K., Moe M. M., and Yelaca, N. W., "Effect of Surface Heterogeneity on the absorptive behavior of orbiting pressure gages," *Journal of Geophysical Research*, Vol. 77, 1972, pp. 4242-4247.

Moe, M. M., Wallace, S. D., and Moe, K. "Recommended Drag Coefficients for Aeronomic Satellites," *The Upper Mesosphere and Lower Thermosphere: A Review of Experiment and Theory*, edited by R. M. Johnson, and T. L. Killeen, Geophysical Monograph, Vol. 87, American Geophysical Union, Washington, D.C., 1995, pp. 349-445.

Moe, K., and Moe, M. M.; "Gas-Surface Interactions and Satellite Drag Coefficients." *Planetary and Space Science*, Vol. 53, 2005, pp. 793-801.

Montenbruck, O., and Gill, E., *Satellite Orbits: Models, Methods, Applications*, Springer-Verlag, Berlin, 2001.

National Geophysical Data Center, *Solar Indices Bulletin*, Boulder, CO: National Geophysical Data Center, Web. 7 May, 2015a http://www.ngdc.noaa.gov/ and Solar Flux Data, ftp://ftp.ngdc.noaa.gov/STP/SOLAR_DATA/SOLAR_RADIO/FLUX.

National Geophysical Data Center, *Solar Indices Bulletin*, Boulder, CO: National Geophysical Data Center, Web. 7 May, 2015b http://www.ngdc.noaa.gov/ and Geomagnetic Data, ftp://ftp.ngdc.noaa.gov/STP/GEOMAGNETIC_DATA/INDICES/KP_AP.

Natural Resources Canada, "Solar Radio Flux – Archive of Measurements." *Space Weather Canada*. Ottawa, Canada. Web. 7 May, 2015. http://www.spaceweather.ca/solarflux/sx-5-eng.php.

Offermann, D., and Grossmann, K. U., "Thermospheric Density and Composition as Determined by a Mass Spectrometer with Cyro Ion Source," *Journal of Geophysical Research*, Vol. 78, 1973, pp. 8296-8304.

Pardini, C., Anselmo, L., Moe, K., and Moe, M., "Drag and Energy Accomodation Coefficients During Sunspot Maximum," *Advances in Space Research*, Vol. 45, No. 4, 2010, pp. 638-650. doi: 10.1016/j.asr.2009.08.034.

Pearlman, M.R., Degnan, J.J., and Bosworth, J.M., "The International Laser Ranging Service," *Advances in Space Research*, Vol. 30, No. 2, pp. 135-143, July 2002, DOI:10.1016/S0273-1177(02)00277-6.

Picone J.M., Hedin A. E., and Drob D. P., "NRLMSISE-00 Empirical Model of the Atmosphere: Statistical Comparisons and Scientific Issues," *Journal of Geophysical Research*, Vol. 107, No. A12, 2002.

Pilinksi, M. D., Argrow, B. M., and Palo, S. E., "Semi-Empirical Model for Satellite Energy Accommodation Coefficients," *Journal of Spacecraft and Rockets*, Vol. 47, No. 6, November-December 2010.

Pilinski, M. D., Argrow, B. M., and Palo, S. E. "Drag Coefficients of Satellites with Concave Geometries: Comparing Models and Observations," *Journal of Spacecraft and Rockets*, Vol. 48, No. 2, March-April 2011.

Saltsburg, H., Smith, Jr., J. N., and Rogers, M. (Eds.), *Fundamentals of Gas-Surface Interactions*, Academic Press, New York, 1967.

Sentman, L. H., "Free Molecular Flow Theory and its Application to the Determination of Aerodynamic Forces," *Technical Report LMSC-448514*, Lockheed Aircraft Corporation, Sunnyvale, California, 1961a.

Sentman, L. H., "Comparison of the Exact and Approximate Methods for Predicting Free-Molecular Aerodynamic Coefficients," *American Rocket Society Journal*, Vol. 31, 1961b, p. 1576-1579.

Sherman, S., *A Theorem on Convex Sets with Applications*, The Annals of Mathematical Statistics Vol. 26, pages 763-767, 1955.

Sherman, S., *Non-Mean-Square Error Criteria*, IRE Transactions on Information Theory, Vol. IT-4, 1958.

Sorenson, H. W. (ed.), *Kalman Filtering: Theory and Applications*, IEEE Press, 1985.

Swerling, P., "First order error propagation in a stagewise differential smoothing procedure for satellite observation," *J. Astronaut. Sci.*, Vol. 6, pp. 46-52, 1959.

Tapley, B. D., "Statistical orbit determination theory", in *Recent Advances in Dynamical Astronomy*, B. D. Tapley and V. Szebehely (eds.), D. Reidel, pp. 396-425, 1973.

Tapley, B. D., Schutz, B. E., and Born, G. H. *Statistical Orbit Determination*, Elsevier Academic Press, Amsterdam, 2004.

Walker, A., Mehta, P., and Koller, J., "Drag Coefficient Model using the Cercignani-Lampis-Lord Das-Surface interaction Model," *Journal of Spacecraft and Rockets,* Vol. 51, No. 5, Sep.-Oct 2014.

Watt, W., and Moreton, R., "The Thermal Accommodation of Helium and Argon on Tungsten and Platinum at Elevated Temperatures," Defense Documentation Center for Scientific and Technical Information, Cameron Station, Alexander, Virginia, 1964

Wright, J, R., "Orbit Determination Tool Kit *Theory & Algorithms*," Analytical Graphics, Inc., Nov. 1, 2013. https://www.agi.com/downloads/resources/white-papers/ODTK-Theory-and-Algorithms.pdf

Vallado D. A., *Fundamentals of Astrodynamics and Applications,* Microcosm Press, El Segundo, CA, 3rd Edition, 2007, Chapters 3, 8.

Vallado, D. A., Hujsak, R. S., Johnson, T. M., Seago, J. H., and Woodburn, J. W., "Orbit Determination Using ODTK Version 6," *European Space Astronomy Center (ESA/ESAC),* Madrid, Spain, May 2010.